A study on the mechanical properties of micro-truss *Ti-6Al-4V* materials fabricated by Electron Beam Melting

Everth Hernández-Nava

A thesis presented for the degree of
Doctor of Philosophy

Materials Science and Engineering
The University of Sheffield
United Kingdom
2016

Contents

1 Introduction 5

2 The physical metallurgy and Electron Beam Melting of *Ti-6Al-4V* 11
- 2.1 Physical metallurgy of titanium 11
  - 2.1.1 Crystal structure 11
  - 2.1.2 Deformation mechanisms 12
  - 2.1.3 Alloy classification 12
  - 2.1.4 Phase transformation 13
  - 2.1.5 Strengthening mechanisms 15
  - 2.1.6 The *Ti-6Al-4V* system 15
- 2.2 Electron Beam Melting 19
  - 2.2.1 Raw materials 21
  - 2.2.2 3D CAD design 22
  - 2.2.3 Processing steps 23
  - 2.2.4 Design for EBM 23
  - 2.2.5 Solidification in Additive Manufacturing 28
  - 2.2.6 *Ti-6Al-4V* microstructures in AM 28
  - 2.2.7 Mechanical properties of *Ti-6Al-4V* in EBM 29
- 2.3 AM Processing of thin sectioned materials 31
- 2.4 Summary 32

3 Deformation in cellular solids 35
- 3.1 Introduction 35
- 3.2 Deformation mechanisms 35
  - 3.2.1 Bending-dominated elastic properties 36
  - 3.2.2 Bending-dominating plastic resistance 36
  - 3.2.3 Stretching-dominated structures 37
- 3.3 Energy absorption and blast protection 38
  - 3.3.1 Strain rate sensitivity 39
  - 3.3.2 Blast wave protection 39
- 3.4 Mechanical properties of EBM cellular solids 40
  - 3.4.1 Bulk Properties 41
  - 3.4.2 Meso-sructure 41
  - 3.4.3 Structural performance 42
- 3.5 Summary 44

4 Experimental procedure 45
- 4.1 EBM manufacturing 45
  - 4.1.1 Build design and parameters set-up 45
  - 4.1.2 ARCAM S12 system 46

4.1.3 Raw materials control 46
4.2 X-ray Computer Tomography (XCT) 47
4.2.1 Data acquisition 47
4.2.2 Visualization 47
4.3 Quasi static tests 48
4.3.1 Tensile testing 48
4.3.2 Compression testing 49
4.3.3 Three point bending 49
4.4 Dynamic tests 49
4.5 Heat treatments 50
4.6 Sample micropreparation 50
4.7 Optical Microscopy 50
4.7.1 alpha lath thickness measurements 51
4.7.2 Alpha colony size measurements 51
4.8 Scanning Electron Microscopy (SEM) 51
4.9 X-ray Diffraction (XRD) 52
4.10 Microhardness Vickers (VH) 52

5 EBM deposition and material characterization 53
5.1 Electron beam penetration 53
5.1.1 Rosenthal's approach 53
5.1.2 Experimental beam depth correlation 54
5.2 Microstructure development 58
5.2.1 As-built microstructure 58
5.3 Mechanical properties 60
5.3.1 Tensile response 61
5.4 Chapter conclusions 65

6 The effect of density and feature size on mechanical properties of metal foams 67
6.1 Files construction 67
6.2 EBM manufacturing 68
6.2.1 Metallic foams 68
6.2.2 Specimens for parent properties 69
6.3 Mechanical properties 69
6.3.1 Compressive response 69
6.3.2 Elastic properties 70
6.3.3 Compressive strength 71
6.4 Parent metal strength 72
6.4.1 Flexural strength 74
6.5 Chapter conclusion 76

7 The effect of defects and microstructure for lattices loaded under equilibrium conditions 79
7.1 Materials processing 79
7.1.1 Structure design 79
7.1.2 EBM fabrication 80
7.2 Investigation of thermal histories 81
7.2.1 Lattices in the "As-built" condition 82
7.2.2 Lattices in the 960°C/2h/FC condition 83

7.2.3 Lattices in the 1200°C/2h/FC condition 84
7.3 Compressive response 85
7.4 Strut cross sectional area 90
7.5 Internal defects and surface roughness 91
7.6 Deformation mode 94
7.6.1 Systematic investigation of shear band thickness 95
7.6.2 Localisation from testing 96
7.6.3 Shearing zones 96
7.6.4 Microstructural evolution 99
7.7 Chapter conclusions 100

8 Defect population and applications of EBM-processed TI lattices 101
8.1 True density and the problem with design 102
8.2 Compressive strength of diamond-like structures 104
8.2.1 Mechanical properties 104
8.2.2 Effect of specimen size 106
8.2.3 Effect of sample aspect ratio, $L/H \geq 1$ 106
8.3 Truss element orientation and the problem with manufacturing 108
8.4 Strength comparison towards volume optimisation 112
8.5 Applications for spatial spread of loading 113
8.6 Chapter summary 115

9 Conclusions 117

10 Future work 119
10.1 EBM characterisation 119
10.2 Heat balance 119
10.3 Deposition strategies 119
10.4 Grain growth in narrow sections 120
10.5 Defect location and loading direction 120

List of Figures

1.1 Schematic representation of the EBM process of their three consecutive stages. 7

2.1 Unit cell of "α" and "β" phases showing the most densely packed lattice planes. 11
2.2 Slip planes and directions in a primitive hexagonal lattice. 12
2.3 Pseudo-binary section through a β isomorphous phase diagram showing α, $\alpha + \beta$ and β regions. 13
2.4 Derivation of the closed-pack hexagonal cell from the bcc lattice. 14
2.5 Ti-6Al-4V transformed microstructures from 1040°C after: a)water quenched to room temperature and, b) furnace cooling [1]. 14
2.6 Structures found for $\alpha + \beta$ alloys as: a) Lamellar, b) Equiaxed and c) Bimodal type. 17
2.7 Left, the oxygen content and heat treatments on the Young's modulus values[2], solution treatment plus quenching (STQ) for various oxygen contents. Right, the oxygen influence on tensile properties in annealed *Ti-6Al-4V* [3]. 17
2.8 Stress axis and c axis relationship on the Young's modulus for α titanium single crystal. 18
2.9 Specimens after bending in the parallel direction to the rolling direction (top), and to the transverse orientation (bottom). 19
2.10 Left, schematic figure of the ARCAM system. Right, an image of the ARCAM system S12. 19
2.11 EBM stages of preheat, contouring and melting from left to right respectively. 20
2.12 Left, SEM figure of spherical *Ti-6Al-4V* power particles. Right, a test of powder particles flowability. 21
2.13 STL representation showing; a) design volume, b) triangulated tessellation, c) triangle unit composed of coordinates and normal 22
2.14 Intersecting triangles highlighted in yellow found in STL files; (a) in a single node, (b) multiplied in all connecting nodes. 23
2.15 Sketch on the speed v adjustment as a function of thickness t. 26
2.16 Schematic representation of the heat balance in order to reach the equilibrium temperature for materials development. 26
2.17 Five speed functions (SF) of different speed-current relationship. 27
2.18 Columnar β grain morphology and a solidification processing map for *Ti-6Al-4V* [4]. 28
2.19 A Continuous cooling diagram for *Ti-6Al-4V* after solution heat treatments at 1050°C [5]. The inserted images show the EBM (top) and SLM *Ti-6Al-4V* microstructure (bottom)[6]. 29
2.20 Mechanical properties reported for Ti-6Al-4V from various AM routes. EBM from table 2.4, SLM and DED from [7][8] [9][10]. 31

2.21 Lattices with variations in beam energy when processed by (a) and (b) SLM and by EBM (c). While energy variations in SLM reported significant porosity fractions and different mechanical properties [11], EBM energy changes did not showed a significant variation of bulk properties [12]. 32

3.1 Schematic representation of: (a) Open unit cell, (b) bending mechanisms acting as a deformation mode, (c) a closed unit cell with (d) tension deformation within their membrane elements. 36
3.2 Schematic representation of stress-strain curves [13] with key features under compression of: Bending-dominated structures and stretching-dominated structures shown in left and right respectively. 38
3.3 Left, stress-strain curve for a material with energy absorption applications including; a stress plateau σ_{pl} prior densification ϵ_d [14]. Right, a schematic representation of a material deformed uniaxially showing the shock wave propagation. 38
3.4 Left, stress-strain compression curves at quasistatic and dynamic strain rate $\dot{\epsilon}$. Right, kinematics of plastic deformation where F is the external load, l and t the length and thickness of the uni cell, $\dot{\theta}$ the rotation of the plastic hinge and δ the displacement [15]. 39
3.5 Examples of lattices fabricated as proof of the concept for EBM manufacturing. (a)Cellular solids with auxetic behaviour [16], (b) Diamond-like lattices for biomedical applications [17], (c) Tensegrity structures [18] and (d) foams with ideal tetrakaidecahedra packing [19]. 42
3.6 Compressive strength and stiffness of EBM an SLM Ti-6Al-4V lattices and foams[11][12][17][20][21][22][23][24]. 43

4.1 Schematic EBM sequence including: (a) The surface representation, (b) the slicing of files and (c) the file uploading. 45
4.2 (a) The X-ray tomography equipment showing the x-ray source, the sample to be scanned and the panel detector. Schematic illustration of the XCT analysis of an imaged strut in (b) and (c). 47
4.3 Zwick/Roell Z050 test rig machines tests of (a) compression and (b) three-point bending. 48
4.4 Horizontal and vertical tensile specimens, (a) and (b) respectively, after tensile tests showing fracture due to “necking” effects typically found in ductile metals. (c) Schematic drawing of the gripping system prior tensile testing. 48
4.5 Hopkinson bar set-up and image recording. (a) the Hopkinson bar, (b) the striker canon, (c) the high speed video camera. 50
4.6 Measurement of α lath thickness by intersecting closed lines. 51
4.7 Colony size determination through a random array of lines on OM images [25]. 51
4.8 Vickers microhardness measurements, (a) grid of indentations with 100μm separation. (b) Contour plots showing microhardness distribution. 52

5.1 Melt pool depths for all the weldtracks according the table 5.1 the blue dashed line highlights the change in microstructure from the affected zone. . 56
5.2 Experimental melt pool depth comparison with η values of 0.9, 0.85, 0.8 and 0.75. 57
5.3 Experimental melt pool depth versus the speed/current for two *speed functions*. 57

5.4 Horizontally and vertically oriented EBM specimens for metallographic observations and tensile tests. 58
5.5 (a) Typical columnar β grain microstructure shown for EBM components, the build direction from bottom to top. (b) and (c) showing fine Widmanstatten α and small α colony. (d)XRD pattern for the "as-built" condition 59
5.6 Microstructure of the horizontal tensile specimens were a similar α lath thickness can be seen. 60
5.7 Micrographs of the vertical tensile samples showing; the columnar β morphology and relatively fine α laths for all specimens. 60
5.8 Temperature versus time for the two set of specimens. The first drop in temperature represents the *out gassing*, a common cleaning practise for the build chamber before the process starts. 62
5.9 Yield strength versus the inverse square root of the alpha lath thickness [6] [26] [27][28][29][30][31][32]. 63
5.10 Maximum elongation prior failure found in titanium alloys and *Ti-6Al-4V* alloys manufactured by SLM and EBM data from this work and [22][27][31][33][34]. 64
5.11 Side views of fracture surfaces in horizontal (a and b) and vertical (c and d) specimens after the tensile tests. While the vertical samples show an interrupted columnar microstructure at the failure point, a more random distribution is seen in horizontal specimens. 64

6.1 Porous foam file creation from: (a) A region taken from a 2-D virtual slice through the 3-D CT image of the 3.9 mm spheres, (b) segmented 3-D representation of a small part of the 3-D image and (c) inverted image showing the spheres as cavities within a solid framework. 67
6.2 2-D cross-section of the inverted bead pack and (b) a node in the STL files used showing the difference in thickness produced by a surface offset of 100μm. 68
6.3 Foam samples produced by XCT and EBM, with the measured relative density listed explicitly. 68
6.4 Engineering stress strain response of the three foam samples at 0.16 relative density. 70
6.5 Relative Young's modulus plotted against relative density for Ti–6Al–4V foams from this work against the prediction from the model of Mortensen et al. [35]. Additionally, data points are included for other additively manufactured foams from Murr et al. [22]. 71
6.6 Relative Young's modulus data matched against the model from Ref. [35], including a knockdown parameter of 0.053. Error bars represent the standard deviation within tested samples. 71
6.7 Compressive resistance against relative density of the Ti–6Al–4V foam. Multiple fits can be observed from Eqs. 3.7 and 3.8. Error bars represent the standard deviation within tested samples 72
6.8 The metal flow stresses for all foam samples, the variation with relative density is represented. The error bars represent the standard deviation. . . 73
6.9 Flexural strength variation for fully dense rods of diameters up to 1.5 mm. The error bars represent the standard deviation. 74
6.10 Figures (a)(b) and (c) show a Widm*ä*statten $\alpha + \beta$ microstructure within samples of 0.56, 0.744 and 1.8 mm diameter. Figures (e)(d) and (f) show the respectively microhardness Vickers maps. 75

6.11 Surface representation obtained from the XCT scans for strut diameters of 0.56, 0.744 and 1.8 mm. 75
6.12 Variation of the porosity volume fraction in different strut diameters. 76

7.1 a) Unit cell designed as the minimum repeatable symmetric unit, b) Samples populated with the unit cell, c) Cross section profile as an octagon of diameter "*d*", d) Lattice front view showing dimensions of sample length "L" upon compressive load. 80
7.2 EBM manufactured Ti-6Al-4V scaffold samples. The STL strut diameters were 0.8, 1, 1.5 and 1.8mm. 80
7.3 Microstructural features in "As built" bulk microstructure: (a) Lattice build orientation from top to bottom, (b) columnar β prior grains, (4c) $\alpha+\beta$ wave basket microstructure and (4d) diffusionless α'martensite. 82
7.4 X-ray diffraction scans of Ti-6Al-4V lattice truss sections in; a) as built EBM condition, b) 960°C/2h/FC and, c) 1200°C/2h/FC samples 83
7.5 Microstructure of lattice specimens; (a) and (b) after 960°C/2h/FC and 1200°C/2h/FC heat treatment respectively. Tensile specimen microstructure; (b) and (d) after 960°C/2h/FC and 1200°C/2h/FC heat treatment respectively 84
7.6 a) Alternating α and β lamellae packets, b) Equiaxed grains with a α plates-like and α grain boundaries across the lattice strut member 85
7.7 A lattice stress-strain curve for each condition from batch 3 showing linear behaviour followed by the maximum peak resistance and failure as a sudden drop in stress supported. 86
7.8 Compressive resistance found in lattice samples compared to current models for cellular materials with a C constant of 0.3. 88
7.9 Experimental data and analytical model prediction. The buckling failure mode was calculated as the height of one layer with nodes built in that cannot rotate therefore using a column effective length factor k of 0.5. . . . 89
7.10 Silhouette images from the video extensometer showing the pre-test and post-yield (pre-failure) forms of samples from batch 1 (a, b) and batch 4 (c, d). 89
7.11 SEM images of the node fractures for the compressed specimens, 0.8, 1, 1.5 and 1.8 mm in diameter respectively. A transition in fracture can be seen from a "dimpled" one to a cleavage fracture. 89
7.12 Experimental compressive yield strength values compared to predictions from parent material properties. "As built" samples falling within a 1.8% deviation, 9600°C/2h/FC samples within 2.7% deviation and 1200°C/2h/FC within 11% deviation. 90
7.13 Porosity volume fraction with the distance from the outer contour for strut samples S1 to S7. Two main depths from contours can be appreciated at approximate 60 and 400μm. 92
7.14 Comparison of melted zones with strut diameter. (a) Shows one contour and (b) the full contouring region. (c) Shows contouring plus hatching stages. (d) Illustrates the corresponding CT strut slice selected at a random height. 93
7.15 Appearance of shear bands in struts of a cubic lattice after being loaded axially. 94
7.16 Magnification of the shear band zone in fractured struts of a cubic lattice after being loaded axially. 94
7.17 Schematic view of the hat specimen showing the key dimensions. 95

7.18 High speed camera shots indicating the accelerating time prior the impact by the bar(right side) to the hat specimen (shown in the left side). 95
7.19 Output voltage gauge signal with displacement converted from the speed recorded out of the camera. The curves show a maximum for samples B to F close to 0.2 mm, indicating the onset of localisation. 97
7.20 (a) Adiabatic shear band developed after the compression of the hat specimen where the shearing zone can be appreciate along the failure.(b) the deformed zone in between the lamellar $\alpha+\beta$ matrix. (c) shows the deformed zone at higher magnifications. 97
7.21 Thickness of the adiabatic shear band with axial displacement from impact. 98
7.22 Adiabatic shear bands found in the hat specimens. (a) The only specimen with a non-homogeneous shear band in agreement with the lack of localisation in the impact curve, (b to f) show well delimited shear bands within the $\alpha + \beta$ microstructure. 98
7.23 Single line Vickers hardness measurements. A lower indentation resistance can be seen as the distance form the shear band increases. 99

8.1 Schematic figure of a diamond-like geometry where the carbon atomic positions represent the nodes. (a) a perspective view, (b) a front view 101
8.2 Schematic figure showing the trusses meeting at a node showing the top and lower part of the magnified intersection. 103
8.3 Relative density curves for diamond lattices in terms of node length-profile diameter ratio based on ideal circular cross section, boolean operations, analytical squared cross section and experimental values. 104
8.4 Schematic triangle tessellation with an offset of $40\mu m$, this value represents the smaller size of a powder particle and the approximated surface roughness found in these materials. The trace of an ideal circular shape for all truss diamond lattices diameters is also shown. 104
8.5 Mechanical properties of a diamond lattice under compressive loading with variation in relative density. 105
8.6 Diagram of a uniaxial loaded beam element. 105
8.7 Mechanical properties of diamond lattice samples of aspect ratio of 1 and relative density of 0.15. 107
8.8 Mechanical properties of diamond lattice samples of aspect ratio $L/H > 1$ and relative density of 0.15. 107
8.9 Schematic view of the three lattices at different heights of (a) cubic, (b) diamond-like and (c) re-entrant cube. Inserts on the node connectivity are highlighted. 108
8.10 Scanned geometry of (a) cubic, (b) diamond, (c) re-entrant cube. 109
8.11 Pore volume fraction found in the three orthogonal planes of (a) cubic, (b) diamond lattices and (b) re-entrant cube lattice. Virtual slice images showing pore populated regions in the highlighted peaks are inserted for each plot; the diamond at 17.9 mm in the y direction, the cubic at 1.66 mm in the z direction and the re-entrant cube at 9.98 mm in the z direction. . . 110
8.12 Number of pores found for the three lattices; Cubic, re-entrant and diamond. 111
8.13 Compressive response of cubic, diamond lattices and metallic foams at quasi-static strain rate. A response of diamond under dynamic conditions is also included. 112
8.14 High speed stills during the impact of diamond lattice cylinder of $\rho = 0.02$, the time recorded was (a)0, (b) 315, (c) 577, (d) 892, (e) 1260 and (f) $2625\mu s$. 113

8.15 High speed stills during the impact of diamond lattice cylinder of $\rho = 0.06$, the time recorded was (a)0, (b) 110, (c)263, (d)315, (e)368 and (f)638μs. . . 113
8.16 (a) CT scan of the $\rho = 0.02$ diamond sample after a HB impact where the fractured trusses are appreciated. (b) The $\rho = 0.06$ diamond cylinder sectioned showing the deformed zone at around 15mm inside. 114
8.17 Illustration of trusses in a diamond lattice. (a) the family of trusses as wires going from top to bottom plates and unconnected wires are highlighted, (b) Four families of wires can be distinguished in the quaternary direction, (c) Plane parallel to the Z direction and (d) the top view. 114

10.1 Fracture tearing loading mode showing the fracture direction developed upon bending forces within strut elements. 120

List of Tables

1.1 Additive manufacturing technologies of titanium alloys [36] 6

2.1 Chemistry required for cast (ASTM F1108)^a and wrought condition (ASTM F1472)^b 16
2.2 Principal areas and sub-areas to develop themes for EBM. 24
2.3 EBM main parameters and definition 25
2.4 Mechanical properties of Yield strength (YS), Ultimate tensile strength (UTS) and elongation percentage found in tensile testing of *Ti-6Al-4V* processed by EBM.*Non-machined tensile coupon. 30

4.1 Standard 70μm ARCAM Melt, Net, wafer, preheat I and preheat II themes including beam parameters of current, speed, speed function (SF), focus offset (FO), line offset, line order and offset to contout (OC). All values applied at a constant vacuum process of $2 \times 10^{-3} mbar$. 46

5.1 Beam current, speed and focus offset of the weldtracks under study. 54
5.2 Experimental measurements of melt pool and numerical depth values using $\eta = 0.8$, 7W/mK of thermal conductivity, $T_m = 1660$, 580 J/kgk of heat capacity [37]. 55
5.3 Chemistry composition in wt% before (powder) and after (solid sample) the EBM process. 61
5.4 Mechanical properties of the tensile specimens. 61

6.1 Mean properties of the 5 set of samples after manufacturing and compression testing 69

7.1 Comparison between specified and observed strut diameters and relative densities for the “as-manufactured” lattices. The uncertainties were estimated based on the standard deviation from each batch of samples. 81
7.2 Microstructural features and mechanical properties comparison for the lattices and tensile samples in the three conditions under study 86
7.3 Microstructural features and mechanical properties in lattice and tensile samples 92
7.4 Test conditions and results form the impacted hat shaped specimens with an impact speed of $\approx 26.5 m/s$. † The deformed area found in sample A seems unclear to be ASB. 96

8.1 Lattice diamond features of unit cell size, virtual strut diameter ϕ, scanned strut diameter ϕ_{CT}, ideal analytical, boolean, adjusted (with CT mean diameter) and experimental relative density. 102

Nomenclature

Material phases

α	Titanium alpha phase
α'	Martensite phase
α''	Orthorrombic martensite
β	Titanium beta phase
ω	Omega phase

Physical properties

T	Temperature
T_m	Melting temperature
T_0	Material temperature
k	Thermal conductivity
$\boldsymbol{\alpha}$	Thermal diffusivity
ρ^*	Porous material density
ρ_s	Parent material density
ρ_r	Relative density
d	Diameter
t	Thickness
l	Length
L	Material length
h	Height
V_s	Solid volume
V_u	Unit cell volume
V_s	Volume of cylinder
V_{I2}	Volume of two intersecting cylinders
V_{I3}	Volume of three intersecting cylinders

Mechanical properties

σ	Stress
ϵ	Strain
E	Young's modulus
E^*	Porous material Young's Modulus
E_s	Parent material Young's Modulus
σ^*	Porous material failure strength

σ_s	Parent material yield strength
τ	Shear stress
γ	Shear strain
$\dot{\gamma}$	Shear strain rate
σ_{pl}	Plateau stress
ϵ_d	Densification strain
$\dot{\epsilon}$	Strain rate
$\dot{\epsilon}'$	Macroscopic strain rate
ϵ_t	Strain pulse
$\dot{\theta}$	Plastic hinge rotation
σ_d	Densification stress
$\bar{U}$	Absorbed energy
δ	Beam deflection
F	Applied force
M_p	Plastic moment
M	Bending moment
I	Second moment of area
$\dot{v}$	Impactor speed
ρ_d	Density after densification
d_{th}	Beam depth
L_s	Span length
d_l	Indenter diagonal length

Electron beam parameters

η	Beam efficiency
q	Beam power
v	Beam speed

Constants

π	Constant
r	Radius
$\mathbf{R}$	Radial distance
x	Dimension
c	Constant
n	Constant
n_x	Number of unit cells in the x direction

n_y	Number of unit cells in the y direction
C	Constant
C_1	Constant of proportionality
C_2	Constant of proportionality

Abstract

Electron beam melting (EBM) has been used to manufacture *Ti-6Al-4V* micro-truss materials for light weight mechanical applications. Several structures were examined, including a cubic lattice, a diamond structure and randomly-structured foams. The "As-built" material, after the selection of processing parameters and fabrication, has been characterised at a micro and macro level through optical microscopy (OM) and x-ray tomography (XCT) respectively. In order to assess the beam penetration and dimensions of the material after the deposition, a numerical method was employed to study the heat source interaction with the metal to be melted. Fabricated structures were evaluated after compression testing, identifying the collapse behaviour. The influence of the microstructure was investigated in the "As-built" condition and after post-builds heat treatments at lower and higher temperatures than the $\beta - transus$. From this study, is it suggested that the incidence of volumetric defects from the additive manufacturing (AM) process influences the mechanical resistance and performance more dramatically than the bulk material properties. Additionally, due to the nature of the alloy system with work hardening and low heat conductivity, the observed failure mode was related to the development of adiabatic shear bands. This type of failure was characterised by deformation at high strain rates through Hopkinson bar tests.

Acknowledgements

I want to thank my supervisors, Prof. Iain Todd and Dr. Russell Goodall for their invaluable guidance in my research project. Their prompt advice was fundamental on the realisation of my PhD. I also want to thank Prof. Bradley Wynne and Dr. Martin Jackson for their helpful discussions. To the experts I could collaborate on their respective subject, Prof. Harm Askes and Dr Andrew Tyas from the department of Civil and Structural engineering of this University of Sheffield, Prof. Philip Withers and Dr. Fabien Leonard from the School of Materials at The University of Manchester and, Prof. Fernando Fraternalli and Miss Ada Amendola from The University of Salerno in Italy. Also, I want to express my gratitude and appreciation to Mr. Dean Haylock, Mr. Ian Watts and Mr. Alan Hindle for passing a bit of their knowledge and experience.

I want to thank The University of Sheffield and the department of Materials Science and Engineering for giving me the opportunity to start an amazing career. Thanks to my sponsors CONACyT and the Roberto Rocca Fellowship Program.

I also want to thank the colleagues-friends who I made an incredible teamwork learning cool stuff, singing, dancing... not necessarily out the department. Amit, Chris, Fatos, Fergus, Itzel, James, Jon, Lampros, Laura, Meurig, Sam, Sarah. To my family and girlfriend who supported the non-scientific side of the person undertaking this enterprise, I'm so lucky to have you all.

Analysis, the interminable quest of untangled relationships...

1

Introduction

Additive manufacturing

Additive manufacturing (AM) has arrived as a promising route capable of fabricating almost any conceivable shape. The approach reduces the complexity of forming the three-dimensional shape through the addition of material as a stack of slices, with each layer consecutively added on top of the previous stack. This basic and fascinating approach has made AM the subject of serious discussions, with some declaring it to be a revolution for manufacturing [38].

The point of these assertions can be understood if traditional manufacturing processes are analysed. While materials made by the "conventional" routes (that is moulding and forging) display a longer chain of production, the processing steps in AM are constant no matter how intricate the shape may be. With the shift in how processing is performed, it is also a great opportunity for designers and manufacturers to come together to tackle common background problems, or for personal designing and manufacturing skills to be improved on an individual basis. Either way, the versatility of the process and the computational power available nowadays are pushing design concepts to the limit. The creation of either organic or geometric shapes are realising idealised materials never previously processed. From many centimetres to nanometres, new materials are now possible in medicine, science, engineering and arts. The development and manufacturing contribution to such fields has been taken to unthinkable levels.

However, not everything is plain sailing. As a relatively new manufacturing route, the potential and capabilities are still being established. The creation of challenging geometries requires reliable material deposition strategies, capable of manufacturing to the demand of virtual designs, even at nanoscale [39], or in different areas of materials (polymers, ceramics or metals [40]). However, each of these areas face fundamental problems that require attention in order to continue with their progress. In the area of metallic materials for example, physical conditions of oxidation, non-equilibrium wetting, epitaxial solidification, metal vaporisation are some of the issues that need to be addressed prior manufacturing additively [41]. Different processing approaches are therefore available in selecting those materials that are more pertinent to be manufactured by either one or another technique.

In regard to metallic materials the AM processing can be generally divided in two categories, direct deposition techniques and powder bed fusion processes [36], see table 1.1.

Table 1.1: Additive manufacturing technologies of titanium alloys [36]

AM category	**Technology**	**Company**	**Description**
Direct energy deposition (DED)	Direct Metal deposition	DM3D Technology LLC	Laser and metal powder used for melting and depositing with a patent closed loop process.
	Laser engineered Net shaping (LENS)	Optomec Inc.	Laser metal power used for melting depositing
	Direct manufacturing	Sciaky Inc.	Electron beam and metal wire used for melting and depositing.
Powder bed fusion	Selective laser sintering (SLS)	3D system corp.	Laser and metal powder used for sintering and bonding.
	Direct metal laser sintering (DMLS)	EOS GmbH	Laser and metal powder used for sintering, melting and bonding.
	Laser melting (LM)	Renishaw Inc.	Laser and metal powder used for melting and bonding.
	Laser melting (SLM)	SLM solutions GmbH	Laser and metal powder used for melting and bonding.
	Laser CUSING	Concept Laser GmbH	Laser and metal powder used for melting and bonding.
	Electron Beam Melting (EBM)	ARCAM AB	Electron beam and metal powder used for melting and bonding.

Among all these routes, Electron Beam Melting (EBM) is becoming increasingly used due to fast processing times, reduced waste of input materials and minimum post processing steps such as heat treatments for elimination of residual stresses [26]. However, limitations of the final product and capabilities of their applications are present in various ways and forms. As an example, the lack of understanding and poor predictability of material micro and meso-structure is continuously present. Hence the obtained mechanical properties are in some cases similar to conventional processing routes, and in some others lower than expected i.e. fatigue properties [36], requiring extensive catalogues of reported properties in order to reduce uncertainty.

To some extent, all this lack of understanding can be attributed to the many process variables involved in the EBM system, controllable and uncontrollable. This is due to the prototyping nature that, even nowadays, the EBM route is characterised by. Such variables however, have been studied progressively during recent years, clarifying their influence on each stage of the process, material input characteristics (particle size, morphology and chemistry), the melting strategy and heat management as the processing and, assessment of the output material properties, see figure 1.1.

Figure 1.1: Schematic representation of the EBM process of their three consecutive stages.

Currently, EBM is employed to develop fully new and up-to-date materials that would be problematic to process under conventional methods such as casting. $Ti-6Al-4V$ and $TiAl_3$ and Nickel super-alloys for jet engine components are some examples. These materials that present segregation and oxidation issues during their processing, excessive waste of raw materials, and usually a long chain-production with complex processability, etc., are examples of what the EBM technology can be used for thanks to the use of inert atmospheres, re-use of raw materials capability, and highly efficient heat sources [42].

Additionally, from the geometrical point of view, the freedom that EBM provides testes the proof of the concept in various ways. Intricate architectures, stochastic, non-stochastic and optimised designs can be produced easily. Such materials, part of the cellular solids area, are characterised by having trusses or interconnected membrane systems that may find extreme difficulties if processed by other routes. Biomedical implants such as prosthesis, requiring precise degrees of density in order to match bone or tissue stiffness are some examples [43].

In regard to this, EBM seems to be a good candidate due to the capability of processing complex geometries with biocompatible materials too [44]. However, as mentioned earlier, materials can display a wide variety of properties. This in part can be attributed to the complexity of the process, the applied heat can create heat gradients high enough to modify the bulk properties significantly or, a fraction of defects in the form of pores and cracks reducing the final properties.

The basis of the current research work, is to study an important part of AM processing, isolating a small number of variables and studying them in order to contribute to the AM pool of knowledge. More concisely, the aim is to use Electron Beam Melting to process materials consisting of structures interconnected through truss members with the potential to be applied for biomedical implants and structures for light weight applications.

Project aims

The present research aims to contribute to the field of cellular solids manufactured by Additive Manufacturing and more specifically by Electron Beam Melting. Such aims can be organised as follows:

1. Analysis of the processing parameters on the bulk microstructure obtained in the Ti-6Al-4V alloy system
2. Study of the output microstructure and properties obtained in the bulk materials
    (a) Microstructural analysis through optical, electronic and atomic diffraction techniques.
    (b) Evaluation of properties through destructive and non-destructive techniques, e.g. compression, tension, hardness, metallography, etc.
3. Investigation of EBM capabilities for intricate porous solids feature size and shape
    (a) Influence of electron beam energy in regard to designs on the geometry to build.
    (b) Influence of deposition strategies on physical features of size and shape built materials.
4. Study of microstructure, heat treated and non-heat treated, in cellular solids processed by EBM
    (a) Analysis and influence of the as-built condition, above and below the β transus temperature of Ti-6Al-4V
5. Investigation of the geometry and failure mechanisms found in cellular solids, stochastic and non-stochastic
    (a) Analysis of materials additively manufactured deformed under bending stresses, axial stresses and/or shearing stresses mainly
6. Investigation of the meso-structure and fraction volumetric defects generated in micro-truss materials by EBM

In order to report in a clear way the results found and the respective analysis of all the studied areas, concerning the manufacturing and mechanical properties of micro-truss materials, the present thesis is structured as indicated by the next chapters. A brief description is added for identification of each.

Chapter 1 is the thesis outline establishing the Introduction and Aims.

Chapter 2 gives a brief overview of titanium metallurgy and electron beam melting.

Chapter 3 is a review of deformation in cellular solids and phenomena occurring at low and high strain rates.

Chapter 4 reports the experimental procedure undertaken for all sets of experiments in this thesis. A detailed description of each technique is included.

Chapter 5 shows the characterisation of the EBM process and the resulting material including the material absorption-melting model and the resulting system alloy microstructure.

Chapter 6 shows the mechanical performance found in stochastic materials and what can be inferred concerning the AM-deposited material.

Chapter 7 reports the mechanical performance of cubic lattice structures and the appearance of adiabatic shear bands as the deformation mode.

Chapter 8 reports the experimental strength of EBM lattices and defect population from the manufacturing process.

Chapter 9 is the general conclusions drawn out of this investigation.

Chapter 10 suggests areas for further investigation in order to extend the knowledge of these materials for potential applications.

2

The physical metallurgy and Electron Beam Melting of *Ti-6Al-4V*

2.1 Physical metallurgy of titanium

The next section is dedicated to the metallurgy of titanium and more specifically to *Ti-6Al-4V* alloy, as this was the material used for this investigation.

2.1.1 Crystal structure

Titanium is an allotropic element that transforms from an atomic hexagonal (hcp) arrangement to cubic (bcc), figure 2.1. This change occurs from phases α to β from temperatures below 882.5°C to higher. Upon alloying, the added elements can favour one or other phase to be stable at room temperature, and are therefore classified as α and β stabilizers. Among the common α stabilizers are: aluminium, gallium, tin and oxygen. For β stabilizers: molybdenum, tungsten, tantalum and vanadium are found [45]. Upon addition of stabilizing elements, the resulting balance would define the phases formed and hence the alloy classification as; α, near α,β and $\alpha + \beta$ alloys, figure 2.3.

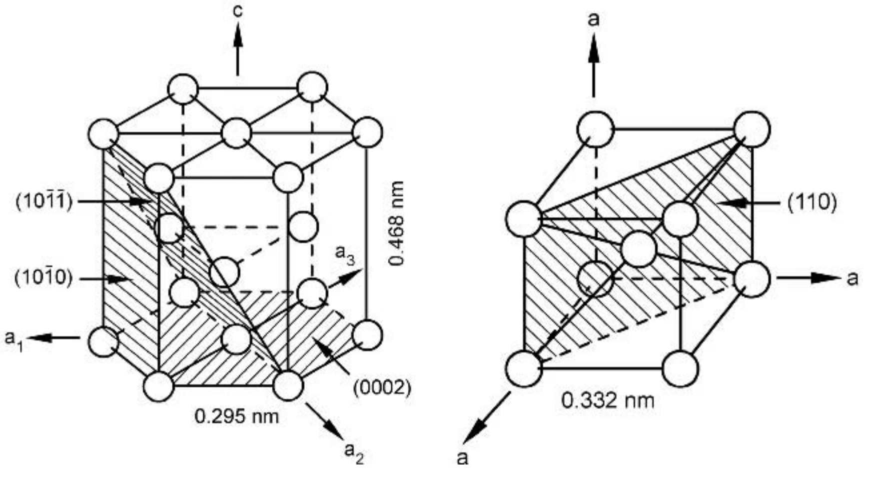

Figure 2.1: Unit cell of "α" and "β" phases showing the most densely packed lattice planes.

2.1.2 Deformation mechanisms

Due to its hexagonal structure, the deformation behaviour of α titanium is through the activation of twinning and slip systems by dislocations. While twinning is observed in titanium commercially pure grade (CP) and α alloys, for $\alpha + \beta$ alloys it is completely suppressed. This is due to the solute content, small phase dimensions and the presence of precipitates, e.g. Ti_3Al. For the β phase there is a similar case where twinning and slip occurs, however the former is limited in β alloys as the solute content increases [45].

Slip deformation

It is well known that deformation by slip mechanisms needs a minimum number of independent systems, which hexagonal structures fail to satisfy [46]. Therefore, upon tensile or compressive loading of a single crystal along the c-axis (see image 2.2) the activation of extra systems would be through shear components called *resolved shear stresses.* If stresses are thus applied along the c-axis, the combination of slip planes and directions (slip systems) close to 45° would be more likely to be activated, i.e. those with the highest Schmidt factor. Evidence concerning the activation of non-basal planes slip has been through the identification of dislocations of type $(\vec{a} + \vec{c})$, which can be observed by Transmission Electron Microscopy (TEM) in titanium alloys [47] .

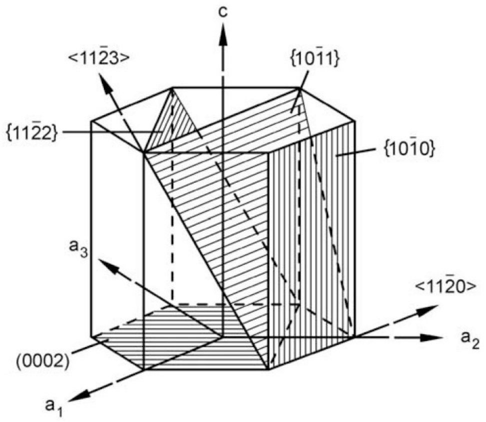

Figure 2.2: Slip planes and directions in a primitive hexagonal lattice.

2.1.3 Alloy classification

α- alloys

This classification is based on a hexagonal structure at room temperature, containing substitutional or interstitial a stabilizers, either alone or in combination. Addition of elements in small quantities with low solubility such as iron, vanadium or molybdenum in low quantity is possible, generating a broad range of α alloys and grades. Although with a limited ductility from its hexagonal α phase, these alloys characteristically have good levels of strength, toughness, creep resistance and weldability [48].

Near α- alloys

Developed to operate at high temperatures, the near α alloys show higher tensile strength at room temperatures than α alloys and excellent creep resistance. Alloyed with small additions of β stabilizing elements (usually below 2%), these can operate at high temperatures with a forgeability improvement in comparison to α alloys [48].

α+ β alloys

These type of alloys are characterised by a relatively high tensile strength and better hot forming compared to α alloys, making them suitable for forged components. With stabilising elements for α and usually 4 to 6% of β phases, the retention of β upon quenching is feasible. Further improvements in strength can be achieved by ageing treatments limited to hardenability effects. With good levels of corrosion resistance, and acceptable properties of yield and fatigue strength up to 400°C [45], these alloys are widely used in aircraft structural parts. Some $\alpha + \beta$ alloys are also widely used for biocompatibility [49] as the case of *Ti-6Al-4V*, employed for medical implants.

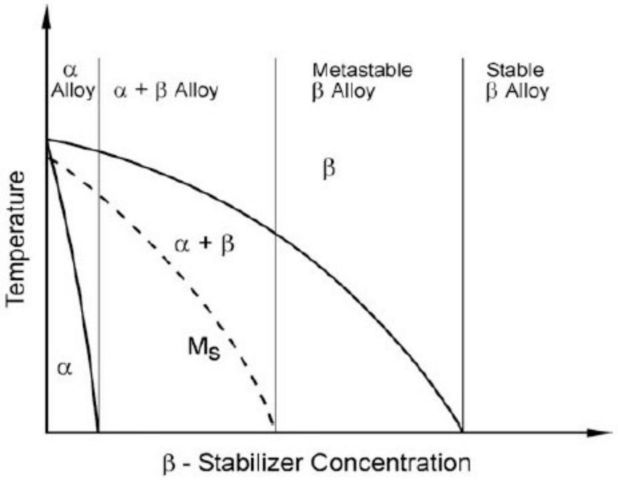

Figure 2.3: Pseudo-binary section through a β isomorphous phase diagram showing α, $\alpha + \beta$ and β regions.

β- alloys

β alloys, in contrast to $\alpha+\beta$, have a metastable or stable β phase that avoids the martensitic transformation. This allows the α phase to precipitate, which forms very fine platelets that can be strengthened by age-hardening. This turns out to be beneficial if an increase yield resistance is required, as higher levels can be achieved than in the $\alpha + \beta$ alloys. An additional advantage is that β alloys can be cold deformed, extending the working deformation range compared to the $\alpha + \beta$ alloys. A better hardenability is an extra advantage, because of the presence of a high content of solutes allowing the hardening of thick sections during heat treatment[48].

2.1.4 Phase transformation

Depending on the cooling rate and the alloy composition, the transformation from β to α in titanium can occur martensitically or by controlled diffusion. In any case, the crystallographic relationship is given as:

$$(110)_\beta \parallel (0002)_\alpha$$

$$[111]_\beta \parallel [1120]_\alpha$$

Martensitic transformation

In the martensitic transformation, a shear type process is what defines the transition from bcc to the hexagonal lattice, figure 2.4. Reduced into different shear systems, the morphology of the martensite (α') is highly dependent (as classified) on the solute content. For pure or dilute alloys, the martensite is usually called "lath" or "packet" and, "acicular" for higher solute content. While the pure titanium martensite is a large irregular region, the acicular martensite consists of individual plates with a high dislocation density and supersaturated β stabilizer elements [5]. It is reported that further addition of alloying elements leads to the distortion of the hexagonal lattice, generating an orthorhombic martensite (α'') [48].

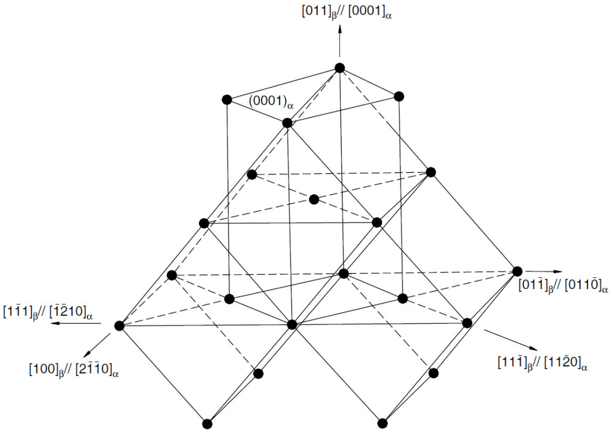

Figure 2.4: Derivation of the closed-pack hexagonal cell from the bcc lattice.

Nucleation and diffusional growth

Upon low cooling rates from the β region, the α phase nucleates along the prior β grain boundary as a continuous layer. Further growth then takes place along the β grain boundary or in the α layer as parallel plates form α colonies. Therefore a population of colonies, each formed of α plates and retained β, coexist up to half the size of the prior β grain (see figure 2.5b). If the cooling rate increases, the α plates become smaller and the nucleation of additional colonies begin at the boundaries of other colonies minimising the elastic strains. Such growth is carried out by contact point in a semi perpendicular direction leading to the called "basket-weave" microstructure [37].

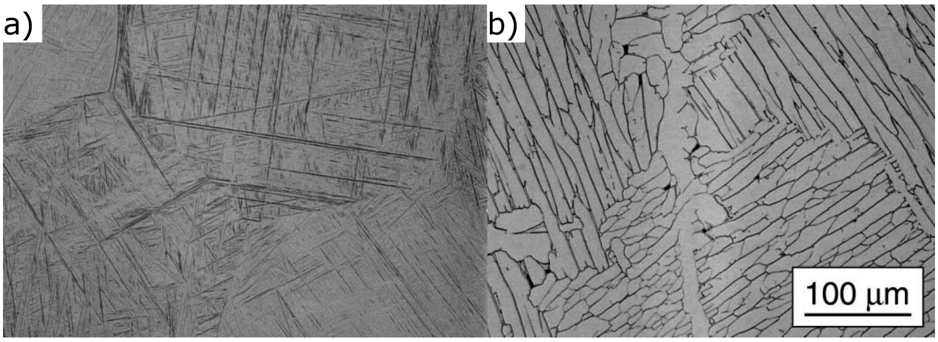

Figure 2.5: Ti-6Al-4V transformed microstructures from 1040°C after: a)water quenched to room temperature and, b) furnace cooling [1].

2.1.5 Strengthening mechanisms

The strengthening mechanisms that titanium can exhibit are due to solid solution, dislocation density, boundary hardening and precipitation hardening effects.

Solid solution hardening takes place in the α phase mainly by the presence of elements in solid solution of larger atomic size than titanium. Among these elements are Al, Sn, Zr. Interstitial elements on the other hand, e.g. oxygen, nitrogen, also increase the yield strength in titanium. This can be seen from titanium grade 1 to grade 4 where an increase in expected yield strength from 170 to 480 MPa is obtained with gradual increase in oxygen level [50]. On the other hand, quantifying the hardening in the β phase only is difficult because of the partitioning of α precipitates occurring in the solute content. However, the strengthening can be measured to some extent by measuring the variation in the atomic lattice parameters with the solute content. Such observations have been reported for Fe, Cr and V additions [51].

Precipitation hardening occurs, for example, by coherent Ti_3Al precipitates in the α phase with contents above of 5%wt in aluminium. As they are coherent, these particles are sheared by moving dislocations during planar slip, although there can be extensive dislocation pile-ups. A similar case is found for the precipitation hardening in β phase where two metastable phases, ω and β', are observed [48]. As they are coherent and sheared by moving dislocations, they intensify the localized slip leading to high yield resistance and low ductility.

Boundary hardening comes from the reduction of $\alpha-$colony size, upon cooling at high rates from the β phase in α+β alloys. This also can cause martensitic transformation which creates a high dislocation density, although, it must be considered that the strengthening contribution from martensitic transformation is low [37]. This is due to small elastic distortions in the hexagonal lattice, an opposite case to the tetragonal distortion found for Fe-C alloys.

2.1.6 The *Ti-6Al-4V* system

Among titanium alloys, *Ti-6Al-4V* is the most commonly used and it represents up to half of the sales in the titanium market [48]. Its condition of $\alpha + \beta$ is the result of investigating titanium alloys capable of overcoming the hot forming limitations in alpha alloys. It displays interesting properties such as: high specific strength, bio-compatibility and corrosion resistance, making an excellent candidate for the aerospace industry and biomedical implants [52][53].

The mechanical properties are strongly linked to the processing route i.e. wrought, casting and powder metallurgy, and to the level of impurities from each process. Depending on the application, the aluminium content may reach 6.75 wt%, a vanadium content of 4.5wt%, an oxygen content up to 0.2wt% and a nitrogen content up to 0.05%, with an increase of the strength with a higher content of interstitial elements. The chemical specifications for cast and wrought material are shown in table 2.1.

Table 2.1: Chemistry required for cast (ASTM F1108)[a] and wrought condition (ASTM F1472)[b]

Ti	Al	V	Fe	C	N	O	H
[a]Bal	5.5-6.75	3.5-4.5	<0.3	<0.1	<0.05	<0.2	<0.015
[b]Bal	5.5-6.75	3.5-4.5	<0.3	< 0.08	<0.05	<0.2	<0.015

Condition

Wrought *Ti-6Al-4V* is usually employed in an annealed condition where a good combination of strength, toughness, ductility and fatigue is found. As in the case of a cast condition, a hot isostatically pressed (HIP) step is needed prior to usage. This makes the closure of internal porosity possible, which improves properties of fatigue and weldability [37].

Although the annealed condition is the most common, some other heat treatments are also used. These conditions can involve heat treatments just above the β transus temperature or in the α+β phase field. These changes create properties of good fracture toughness, crack growth resistance and creep resistance. On the other hand, ageing treatments are common processes too. Achieved through solution-treatments in the range of 800 to 1000° C followed by quenching, they generate acicular α martensite structures. This creates the starting condition for further ageing in temperatures between 300 and 600°C [37].

Phases and structures

The α and β phases would be present in different fractions depending on the heat treatment and interstitial elements, achieving different arrangements and microstructural configurations. Such morphologies are generally classified as lamellar, equiaxed and bimodal types, figure 2.6.

Lamellar. The lamellar structures are the product of controlled cooling rates. For structures slowly cooled down from above the β transus temperature, a coarse α phase is nucleated in layers along the boundaries and inside the β prior grain generally known as α "plate-like". If the cooling rate increases i.e. air cooling, a fine needle-like α is generated. Water quenching and annealing treatments usually lead to a much finer lamellar structure resulting in α' martensite structures if the quenching was greater than 900°C and, in orthorhombic martensite α'' if the quenching was carried out from 750 to 900°C [37].

Equiaxed. Equiaxed microstructures are usually the result of thermomechanical treatments. Formed of a combination of extensive deformation plus a heat treatment breaking up of the lamellar structure into equiaxed grains. Usual procedures are composed of a reduction in sections up to 75% plus annealing periods up to 925°C followed by slow cooling rates [52].

Bimodal type. Consisting in α grains in a transformed β matrix, these can be obtained through annealing+quenching+ageing cycles. With the annealing treatment high in the α+β region a bimodal microstructure of equiaxed α and lamellar α+β matrix is achieved. These would generate the conditions for a further quenching step and ageing at 600°C resulting in an α grain size of 15-20μm and α precipitates [52].

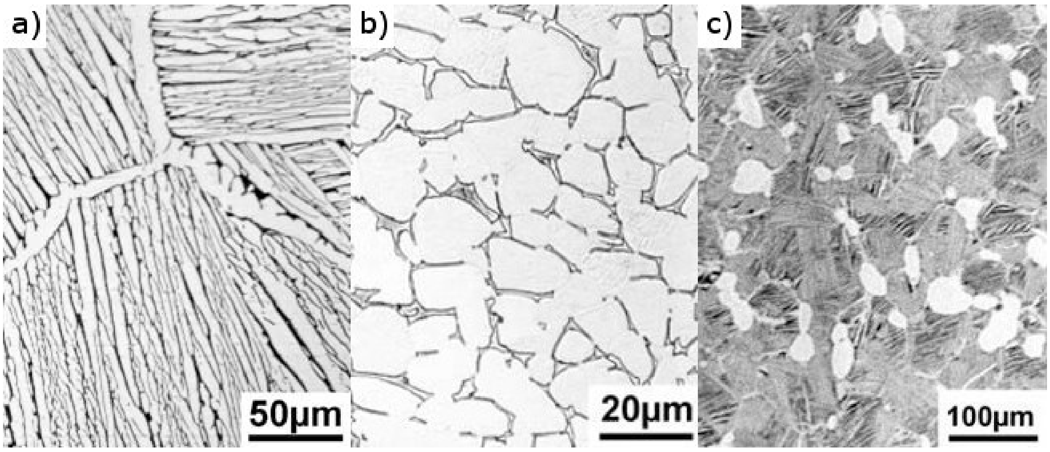

Figure 2.6: Structures found for $\alpha + \beta$ alloys as: a) Lamellar, b) Equiaxed and c) Bimodal type.

Mechanical properties

The Young's modulus of *Ti-6Al-4V* can be found in a wide range going from 100GPa up to 130 GPa. This is because of the multiple phase fraction that can be found and modified by heat treatments [50]. Also, as this alloy tends to develop crystallographic anisotropy, changes in Young's modulus are influenced by changes in texture too. Additionally, the level of impurities, i.e. oxygen pick up, contribute to the variations in the elastic modulus, figure 2.7a.

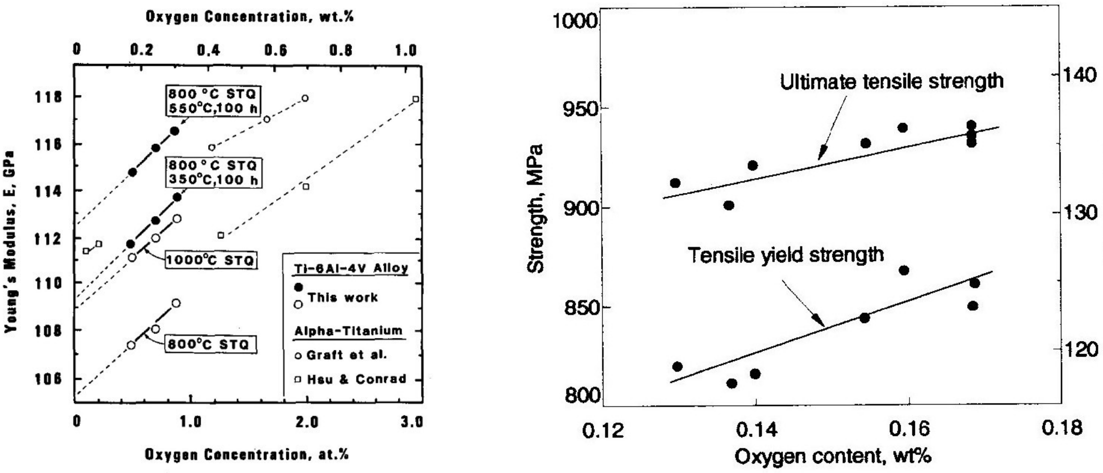

Figure 2.7: Left, the oxygen content and heat treatments on the Young's modulus values[2], solution treatment plus quenching (STQ) for various oxygen contents. Right, the oxygen influence on tensile properties in annealed *Ti-6Al-4V* [3].

On the other hand, the yield strength is influenced by the heat treatment, texture and chemical composition. If the material is subjected to tensile tests, the influence of heat treatments and texture can be up to 200 MPa each, while chemical composition by oxygen increments can be from 70 MPa to 100 MPa, figure2.7b [3]. Under compression, the yield strength exceeds these values slightly compared to tensile loading. This makes *Ti-6Al-4V* a good candidate for structural applications even at high temperatures, up to 540°C.

Influence of crystallographic texture

It has been widely reported that physical, chemical and mechanical properties of crystals depend on their crystalline orientations, i.e. texture anisotropy. For hexagonal materials, the lower number of easy glide systems results in a significant anisotropy compared to cubic structured materials [54][55][56]. From the mechanical point of view, the strong relationship between the crystallographic texture and the deformation modes, e.g. slip and twinning, especially after heavy periods of deformation, plays an essential role in the material deformation.

The result of this intrinsic anisotropy is seen in a variation in Young's modulus as a function of load direction for pure α titanium crystals, shown in figure 2.8 [57]. It is observed that the Young's modulus varies from 145 GPa to 100 GPa when the stress axis is parallel and perpendicular to the C axis respectively. However, for polycrystalline α titanium, the variations are not that pronounced making them more dependent on the intensity of the texture.

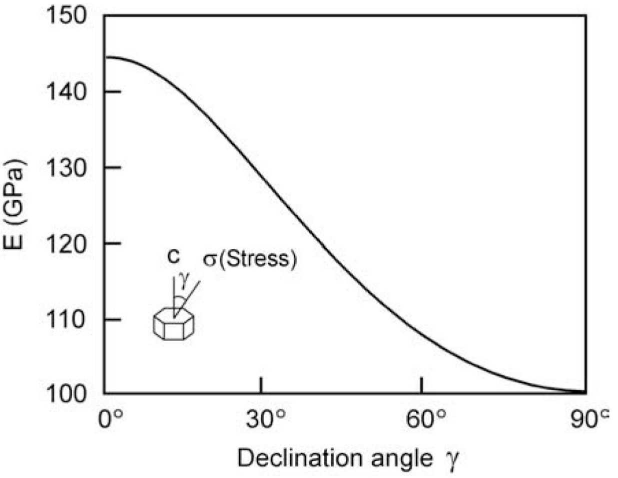

Figure 2.8: Stress axis and c axis relationship on the Young's modulus for α titanium single crystal.

As a general classification, the deformation texture in hexagonal materials is a function of the c/a ratio. For materials with an approximated ideal value of 1.633, e.g. magnesium, the tendency is to form slip in the basal slip system $\{0001\}\ \langle 11\bar{2}0\rangle$. For $c/a>$ 1.633 values for Zn and Cd; a combination of pyramidal slip $\{11\bar{2}\bar{2}\}\ \langle 11\bar{2}\bar{3}\rangle$ and basal slip $\{0001\}\ \langle 11\bar{2}0\rangle$ will result. If the c/a ratio is lower than the ideal 1.633 i.e. Ti and Zr, a combination of basal slip $\{0001\}\ \langle 11\bar{2}0\rangle$ and prismatic slip $\{10\bar{1}0\}\ \langle 11\bar{2}0\rangle$ will result [58].

As an example, Bache et al [55] have reported the influence of the strong texture developed in annealed *Ti-6Al-4V* samples loaded parallel to the longitudinal and transverse plate orientations from cold rolled materials. When the material was loaded parallel to the transverse orientation, a fracture after 15° of bend appeared. However, upon loading the material perpendicularly to the deformed direction, the material remained intact to the maximum bending angle, figure 2.9. This can be attributed to the basal plane orientation allowing shear deformation in the longitudinal samples so that slip would be easily accommodated.

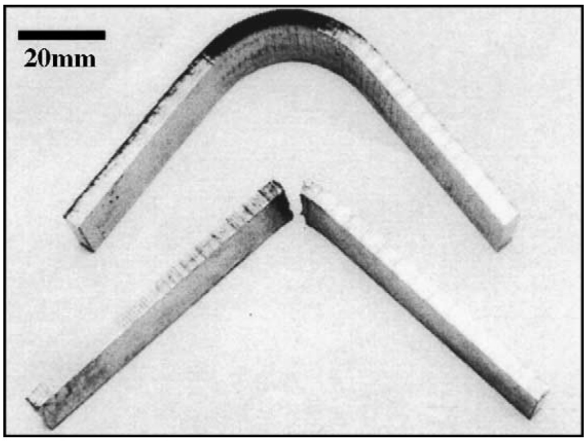

Figure 2.9: Specimens after bending in the parallel direction to the rolling direction (top), and to the transverse orientation (bottom).

2.2 Electron Beam Melting

Electron Beam Melting (EBM) is a powder fusion bed process under the additive manufacturing (AM) umbrella. Initially developed at Chalmers University, today the technique is commercialized by ARCAM at Gothenburg, Sweden. Similarly to other AM processes, EBM technology constructs components layer by layer using an electron gun as an energy source and a powder rake as the material delivery system. The final printed component is the result of a consecutive melting of a sliced 3D model through all layers.

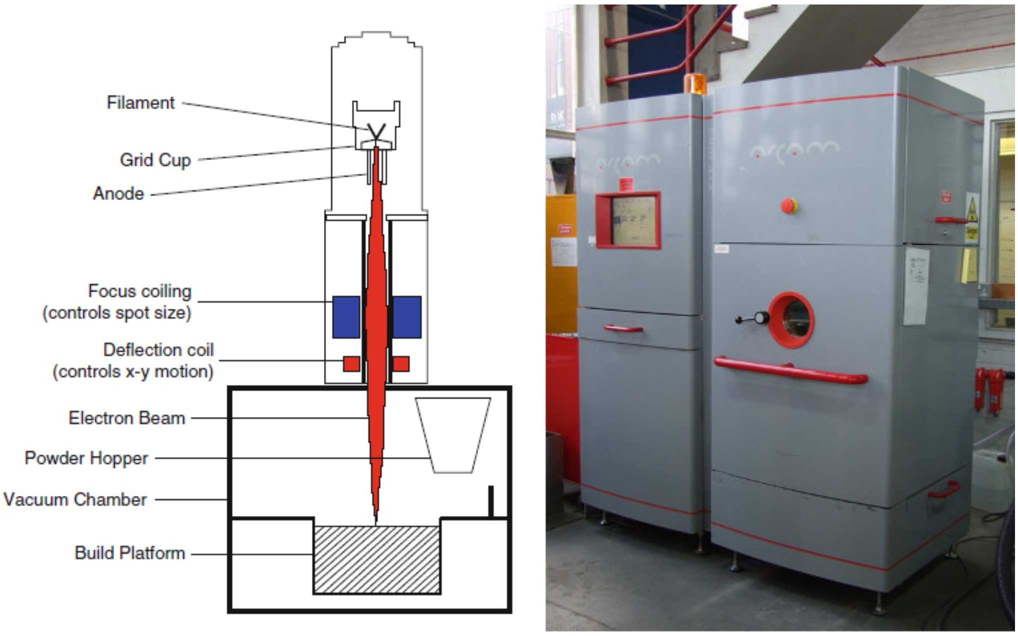

Figure 2.10: Left, schematic figure of the ARCAM system. Right, an image of the ARCAM system S12.

Making use of a highly accelerated beam of electrons, the EBM system is supplied with a high voltage. Immediately after, the electrons are accelerated towards the anode increasing the kinetic energy due to the so called Coulomb forces. During this stage, the output speed in ARCAM systems reaches the order of half the speed of light.

The selective melting process, see schematic figure 2.10, happens with a wide output of settings mainly in speed, power and beam focus offset. Practised in a low partial pressure vacuum, the system delivers significant beam power capable of melting a wide range of conductive materials. The energy absorption by the material, is of course, dependent on the energy of the electrons but also on the conductivity of the alloy and the condition of the raw material, e.g. powder morphology. Such morphology may be of importance when the income of electrons are distributed to the powder bed, therefore, influencing the accumulation and/or dissipation of electronic charge that may be result in arc trips commonly named as "smoke" [59]. On their path through the column (see figure 2.10), electrons are manipulated by two pair of electromagnets. At the time, the electron beam is focused and deflected to a certain position and moved with a certain speed, directed towards the powder bed. It is at this point when the part designed, in the form of CAD coordinates through a surface representation (the STL file or Standard Tessellation Language), are used to control the beam position to melt the parts. The melting is carried out in successive layers of 50-70μm in thickness in routines composed of *Preheat* and *Melting* stages. Such sequence is designed to attempt to minimize the duration of the melting step and thermal gradients by gradually increasing the heat input. It also controls drops in temperature from hardware delays that may exist throughout the layer-up process.

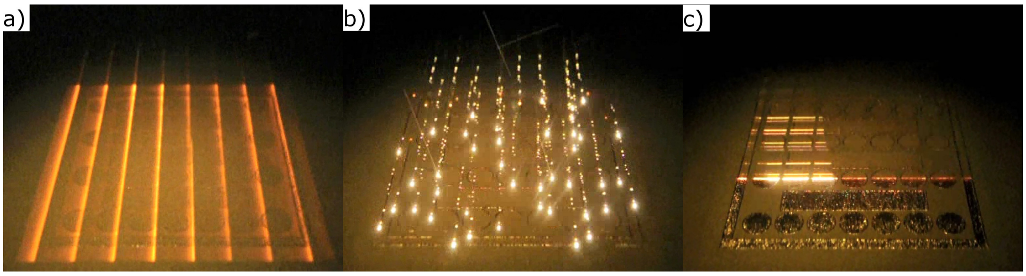

Figure 2.11: EBM stages of preheat, contouring and melting from left to right respectively.

The *preheat* step (2.11a) is usually divided into two stages, *Preheat I* and *Preheat II*. If applied, the *Preheat I* is intended to increase the temperature all across the powder particles in the powder bed. This is achieved by defocussing the electron beam at high levels and moving this across the bed with line patterns and direction defined by the *line order* and *line offset*, see table 2.3. After this, *preheat II* is applied, usually with the same parameters, only at certain offset of the STL contours. This is to retain the heat input in the region of the part to melt as a final preheat step.

The *melt* stage is mainly composed of two parts; the *contouring* and the *hatching*. While the first attempts to minimise the surface roughness, the latter aims for a fast and efficient melting operation. The *contouring* is usually set to melt at lower beam current in *multibeam* mode. This name in reality is the result of the equipment driving the beam at high speeds such that it is capable of maintaining a certain number of *spots* or molten pools at the same time, see figure 2.11b. The *hatching* however is carried out in *single beam* mode (figure 2.11c) according the parameters of *speed*, *current*, *focus offset*, *line offset*, *thickness function* and *turning points* among others, see table 2.3 for description.

2.2.1 Raw materials

In order to develop optimum solid components, the material used needs to fulfil certain requirements, such as having a positive response when absorbing electrons. Powder size distribution and hall flow tests (2.12) are some examples, that, upon adequate properties, it has allowed the manufacturing of copper [60], nickel [61], titanium aluminides [62], titanium grade 2 and *Ti-6Al-4V* alloys [63] to name a few. The versatility of EBM for developing materials has given the opportunity to provide components in areas where the expectations of economic growth are high, such as the automotive, aerospace and medical industries [64].

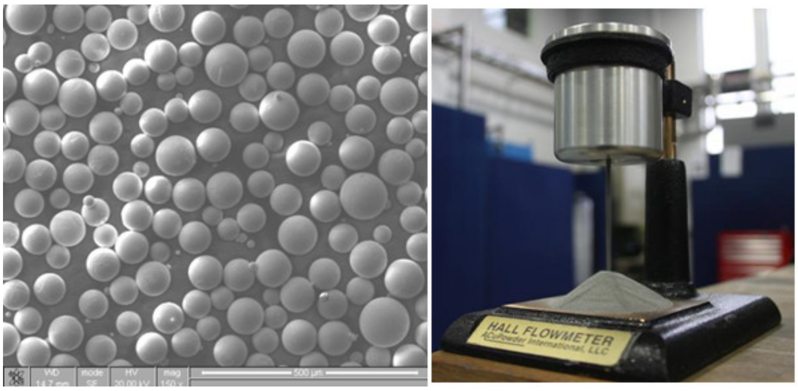

Figure 2.12: Left, SEM figure of spherical *Ti-6Al-4V* power particles. Right, a test of powder particles flowability.

Gas atomized powder

Gas atomized powder is one of the main materials that has been used and commercialised in EBM processes [65]. To create this feedstock particles are generated via disruption of a molten metal stream of liquid by a compressed gas nozzle. Eventually, the disintegrated particles are cooled rapidly to solidification temperatures so they can be collected. Melt temperature, gas pressure and gas-melt impingement angle are of great importance during the processing in order to obtain the particle size range.

Plasma rotating electrode powder (PREP)

Due to spheroidal shapes of atomized powder involves the previous fracture of a stream of liquid, it may have the inconvenience of trapped gas in the powder particle which could be retained even after the EBM manufacturing. As an attempt to minimize the porosity fraction, other atomized powders have started to be explored, with plasma rotating electrode powder (PREP) among those. PREP powder is the result of feeding a wire into a plasma torch where rapid solidified particles are sprayed out. If an alloy is required, input particles can be mixed in order to melt in the plasma [66]. Whichever is the case, the particle size is the result of velocity and temperature reducing considerably the fraction of internal porosity.

Reduction by electrolysis

The reduction of minerals from the ore is necessary to produce some materials, with long pyrometallurgical processing steps, and this can significantly increase the production costs as the case of Kroll's titanium process. As an alternative, the electrolysis process capable of extracting metals and alloys directly from their oxides could potentially be employed in the EBM production chain. Consisting of an electrolyte of molten salt (800-1000) a metal oxide is placed in the presence of a graphite anode. The liquid media under a current extracts the oxide in gaseous state. The output material is further crushed and washed to be ready for use [67].

The main advantage of using a process like this one would be the significant cost reduction [68]. However, comparing the irregular particles produced by these processes with the traditional spherical morphologies, new challenges would be faced depositing these particles for AM, e.g. acceptable flowability.

2.2.2 3D CAD design

Full conceptualization of the product to be manufactured can take several routes. They can be generated by a computer-user through user-interfaces, e.g. CAD platforms or, through reverse engineering technology from pre-existing models, e.g. 3D scanning techniques.

The usage of CAD in AM is made by a surface representation [38], the STL file (Standard Tessellation Language). This is done by exporting the solid constructed data, from solid to meshed files, figures 2.13a and 2.13b. Such file is composed of a triangles which tessellate to describe point coordinates and vector normals, figure 2.13c.

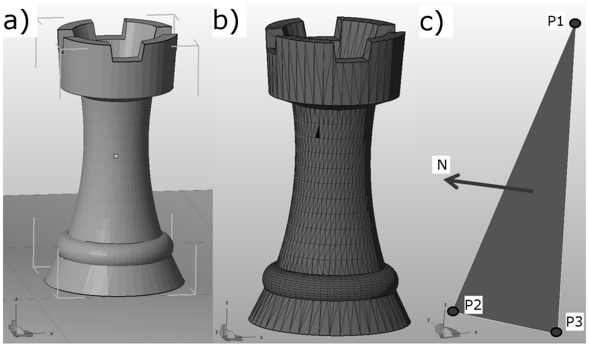

Figure 2.13: STL representation showing; a) design volume, b) triangulated tessellation, c) triangle unit composed of coordinates and normal

Even though the CAD-STL conversion process is automatic, a few errors still can appear. This suggests the solid-to-surface conversion is not so straightforward, involving a restricted offset tolerance in the triangulating operations. Among the common errors are “overlapped” and “intersecting” triangles which vary in the direction of their normal vectors. This eventually turns out to be a significant problem for high surface representations as in lattice materials, creating multiple and repetitive errors (see figure 2.14), causing in some cases a computational crash due to out-of-memory RAM [16].

In any case, the fixing steps can increase dramatically, becoming time consuming. For high surface materials i.e. lattices, foams, etc., the CAD design should constrain the conversion steps in order to minimize further errors. Rounded/organic shapes should be locked to a certain triangulation offset depending on the manufacturing capabilities and design resolution.

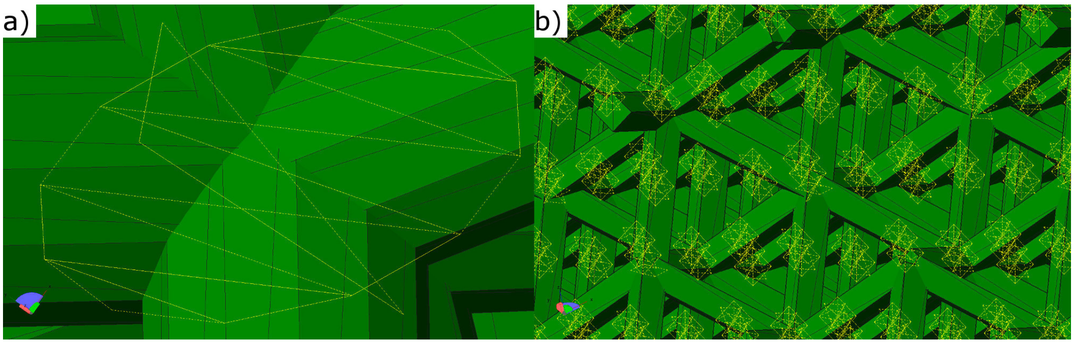

Figure 2.14: Intersecting triangles highlighted in yellow found in STL files; (a) in a single node, (b) multiplied in all connecting nodes.

2.2.3 Processing steps

Once the part has been designed and the model files are fixed, the processing set up is carried out. Consisting of a few steps, EBM (and indeed most of the AM routes) follow the fabrication sequence of:

1. **File transferred to the machine software control.** Initially a 3D representation, a “sliced” file (.abf file standing for Arcam Build File) is inserted and read by the machine software.

2. **EBM machine set-up.** Consisting of the anode and filament, powder bed set-up and powder containers, the process can then be executed unless a machine modification is needed, e.g. extra isolating material for development of high temperature materials.

3. **Build process.** The process parameters to run or investigate as power input, must be set; mainly the deposition speed and vacuums level.

4. **Removal and clean-up.** Once the build is completed, the solid piece remains within a “cake” of semi-loose sintered powder. Through the use of compressed air in a powder recovery system (PRS), the powder is broken down and removed out of the solid. All particle remnants are recirculated for further sieving steps and reuse.

5. **Post processing.** Surface finishing if needed or, in the case of titanium alloys, Hot Isostatic Pressure treatments (HIP) prior to use in the application are in some cases applied.

2.2.4 Design for EBM

A few variables need to be taken into account in order to achieve a pre-designed geometry free of defects and a predicted microstucture. First, the addition of material from powder particles starts with an intrinsic possibility of developing internal porosity [69]. Second, beam parameters need to be optimised to avoid leaving gaps or pores when melting. Third, thermal history is complex as areas on the build envelope may be susceptible to faster cooling rates than others.

As an attempt to control the process and reduce the above issues mentioned, EBM machines use organisational schemes of parameters called “themes”. While some parameters within the theme can be, to some extent, manipulated for further research, some others are part of the industrial know-how, limiting research and experimental replication. Among these are speed-power relationships to melt at a constant depth; this is further explained in chapter 5.

Themes development

As part of the user interface the operator can approach the EBM process through the design of parameters involving heating, sintering and melting through *plate heating*, powder *preheat* and *melting* themes respectively, table 2.2. While the *plate heating theme* is conventionally constant, (usually heating the same plate to the same temperature for a particular material) the other two are frequently varied.

The set theme *Preheat I,* is usually used to obtain a constant temperature profile across every powder bed layer throughout the process. The *Preheat II* theme is constrained to a certain offset, 5 mm off the CAD contour, increasing the particle temperature in the vicinity where the melting step is going to take place. The *melt* theme is composed of scan movements of *contouring* and *hatching*, as in a "drawing" technique for the beam to melt in an organized sequence (although the order is subject to debate). For small sections the *Net* theme is used, capable of working in a similar way as the melt them does but, with a difference in offset to contours avoiding oversized components. The *Point* theme as a variant of the net theme, with the flexibility of being energy optimized in function of time. Finally, the *Wafer* theme is meant to sinter powder particles hard enough to construct support structures for solid components, see table 2.2 for a brief classification.

Table 2.2: Principal areas and sub-areas to develop themes for EBM.

Plate heating	Preheat	Melting
Constant	Preheat I	Solid
	Preheat II	Net structures
		Wafer structures

Depending on the melting strategy, a large number of parameters can be found in a theme. However, only a few directly affect the heat input, these are mentioned in table 2.3. The parameters omitted from this table are described as qualitative only. Among those are: the number of repetitions, parameter compensations and scanning directions e.g. left, right or randomized beam melting patterns.

Build orientation.

A critical step in the EBM planning is the component orientation. While depositions close to 90°angles to the plane of the layers gives the best resolution, depositions close to fully horizontal orientations reduce the properties [70]. As an example, if a part with the form of an "I" shape is to be manufactured, the "laying" position would be preferable against the "standing up". However, if the standing up position, for any reason, needs to be chosen, a few issues have to be considered. First, the negative surface would require the introduction of support structures, e.g. pins, wafers, to avoid any collapsed areas which, in turn, increase the build time and the waste of input material. Secondly, introduction

Table 2.3: EBM main parameters and definition .

Parameter	Description
Beam current	The beam energy component measured in (mA).
Beam speed	The speed in mm/sec at which the electron beam operates.
Focus offset	The focal change above or below the surface product of a positive or negative current value in mA given to the focussing coils, therefore, capable of diffusing or concentrating the beam.
Line offset	The established distance between a parallel line array for the beam to melt in a sequence.
Line order	The defined order at which the scan lines travel on the melting plane; “1234” indicates an order of 1, “1324” an order of 2, etc.
Offset to contour	Used in small sections, close to the size of the weld track width, to account for possible oversized areas, moving the beam to an inside offset from the CAD contour.
Block offset	If applied, prevents sections less than two times the *offset to contour* from disappearing by driving the beam through the guidance of 4 spots placed on the starting beam point from the offset to contour.
Contour length	Is the distance between two points of the four formed when block offset is applied.
Contour overlap	The distance the beam is permitted to move times the *smallest contour length.*
Thickness function	Is the variation in speed due to changes in angle deposition.
Turning points	Is the function compensation of beam speed when changes in melting direction take place.

of new shaped layers to melt would bring along a changing thermal history resulting, in some cases, in swelled areas difficult to control.

It has to be pointed out that EBM faces a key challenge on the addition of material in changing angles as the layer-up process continues. This is related to the new areas to be melted in a slope, as in the case of the overhang in the I shape, figure 2.15. Either through speed or beam power adjustments, the introduced material in the I shape neck would be free of defects only if the right set of parameters are chosen. This would require the capability to adjust the electron beam for the new particles to be melted with no solidified volume below the new layer [71].

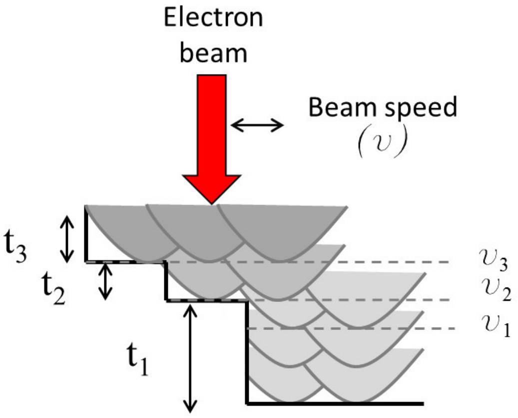

Figure 2.15: Sketch on the speed v adjustment as a function of thickness t.

Heat balance

The build orientation therefore becomes an extended problem related to the *area to melt*, and the heat source; the heat balance. A successful balance of the heat involves applying the minimum amount to avoid cold areas while reducing negative charged-up area leading to failure. At the other extreme, the heat input should not be high enough to cause solid "swelling" losing shape resolution or even evaporation of low melting point elements [41]. Figure 2.16 shows schematically the main variables used to control this balance with temperature from measurements. The *beam current* and *beam speed* as direct variables (mentioned in table 2.3) and speed and current compensations through the *thickness function* and the *turning points*.

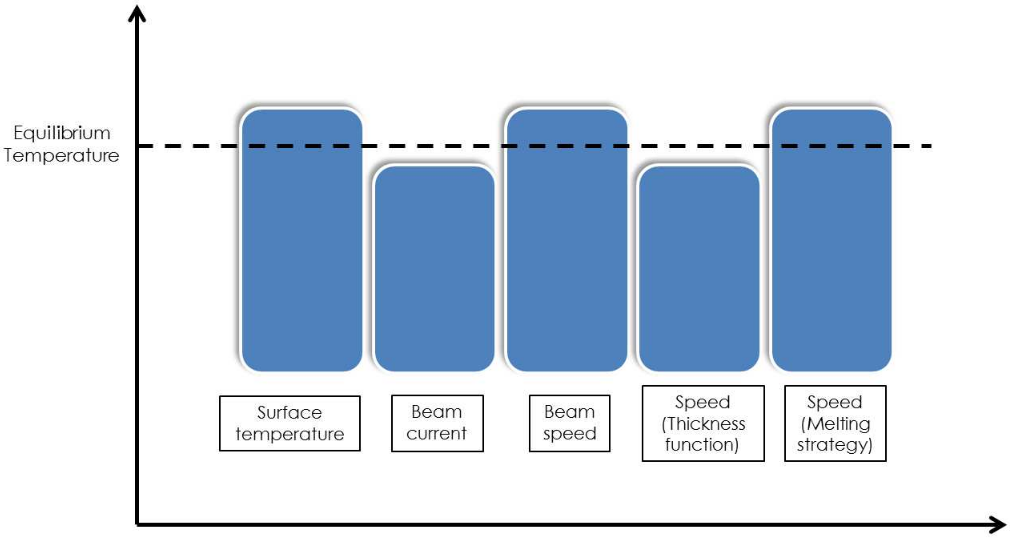

Figure 2.16: Schematic representation of the heat balance in order to reach the equilibrium temperature for materials development.

Beam speed-current correlation

However, beam parameters of speed and current cannot be independently changed. This as a notorious characteristic in the EBM system as the manufacturers allow the manipulation only through arrangements called *speed functions*. As the current and beam speed influence directly the depth of penetration (discussed in the next subsection), these functions are a measure to keep a constant melting depth. However, it is still not clear what these functions are as a non linearity is present in all of them (figure 2.17). It can be suggested that beam depth is subject to hardware capabilities e.g. the system moving electrons to demanded positions at a certain time.

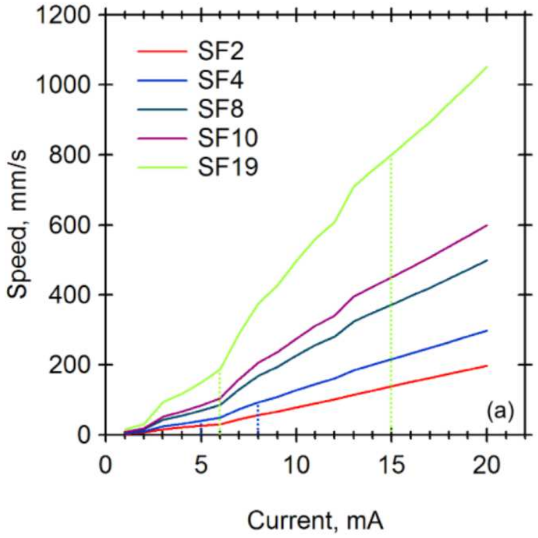

Figure 2.17: Five speed functions (SF) of different speed-current relationship.

Heat source model

In order to predict the required current and its effects on the material penetration, certain assumptions need to be made. Although there are a few models to predict this behaviour [72][73], the heat source can be modelled through Rosenthal's solutions as a basis for prediction of the temperature field [74][75]. Such a model represents a simplified form of the heat flow equation based on the principle of a quasi-stationary thermal state [76]. The major assumptions made by Rosenthal for the model were that the speed of the heat source is kept constant on its moving path, the x direction. Second, there is no heat loss by convection or radiation, and the heat source is distributed by an infinite single point so there is no heat loss with time. Third, the material properties do not change with temperature. The consequences of these assumptions allow the conduction equation to be solved for three dimensions and is shown in formula 2.1.

$$T - T_0 = \frac{\eta q}{2\pi k R} \exp\left(\frac{-v}{2\alpha}(R + x)\right) \tag{2.1}$$

where T represents the melting material temperature, T_0 the material temperature, q the beam power, k is the thermal conductivity, α the thermal diffusivity, $R = \sqrt{(x^2 + y^2 + z^2)}$ the radial distance from the heat source, v is the beam speed. The given solutions and the temperature fields can be seen as a series of isotherms in oval shape, giving the solution to the temperature distribution around the heat source. Therefore, when x, y and $z \to 0$, an infinite temperature is predicted. In the region enclosed by the melt isotherm on the other hand, $T - T_0$ represents the fusion zone and the maximum penetration.

2.2.5 Solidification in Additive Manufacturing

Semiatin & Kobryn [4] have studied the solidification of *Ti-6Al-4V* in a laser melting system, finding a columnar prior-β grain morphology. Such morphology, attributed to the nucleation and growth features during solidification composed of high cooling rates and thermal gradients able to avoid nucleation ahead of the advancing solidification interface. As the alloy system has their own preferential growth (in the (100) direction for BCC metals), this morphology could grow epitaxially in height through several layers. As a validation method, the observations were applied to solidification maps plotting the solidification velocity (R) and the gradient of solidification (G) to predict the microstructure, see fig. 2.18.

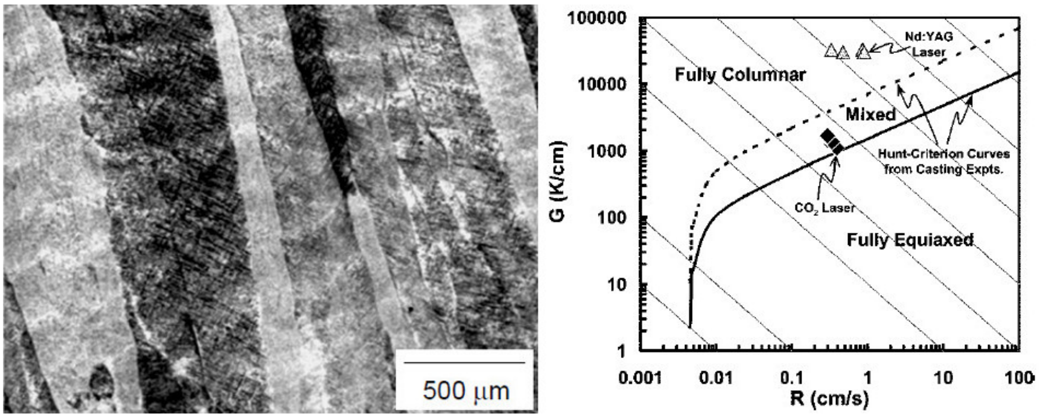

Figure 2.18: Columnar β grain morphology and a solidification processing map for *Ti-6Al-4V* [4].

Furthermore the processing maps were employed by Bontha et al. [74] to characterise the effect of beam speed and beam power in thin walls affecting the grain morphology. Using laser melting systems, their observations indicated a trend towards a mixed equiaxed microstructure as the energy input increased within the local melt pool for *Ti-6Al-4V*. EBM systems on the other hand have been operated to obtain equiaxed microstructures [77] by adjusting speed and power. However, the energy input required was high enough to cause full melting of solid substrates of up to 10 mm in thickness. Such high power makes it undesirable for AM purposes.

2.2.6 *Ti-6Al-4V* microstructures in AM

The $\alpha + \beta$ microstructure of *Ti-6Al-4V* owns its origin to the conditions of solidification and cooling from the β-transus temperature [37]. In EBM systems, it is well known that a gradient of temperature is develop, leaving a trace of columnar grains generated during the first steps of solidification. Additionally, further cooling is so fast that martensitic transformations take place. However, as the addition of material in the layered-up process involves a repetitive cycle of preheating-melting stages (730-680°C [26]), the final microstructure can be seen as a mixture of columnar traces, martensitic and annealead $\alpha + \beta$ laths, see figure 2.19.

On the other hand, the microstructure found in SLM products can differ vastly. As the cooling rates can be higher without consecutive preheating stages, the fraction of martensite is reported to be much higher [9]. Murr et al. [6] have reported *Ti-6Al-4V* microstructures manufactured by SLM and EBM. While SLM products showed a dominated martensitic structure, EBM parts are mainly composed of Widmanstätten/basket wave microstructures. The solidification however, is affected by high cooling rates in a similar way for both systems, leaving traces of β columnar grains throughout the entire build [4][26].

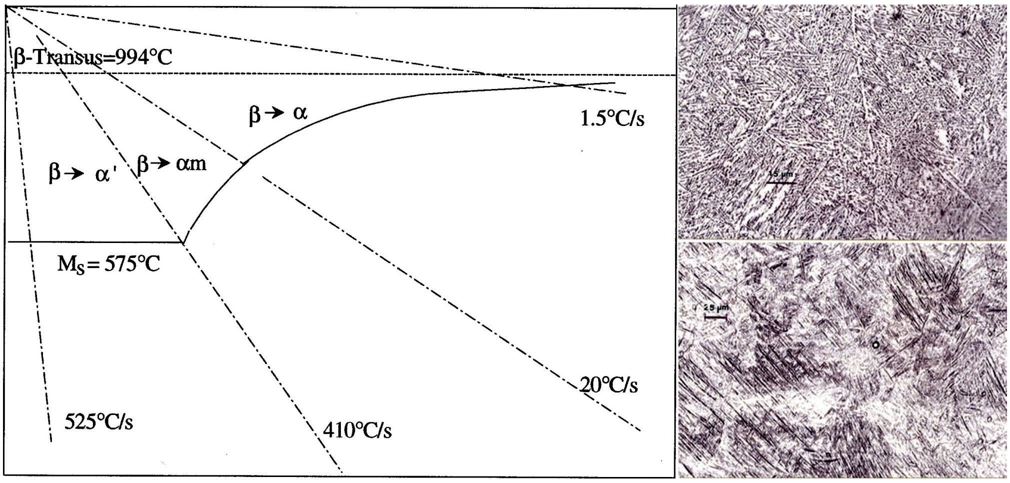

Figure 2.19: A Continuous cooling diagram for *Ti-6Al-4V* after solution heat treatments at 1050°C [5]. The inserted images show the EBM (top) and SLM *Ti-6Al-4V* microstructure (bottom)[6].

2.2.7 Mechanical properties of *Ti-6Al-4V* in EBM

The effect of EBM processing parameters on the machanical properties of *Ti-6Al-4V* has been investigated from the up-to-date literature. Among those reported are; the effect of preheat temperature [26], particle size [78] thickness of layer deposition [78][79], the influence of build direction [31][22][80][81], the effect of part size and distance to build plate [82], the effect of X and Y direction across the powder bed and energy input [80], and the tensile strength on as built coupons [81][83] to name a few. All strength values found were superior to the minimum required by ASTM F1108 and ASTM F1472 standards for cast and wrought material, with the exception of tensile tests carried out on as built coupons. Such exception was attributed to the effect of the surface roughness on the applied stresses leading to localisation during very failing at low percentages of elongation, see table 2.4. Properties found in *Ti-6Al-4V* from other AM routes are reported in figure 2.20 for comparison purposes. As can be seen from table 2.4, a wide range of properties is reported for the same titanium alloy system. Along the values of yield and ultimate strength, the chemical composition is shown when reported in the literature. It can be seen that discrepancies on the reported compositions exist especially for oxygen, potentially attributing those to the storage conditions of atmospheric humidity. It is worth to mention that not all the studies report precise chemical composition of the raw material, making them not straightforward to relate it to the mechanical properties in order to suggest an interstitial strengthening mechanism due to oxygen pick-up. Aside these chemistry variations however, the mechanical properties are mostly reported focusing their study in regard to heat management during the process. As an example, in table 2.4 build orientation is given (as a variable on the heat distribution during the layered process) and

Table 2.4: Mechanical properties of Yield strength (YS), Ultimate tensile strength (UTS) and elongation percentage found in tensile testing of *Ti-6Al-4V* processed by EBM.*Non-machined tensile coupon.

Y.S. (MPa)	**T.S.** (MPa)	**EL.** (%)	**Ref.**	**Build orient.**	**Chemical Composition (%wt.)**
883.7	993.9	13.6	[26]	(Z)	5.74 Al, 4.20 V, 0.228 O
932.4	1031.9	11.6	[26]	(Z)	5.86 Al, 4.19 V, 0.233 O
928.8	1028.9	13	[26]	(Z)	5.73 Al, 4.11 V, 0.246 O
938.5	1029.1	13.2	[26]	(Z)	5.89 Al, 4.20 V, 0.243 O
1125.2	1175.3	20	[31]	—	6.0 Al, 4.0 V, $<$ 0.2 Fe, $<$ 0.25 C, $<$ 0.2 O
1034.5	1110	13.08	[22]	(Z)	—
1101.7	1113.7	11.08	[22]	(XY)	—
952.2	1007.7	12.3	[80]	(XY)	6.1 Al, 4.07 V, 0.22 O, 0.2 Fe, 0.0008 H, 0.019 C, 0.031 N
982.9	1029.7	12.2	[80]	(XY)	6.1 Al, 4.07 V, 0.22 O, 0.2 Fe, 0.0008 H, 0.019 C, 0.031 N
966.5	1017.4	12.2	[80]	(XY)	6.1 Al, 4.07 V, 0.22 O, 0.2 Fe, 0.0008 H, 0.019 C, 0.031 N
984.1	1032.8	9	[80]	(Z)	6.1 Al, 4.07 V, 0.22 O, 0.2 Fe, 0.0008 H, 0.019 C, 0.031 N
961	1008.6	7.1	[80]	(Z)	6.1 Al, 4.07 V, 0.22 O, 0.2 Fe, 0.0008 H, 0.019 C, 0.031 N
993.1	1036.3	11.1	[80]	(XY)	6.1 Al, 4.07 V, 0.22 O, 0.2 Fe, 0.0008 H, 0.019 C, 0.031 N
927.6	1011.6	13.2	[82]	(XY)	5.54 Al, 4.17 V, 0.19 O, 0.21 Fe, 0.0009 H, 0.018 C, 0.029 N
929.5	1010.4	13.7	[82]	(XY)	5.54 Al, 4.17 V, 0.19 O, 0.21 Fe, 0.0009 H, 0.018 C, 0.029 N
783	833	2.7*	[81]	(XY)	—
812	851	3.6*	[81]	(XY)	—
735	775	2.3*	[83]	(Z)	0.31 O
	1028	14	[84]	—	—
	928	3*	[84]	—	—
1150	1200	25	[85]	(Z)	6 Al, 4 V, $<$ 0.2 Fe, $<$ 0.25 C, $<$ 0.2O
1100	1150	16	[85]	(Z)	6 Al, 4 V, $<$ 0.2 Fe, $<$ 0.25 C, $<$ 0.2O

omitting others due to spaces constraint that may be important, those are: preheating powder temperatures[26], energy input, orientation and location [80], distance from build plate and specimen size [82].

Other studies report their bulk properties depending the final application of the component. In dental and medical applications for example [84], were the component may not be required to have a post-process (surface finishing), the mechanical properties are reported from as-built coupons for more accurate estimation of properties. Part of these results are low values of elongation to failure compared to machined coupon specimens.

Comparing the EBM mechanical properties of Ti-6Al-4V with other processes such as Selective Laser Melting (SLM) and Direct Energy Deposition (DED), see figure 2.20, it can be seen that EBM processing has a wider spectrum. Despite the not extensive report,

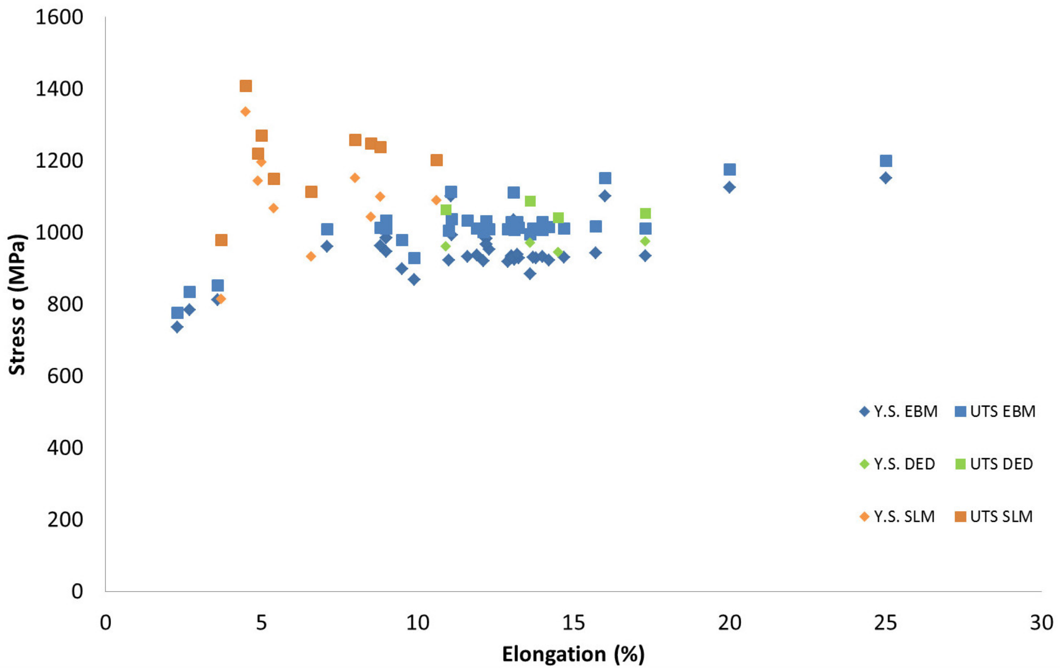

Figure 2.20: Mechanical properties reported for Ti-6Al-4V from various AM routes. EBM from table 2.4, SLM and DED from [7][8] [9][10].

it can be suggested that due to the high number of process variables these influence the thermal history extensively giving a wide range or transformed microstructures and therefore mechanical properties. Such diversity of thermal histories through process parameters can be seen as an advantage for building progressively in order to avoid thermal stresses however, an adequate assessment on heat management needs to be carried out in order to avoid evaporation of low melting point elements or excessive degradation of spherical raw materials [63].

Laser technologies on the other hand seem to fabricate components with different range of properties, higher tensile strengths with lower elongation values. These can be indicative of a much rapid solidification rates modifying the microstructural products in such a way the strengthening mechanisms favour a development of higher tensile resistance, i.e. a finer α lath morphology. As mentioned earlier, laser additive manufacturing routes experience higher cooling gradients [6] to some extent du to lack of preheating stages. Direct deposition methods process materials with yield and ultimate strength in the EBM spectrum of properties and elongation values lower than SLM.

2.3 AM Processing of thin sectioned materials

The processing of thin section materials can be carried out in a similar way as any other component, looking after the geometrical resolution free of defects. However, it is indeed agreed that certain variables need to be adapted prior to manufacturing in order to achieve their best possible integrity. Beam offset to CAD is one example, as thin sections may approach the size of local melt pool or powder particles. Laser processes in this case deliver a smaller melt pools through sharper energy beams [77][86], therefore handling smaller particle ranges to melt capable of building components with thinner sections.

Other issues may be latent when manufacturing thin parts, as an example, power input may accentuate the effects of rapid solidification cooling rate due to less thermal mass. Fogagnolo et al. [11] for example, have reported the microstructural and mechanical behaviour of cubic lattices obtained by SLM. In such study, variations in beam energy were carried out in order to report the influence of beam power to internal porosity fraction. A martensitic microstructure, thinner struts than previous designs and larger pores were achieved. By varying the energy input to high levels, the mechanical properties showed higher strength as well as higher contents in oxygen and nitrogen, suggesting that interstitial elements (oxygen and nitrogen) increased the strength despite a significant porosity fraction found in the specimens.

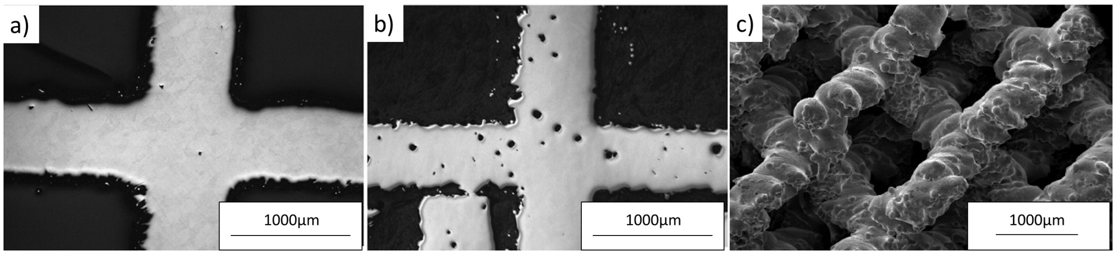

Figure 2.21: Lattices with variations in beam energy when processed by (a) and (b) SLM and by EBM (c). While energy variations in SLM reported significant porosity fractions and different mechanical properties [11], EBM energy changes did not showed a significant variation of bulk properties [12].

In respect to electron beam melting, Körner et al. [12] have reported the effect of energy input per unit length on the mechanical properties of diamond-like lattices. The energy changes modified the relative density through the quality of truss members in all lattices causing a variation in relative density. Such evaluation allowed to systematically characterise the mechanical properties suggesting that these materials can be designed to tailor properties in function of their density for load bearing bone implants. This was further corroborated by Marin et al. [87], who have studied the effect of cellular porosity on the mechanical properties in the same lattice diamond-type. Part of the results have shown that values of lower porosity have a higher mechanical strength while the elastic modulus is almost similar. Additionally, the microstructure (conformed of alpha laths of 0.5μm) was reported to be homogeneous throughout the truss member of the cellular solid, giving resistances to indentation almost identical along the body of the structural element.

Other alloy systems have been explored as well. Ramirez et al. [60] reported the mechanical properties of copper lattice structures focusing their study on the strengthening mechanism of precipitation and its strength contribution to the material. It was concluded that while the mechanical properties in Ti-6Al-4V agree with current models, copper structures showed an increase due to strengthening mechanisms of precipitation hardening.

2.4 Summary

The literature reported in this chapter is concerned to the metallurgical principles for titanium and titanium alloys. As part of this non exhaustive literature recompilation, the EBM process is described following the sequence of equipment description, raw materials, material design and processing. Finally, a few subsections are given to show the reported results of microstructure and mechanical properties found in materials processed by this route. This can be seen as a useful data compilation for material properties that need to be further referred. As reported, multiple process variables can lead to a wide umbrella of properties for the same material, therefore, suggesting a complex reproducibility of results. This arises due to the influence of the heat source (preheating and cooling rates) and a continuous changing chemistry composition of input materials giving microstructures with not necessarily identical mechanical properties. Additionally, as the process degrades the raw material, properties of chemistry lead to multiple side effects of oxygen, nitrogen and hydrogen pick up as well as aluminium evaporation.

3

Deformation in cellular solids

3.1 Introduction

A cellular material is made up of individual cells of free volume interconnected throughout a determined volume. Such interconnection can be through a network of membranes or truss members. This group of materials is so common that they appear everywhere in nature, in some exceptional cases as very light and strong materials, e.g. wood. Because of the structural potential they show, they are the focus of detailed study, particularly to understand the role of the *shape* and *topology* they present, the effect of the variation in *volume fraction* and their parent material properties. In research such materials are mostly classified as metallic/ceramic cellular solids. Studies assessing the mechanical [13], thermal [88], electrical [89] and acoustic [90] properties in function of structural parameters can be found extensively in the literature.

Reference to the shape and topology of the structure is of use in order to classify the different types that are found whether they present a *random* network of pores e.g. foams, sponges, fibre networks, or an *organized* configuration like honeycombs or lattices. This becomes of importance when the material geometry is to be studied, if a degree of directionality is developed, anisotropic properties would most likely be present. For some properties, the degree of geometrical differences is much less significant than the solid fraction in determining the properties. Where the solid fraction is expressed it is often referred as the relative density ρ^*/ρ_s, and sometimes reported as the inverse of this value, the pore fraction $(1-\rho^*/\rho_s)$ the "*" conventionally refers to the cellular material property and the subscript "s" the bulk material property. In this way, properties of Young's modulus, plastic yield strength, thermal conductivity, thermal expansion coefficient, etc., can be systematically tailored to complex geometries [14][91] that can show directionality in their properties as reported in the literature [11][16][19][92][93][94].

3.2 Deformation mechanisms

It is well known that cellular materials can deform by bending or stretching their structural elements, as shown schematically in figure 3.1. Upon loading, the forces acting on a unit cell (figure 3.1b), and the connectivity of their elements would determine the deformation mechanism. While bending-dominated behaviour is characteristic of low connectivity truss materials [13], stretching-dominated behaviour (figure 3.1c,d) is displayed by structures with higher connectivity [95]. Among the important differences between these two behaviours, the stretch-dominated lattices show a higher collapse strength and elastic modulus at same values of relative density than bending-dominated structures. This makes them, in general, good candidates for structural applications. However, as they tend to present a softening after the peak strength (see figure 3.2), their use for energy absorption would not be recommended, as a dramatic failure leads to complete fracture.

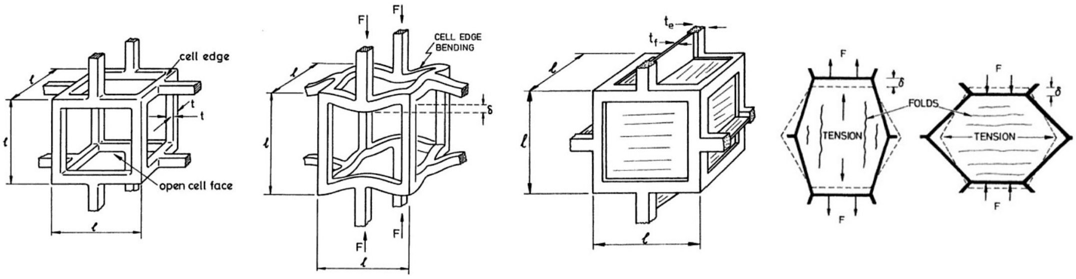

Figure 3.1: Schematic representation of: (a) Open unit cell, (b) bending mechanisms acting as a deformation mode, (c) a closed unit cell with (d) tension deformation within their membrane elements.

3.2.1 Bending-dominated elastic properties

Upon the right assumptions for the conditions in beam deflections, the elastic properties in bending-dominated structures can be predicted. This is achieved if the stiffness of the structural member and the available displacement is known. While for open cellular structures (see figure 3.1a and b) the deflections are only through bending mechanisms, for closed cells (see figure 3.1c and d), the stresses experienced in the beam elements are accompanied by tension-compression of the material in the cell faces. Although it is well known that bending forces acting in cantilevers are accompanied by tension and compression [96], the tension-compression experienced in closed cellular materials contributes to the stiffness in a more sensitive way [91].

In order to characterise the Young's modulus for open cell structures, Timoshenko's standard beam theory can be used. Based on the deflection δ proportional to FL^3/E_sI, and the applied stress σ as $F \propto \sigma l^2$ the displacement δ can be related to the strain ϵ as $\epsilon \propto \delta/l$:

$$E^* = \frac{\sigma}{\epsilon} = \frac{C_1 E_s I}{t^4} \tag{3.1}$$

Taking into account that, for three dimensional geometries, the relative density can be approximated to $\rho^*/\rho_s \propto (t/l)^2$ [13], further substitution leaves the expression as shown in equation 3.2.

$$\frac{E^*}{E_s} = C_1 \left(\frac{\rho^*}{\rho_s}\right)^2 \tag{3.2}$$

where C_1 is reported to be close to 1 after numerical simulations [13].

3.2.2 Bending-dominating plastic resistance

Further deformation beyond the elastic region can be predicted based on beam bending theory, equation 3.3. Assuming that the stresses experienced within the beam, tension and compression in the extreme fibres of a section of thickness t, could at most reach the yield strength σ_{ys} (eq. 3.4), failure therefore would occur when the plastic moment M_p is equal or greater than the bending moment M [96], that is $M \leq M_p$.

$$\frac{M}{I} = \frac{\sigma}{Y} \tag{3.3}$$

$$\frac{M_p}{I} = 2\frac{\sigma_s}{t} \tag{3.4}$$

Considering the second moment of area proportional to t^4 as $I \propto t^4$ for a squared area of section t then, the fully plastic moment would be proportional to the yield strength as,

$$M_p \propto \sigma_s t^3 \tag{3.5}$$

therefore, relating the material yield strength σ_s to the applied stress σ^* to the cellular material $M \propto \sigma^* L^3$, the strength failure would be:

$$\frac{\sigma^*}{\sigma_s} \propto \left(\frac{t}{L}\right)^3 \tag{3.6}$$

A substitution in terms of relative density would be:

$$\frac{\sigma^*}{\sigma_s} = C_2 \left(\frac{\rho^*}{\rho_s}\right)^{\frac{3}{2}} \tag{3.7}$$

where the C_2 value is close to 0.3 [13]. It has to be mentioned that this expression does not work for relative densities higher than 0.3, as the *double counting* of corners leads to considerable deviations from experiments. Further improvements have been made by Ashby & Gibson [91], and reported experimentally with good results by Hernandez-Nava et al. [97] through equation 3.8

$$\frac{\sigma^*}{\sigma_s} = C_2 \left(\frac{\rho^*}{\rho_s}\right)^{\frac{3}{2}} \left(1 + \left(\frac{\rho^*}{\rho_s}\right)^{1/2}\right) \tag{3.8}$$

The constants and exponents shown here are employed frequently in the mechanical properties characterization of cellular materials [11][20]. However, the value of these constants falls in a wide range for different applications and topologies. Similar relationships to equations 3.2 and 3.7 are reported in the literature indicating the extensive range of these values constants can take [13][14][35][91].

3.2.3 Stretching-dominated structures

The stretching-dominated structures on the other hand, involve more compression or tension mechanisms than bending of their elements. These structures are generally characterised by having a high number of elements, and therefore a high connectivity, making them prone to develop states of self-stresses [13]. Similarly to bending-dominated structures, the mechanisms of buckling, yielding and fracture compete to determine the failure upon loading. Therefore, the properties and their relationship with density are reported to be similar to those for bending-dominated structures. In such case, the constant values may vary as a sign of their indicative collapse behaviour. As part of these fundamental differences Calladine & English [98] previously reported that stretching-dominated structures (called Type-2) may behave significantly differently under high strain rates due to inertial effects. This after stating that vibration forces developed from acceleration in their structural elements can lead to increases in stress at high impact velocities.

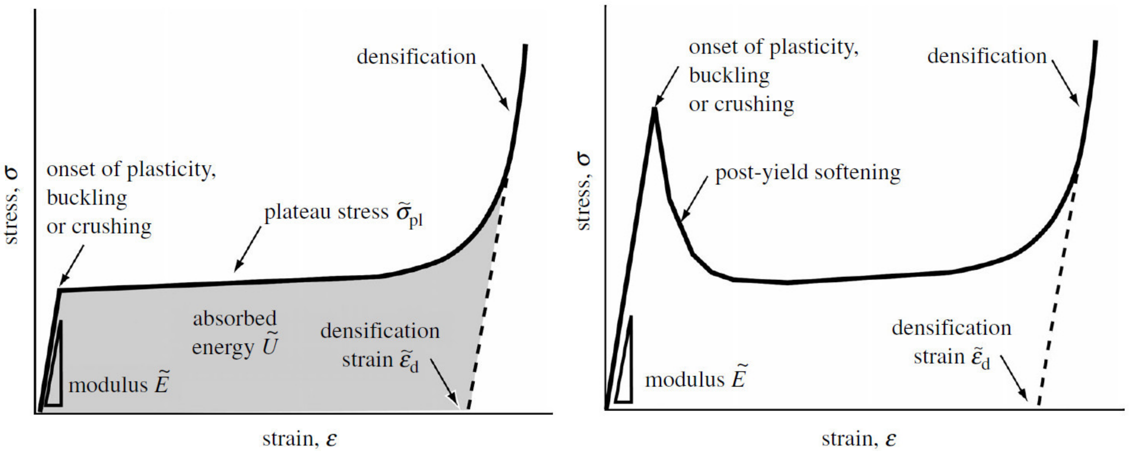

Figure 3.2: Schematic representation of stress-strain curves [13] with key features under compression of: Bending-dominated structures and stretching-dominated structures shown in left and right respectively.

3.3 Energy absorption and blast protection

As mentioned previously, cellular solids are capable of developing excellent properties for energy absorption. The main way to achieve this is through extensive deformation and developing long plateaus in their stress-strain curves. So, if they are subjected to deformation, the energy absorbed would be sufficient before the material reaches densification. Therefore, a combination of long plateau strain and high plateau stress σ_{pl} result in a potential candidate material for protection of rear structures, see figure 3.3a[14]. Hollow tubes, foams and metallic honeycombs have been reported to possess these characteristics for energy absorption and packaging. However, for energy absorption where blast protection is implied, cellular solids perform better if plates are attached to the front in order to deflect shock wave fronts due to the conserved momentum from impulses transmitted to them [99].

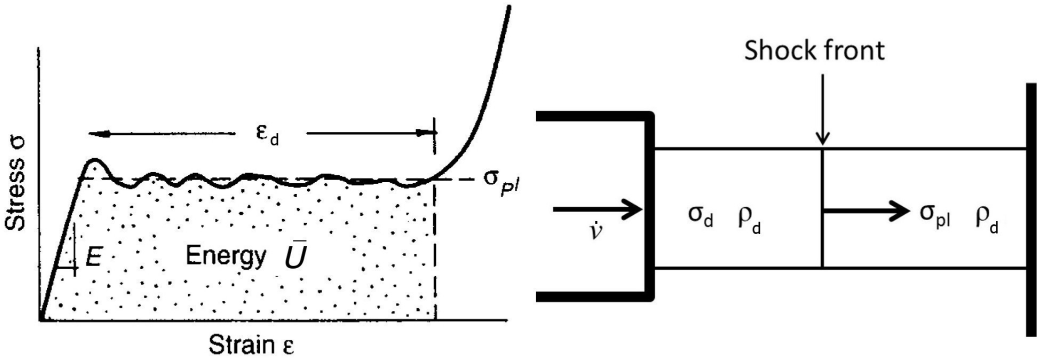

Figure 3.3: Left, stress-strain curve for a material with energy absorption applications including; a stress plateau σ_{pl} prior densification ϵ_d [14]. Right, a schematic representation of a material deformed uniaxially showing the shock wave propagation.

Although there is a high number of cellular materials that can be used in protecting and packaging applications, stochastic configurations made by low cost processes are preferable. As an example, foaming of liquid metal by gas injection or decomposition of particles releasing gas are among the most widely used for aluminium cellular solids [100].

3.3.1 Strain rate sensitivity

As an important characteristic in the mechanical response of cellular solids, the rate of deformation may have a strong influence on the flow stress. It is known that the deformation of cellular solids is partly dependent on the bulk material properties, where its flow stress response to strain rate is dependent to the motion of dislocations [101]. Such motion, thermally assisted, can face short-range barriers on its path at faster strain rates. This is because of less effective thermal activation at high rates of deformation. Consequently, it is common to find that materials with a strong temperature dependency exhibit high strain rate sensitivity [102].

For the case of *Ti-6Al-V*, the deformation at constant temperature and strain during hot working has been reported to be controlled mainly by dislocation glide/climb processes [103]. This after comparing a range of strain rates where this deformation process is suggested to be found in strain rates of the order of $0.1s^{-1}$. However, as the strain rate is reduced, deformation modes of diffusional creep compete increasing the strain rate sensitivity [1]. Such sensitivity evaluated by determining the slope m of experimental ln σ-ln$\dot{\epsilon}$ curves at strain ϵ and constant temperature T (see equation 3.9), to describe the flow stresses in the form of $\sigma = C(\dot{\epsilon})^m$ with C as a constant.

$$m = \frac{d \log \sigma}{d \log \dot{\epsilon}} \tag{3.9}$$

From the structural point of view, the strain rate sensitivity on the cell deformation has been analysed by Deshpande & Fleck [15]. They suggested that the strain rate ($\dot{\epsilon}$) in the outer fibres of the cell walls are an order of magnitude lower than the macroscopic strain rate as, $\dot{\epsilon}' \approx \frac{\dot{\epsilon}}{8}$. This assumes that the kinematics of plastic deformation is by plastic hinges, see figure3.4b [91].

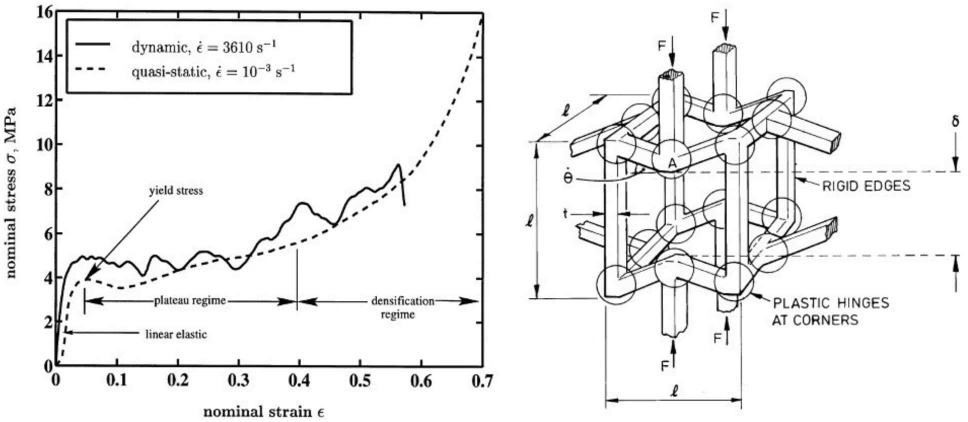

Figure 3.4: Left, stress-strain compression curves at quasistatic and dynamic strain rate $\dot{\epsilon}$. Right, kinematics of plastic deformation where F is the external load, l and t the length and thickness of the uni cell, $\dot{\theta}$ the rotation of the plastic hinge and δ the displacement [15].

3.3.2 Blast wave protection

Another important feature of energy absorption applications is the capability to withstand and mitigate blast wave loading. It has been extensively reported that cellular solids are potential candidates to reduce the loading impact and to protect rear structures [104] coming from blast waves caused by explosions [105] or, from direct high speed impacts [99]. The use of these materials to arrest the blast wave has been suggested as an attempt to absorb the income energy due to a differences in pressure from the shock front. This, as the travelling increase in pressure transmits mechanical impulses along its path, making cellular solids with attached buffer plates (effectively sandwich panels) attractive materials to reflect a portion of the blast waves and mitigate the over pressure. Various studies highlight the beneficial effect of using sandwich panels [105][106] to abate blast waves attributing such capability mainly to features of fluid-structure interaction, kinetic energy dissipation and an increased bending resistance due to the panel configuration [107][108][109][110].

On the other hand, the use of these materials has been suggested as an attempt to spread the loading from direct impacts, i.e. with no reflected shock waves. This is by taking into consideration compressive waves travelling through the solid at a speed of $(E/\rho_s)^{1/2}$ that may leave dense regions in the crushed material reducing the peak impact stresses [14]. However, the potential for this region of material to be crushed depends of both material and structural features. From the material configuration point of view, the dimensions of plate thickness and core, as well as its relative density and geometry, are fundamental in constitutive models [14]. The strength of the parent material, *Ti-6Al-4V* in this case, is also known to be dependent of the strain rate. From the structural point of view, the propagation of shock waves can cause the material properties to become load rate dependent and in some cases to develop inertial effects [98].

Shock wave propagation

The strength of cellular solids under dynamic loading can be approached by shock wave propagation theory. A typical accepted model to estimate the collapse strength of a cellular solid was proposed by Reid and Peng [111] under conditions of uniaxial loading independent of the rate. Its prediction is based on the consideration of a rigid, perfectly-plastic object being compressed from one end towards the opposite fixed end reaching a strain of densification ϵ_d at a stress plateau σ_{pl}, see figure 3.3 a and b, arriving to an increased strength σ_d of:

$$\sigma_d = \sigma_{pl} + \frac{\rho \dot{v}^2}{\epsilon_d} \tag{3.10}$$

Increments in flow stress under compression of *Ti-6Al-4V* foams have been reported [112][113] to be $\approx 30\%$. Taking into account a relative density ranges of 0.16 to 0.33 additively manufactured recently [97], critical speeds where these effects become important would be close to $\approx 50 m/s$. Further investigation of deformation at high impact speeds on cellular solids reported by Ozdemir et al. [104] showed significant enhancement in peak strength at speeds of $\approx 180 m/s$ and densities of 0.6 to 0.7 presented in lattices manufactured by EBM using *Ti-6Al-4V*.

3.4 Mechanical properties of EBM cellular solids

Several studies have reported the mechanical properties of foams and lattices processed by EBM [19][22][70][114][115]. It is worth mentioning that most of the literature reported on this topic is dedicated to the details of the processing and characterisation with few studies [16][17][19] on detailed mathematical models explaining their structural behaviour. Part of this lack of information may be related to the relatively new manufacturing process and the up-to-date technological resources that are not capable to fully model performance of AM materials. Computational power as an example, may be limited against the high number of irregularities that can be found in AM components such as internal pores, surface roughness, bulk anisotropy, etc.

3.4.1 Bulk Properties

With significant differences in microstructure and properties, thin walled materials, usually develop their properties due to size component implicating the thermal constraints of solidification and cooling rate. Murr et al.[116] for example, had compared microhardness variations in solid monoliths and metal foams in as-built EBM condition, giving values of 3.6 and 4.5GPa respectively. Hence suggesting that the Ti-6Al-4V transformed microstructure i.e. α laths, underwent through a higher cooling rate due to size of the component giving higher indentation resistances in the later materials. This after the fine α lath thickness, product of rapid cooling rates, can be related to higher material strength through Hall-Petch type relationships.

3.4.2 Meso-sructure

The mechanical properties of lattice materials also depend on the likehood of macro-defects as possible factors to trigger premature failure. In this context, internal pores, surface roughness and undersized sections can diminish the structural performances. Parthasarathy et al. [92] have reported the effective stiffness, compressive strength, dimensions and weight of cubic geometries. These porous structures, intended to populate regions of mandible and hip implants reported, overall, dimensional mismatch according CAD designs. Such mismatch accentuated when strut size decrease, i.e increasing the cellular porosity with changes in properties. As part of their study, recommendations on safety factors were suggested for porosities of 70% and higher in order to achieve a desired volume fraction. In a similar study [117], it was reported that cubic lattices with different porosities (45-70% and strut sizes from $450 - 800\mu$m), the mechanical properties not only depend on cellular porosity but also on the dimensions of solid struts. However, the melting strategy was not explicitly mentioned in any of these studies, such as beam power in relation to the size of the component, therefore a potential area for optimisation of melting small trusses is left for further research.

In regard to internal defects such as pores, Gorny et al. [118] have reported that these type of defects (characterised by digital imaging correlation) act as local strain concentrators, therefore collapsing the structure prematurely upon loading. Hazlehurst et al. [119] have also shown (through finite element methods) that mechanical properties of cubic lattices processed by SLM, significantly decrease compressive stiffness due to structural variations and heterogeneities associated to the manufacturing process. In regard to EBM, Cormier et al. [120] have reported lower compressive strength and energy absorption values than expected for auxetic materials. This was attributed (among other features) to the “stepping” effect that AM technologies intrinsically develop.

It is therefore likely that defects, developed intrinsically, create directionality on the properties depending on loading conditions and the position of such local stress concentrators. Compressive resistance for example, has reported to give dissimilar strength when loaded parallel or perpendicular to the build direction [121]. Also, Harrysson et al. [114]

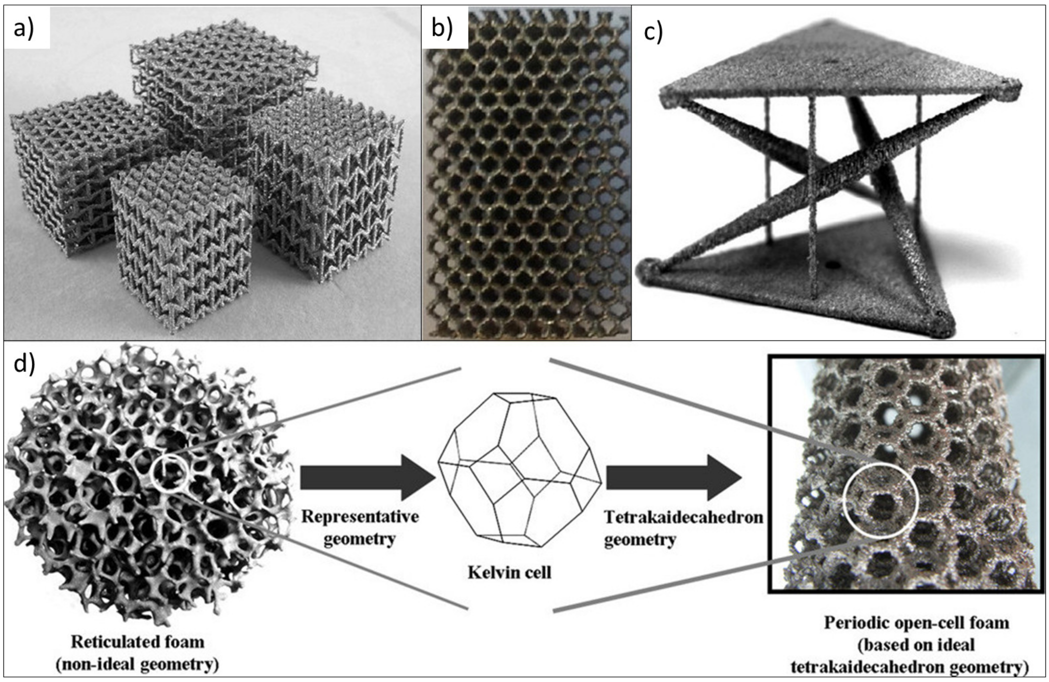

Figure 3.5: Examples of lattices fabricated as proof of the concept for EBM manufacturing. (a)Cellular solids with auxetic behaviour [16], (b) Diamond-like lattices for biomedical applications [17], (c) Tensegrity structures [18] and (d) foams with ideal tetrakaidecahedra packing [19].

pointed out that orientation of lattice structures during the process is of critical importance. Beam elements should be orientated within variations at a certain range to get the best possible strut shape out of the process. As a result, all these defects; internal porosity, dimension mismatch, etc., contrast to ideal smooth surfaces usually employed in finite element modelling that can mislead the mathematical predictions [122].

Despite the defects that can be found in AM micro-truss structures, it is the cellular geometry what establishes the main criteria for its resistance upon loading. In figure 3.6 it is plotted an example of different topologies showing properties of compressive strength and compressive stiffness. Lattices made by SLM are also shown for comparison. Despite the multiple authors and data plotted in figure 3.6, and the different methods that may been employed in the report of properties, e.g. Young's modulus in initial slope or unloading slope, yield strength or plateau stress, figure 3.6 provides insight into the possible range of properties that specific geometries can offer.

Cubic-like lattices for example seems to be on top of properties for any given relative density. This has been reported to be due to a better withstanding the axial compressive forces with trusses parallel to loading direction, especially at low levels of density. Stochastic structures like foams on the other hand, show a lower compressive resistance within similar levels of density. This has been reported to be due to the failure mechanisms found in foams, where the collapse upon loading appears in trusses of thinner cross section leaving the rest acting redundantly to the active density that supports the loading.

3.4.3 Structural performance

Despite the limiting factors above mentioned, analytical and numerical models have been adapted so that predicting properties. As an example, Inayat et al. [19] have determined

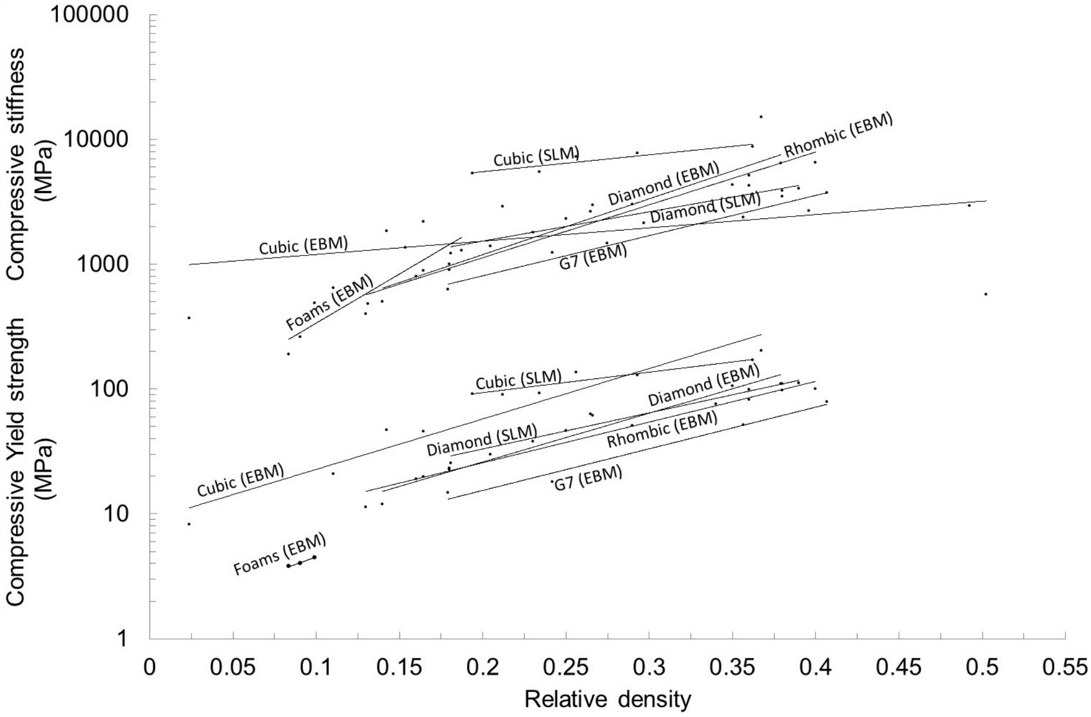

Figure 3.6: Compressive strength and stiffness of EBM an SLM Ti-6Al-4V lattices and foams[11][12][17][20][21][22][23][24].

experimentally the pressure drop on periodic foam samples manufactured by EBM. The current equations were modified developing new correlations that agree experimental evidence and theoretical models. Amahdi et al. [17] have derived analytical relationships for a diamond-like lattice structure. In their study, experimental mechanical properties under compression were also reported. Along with new analytical solutions, the prediction of elastic modulus, Poisson's ratio, critical buckling load and plateau stress were carried out with good agreement. Such mathematical formulation for the Young's modulus was carried out based on Euler-Bernoulli theory (equation 3.12) and Timoshenko's theory, equation 3.15. The Euler-Bernoulli approach (or beam element theory) is based on the deflection ω of a beam element when a load is applied. Assuming constant bulk properties and a constant cross section of the beam, the rate of change of beam deflection is given as:

$$\frac{d^4\omega}{dx^4} = 0 \tag{3.11}$$

By applying boundary conditions of a beam fixed at one extreme and free rotation at the other, and replacing the force term by $Fcos\gamma$ for the component in the Y direction, the displacement of the truss element by bending and axial forces (denoted by subscripts) is $\delta = \delta_{22,b} + \delta_{22,a} = \frac{Fl^3cos^2\gamma}{12E_sI} + \frac{Flsin^2\gamma}{E_sA}$ where; I and A are the second moment of area and the area of the cross section. Hence, the displacement of the unit cell $\sigma_{uc} = E_{uc}\epsilon_{uc}$ where $\epsilon_{uc} = \frac{\delta_{uc}}{L_0}$ is the ratio of the Young's modulus of the lattice and the Young's modulus of the material as:

$$\frac{E^*}{E_{uc}} = \frac{\sqrt{6}\rho_r}{\pi 3 + 2\sqrt{3}\rho_r} \tag{3.12}$$

Taking into account that the relative density is given by $\rho_r = \frac{3\sqrt{3}\pi d^2}{16l^2}$, this value was taken from experimental measurements. Ahmadi et al. [17] also reported an expression neglecting axial forces, equation 3.12. This is justified for the case of diamond lattices with low relative density, giving the equation as:

$$\frac{E^*}{E_{uc}} = \frac{\sqrt{6}}{3\pi}\rho_r^2 \tag{3.13}$$

On the other hand, the second derivation of the Young's modulus approached with Timoshenko beam theory was based on the differential equation for static beam loading [17] as:

$$\frac{dw}{dx} = q(x) - \frac{1}{\kappa AG}\frac{d}{dx}\left(EI\frac{d\phi}{dx}\right) \tag{3.14}$$

where the displacement of the cantilever at its end point was $\delta = \frac{Pl^3}{3EI} + \frac{Pl}{\kappa AG}$ defining κ as the shear coefficient and for a circular cross section given by $6(1+\nu)/(7+6\nu)$. Therefore, obtaining a total deformation of the unit cell of $\delta = \frac{Pl^3cos^2\gamma}{12E_sI} + \frac{Plsin^2\gamma}{E_sA} + \frac{PLcos^2\theta}{\kappa AG}$ and giving a similar displacement as in Euler-Bernoulli with an extra term. This gives a lattice-material elastic modulus ratio in terms of the relative density as:

$$\frac{E_{p-Timoshenko}}{E_s} = \frac{(0.46) + (0.17\rho_r)\rho_r^2}{(0.46) + (1.17\rho_r)(3.85 + 1.41\rho_r)} \tag{3.15}$$

For the plastic plateau-yield stress ratio (see equation 3.16), Amadi et al. [17] developed a model based on the bending moment of a truss element, $\sigma = \sigma_b = \frac{Md}{4I} = \frac{Pldcos\gamma}{8I}$. As before this neglects stresses developed by axial forces, and therefore, the formula is given by:

$$\frac{\sigma_{pl}}{\sigma_s} = \frac{9\pi d^2}{32\sqrt{6}l^3} \approx 0.35\rho^{1.5} \tag{3.16}$$

3.5 Summary

The reported literature in this chapter aims to draw the baseline for analysing the response of cellular solids upon elastic and plastic deformation. Based on simplistic approaches properties of strength and Young's modulus can be initially predicted for different porous materials. Other models using beam element theory, at a deeper level, have also been reported for diamond-like geometries where failure modes match the prediction of properties after the experimental testing. Despite the multiple heterogeneities that can be found in AM cellular solids, geometrical arrangements seem to establish clear differences between different porous materials, making possible a systematic study in function of volume fraction and therefore tailoring their properties. Other considerations such as strain rate sensitivity or inertial effects, that may be present in the studied structures, has not been extensively reported as in quasi-static conditions of loading, this contrasts to the idea of multiple uses that light porous structures can be used in blast wave applications for example.

4

Experimental procedure

The methodologies used to carry out the experimental work followed a flow of material synthesis, mechanical testing and micro/macro-scale characterisation. The *Ti-6Al-4V* alloy system has been used for the EBM manufacturing, fabricating cellular materials and specimens for parent tensile properties. The cellular materials were structurally characterised through X-ray Computed Tomography (CT) prior to deformation. The mechanical testing was carried out under two main regimes, under quasistatic and under dynamic conditions. In order to investigate the bulk material properties and its influence on those porous materials, high vacuum heat treatments were applied to the specimens. Finally, the material characterization was carried out by carefully preparing the specimens for microscopy, Vickers micro hardness and X-ray diffraction.

4.1 EBM manufacturing

EBM manufacturing, as any other AM route, starts with a surface representation design. Further slicing operations take place in layers according the beam power parameters aiming for manufacturing reliability. Upon a favourable processing step, the materials are air blasted in the powder recovery system for cleaning and recycling material purposes prior further characterisation.

4.1.1 Build design and parameters set-up

The surface representation for regular lattice structures was carried out by designing the structure with *Netfabb*® professional. The node connectivity, structural element profile (cross-sectional area of the trusses), and unit cell size were manipulated for the lattice construction. After fixing faulty triangle tessellations, e.g. “holes” and “intersecting triangles” the models were converted to sliced format for their further processing.

Figure 4.1: Schematic EBM sequence including: (a) The surface representation, (b) the slicing of files and (c) the file uploading.

The output file was represented by a series of slices at the thickness the system would melt with the previous power beam parameters. Finally, the files were uploaded to the EBM control, the interface between the ARCAM system and the user. Conditions and parameters of *vacuum* levels, *voltage* and *beam speed* and *current* were set up according the themes developed by ARCAM shown in table 4.1 prior manufacturing.

Table 4.1: Standard 70μm ARCAM Melt, Net, wafer, preheat I and preheat II themes including beam parameters of current, speed, speed function (SF), focus offset (FO), line offset, line order and offset to contout (OC). All values applied at a constant vacuum process of $2 \times 10^{-3} mbar$.

Theme	Current (mA)	Speed (mm/s)	SF	FO (mA)	Line offset (mm)	Line order (mm)	OC (mm)
Net	1.7-3	200	1	0	0.2	1	0.050
Melt	17	500	36	19	0.2	1	0
Wafer	7	1500	–	0	5	–	–
Preheat I	30	14600	–	50	1.2	15	–
Preheat II	38	14600	–	50	1.2	15	–

4.1.2 ARCAM S12 system

Currently, ARCAM's manufacturers sell various EBM systems with advances in new models coming from improving previous features or looking for adapting equipment to new clientele needs. At the moment, the cycle of setup, running and unloading of samples of post production is time consuming and requires experience and confidence. Because of the large number of set-up variables, the build success relies to a large extent on the operator's skill and experience.

The usual maintenance includes the cleaning sensitive parts such as the anode, grid cup, conductive pins, column foil and replacement of filament after 80 hours of use. While this setup needs all surfaces clean, the rake system on the other hand needs to be recalibrated to avoid powder leakage from the build envelope. Powder sensors, rake blades, full powder hoppers, a start plate centred and free of any particle in its surface are among the principal tasks. Finally, the chamber vacuum seal needs to be free of any particles to ensure a quick vacuum step.

Upon build completion, all particles are recovered and sieved after being air blasted in the PRS. The powder is stored immediately after the sieving as moisture can be introduced into the batch. As mentioned before, all these operations (powder handling) have been improved incrementally over a period of time by the EBM manufacturers. Currently there are systems being introduced to market where the human interaction with powder is reduced to the minimum as this represents a direct effect on the input material quality.

4.1.3 Raw materials control

Due to extensive powder re-usage, a in-house developed checking routine constantly reported data on chemistry, flowability and particle size distribution of the current batch of powders. This is part of the quality control required for powder recycling. Powder samples were regularly sent to "AMG superalloys UK Limited" for chemical analysis. Chemistry inspection was achieved by gas chromatography reporting the content of interstitial elements of carbon, oxygen and nitrogen. Once manufactured, solid samples were also sent in order to corroborate chemistry. Such analysis was carried out using combustion analysis (Leco). The powder flowability was measured according to the standard ASTM B964-09 and powder size distribution according to the standard ASTM B8822-10.

4.2 X-ray Computer Tomography (XCT)

As part of the EBM manufacturing evaluation, non-destructive characterization using X-ray Computed Tomography (XCT) was employed, figure 4.2. All XCT scans were carried out at the Henry Mosley X-ray Imaging Facility at the university of Manchester.

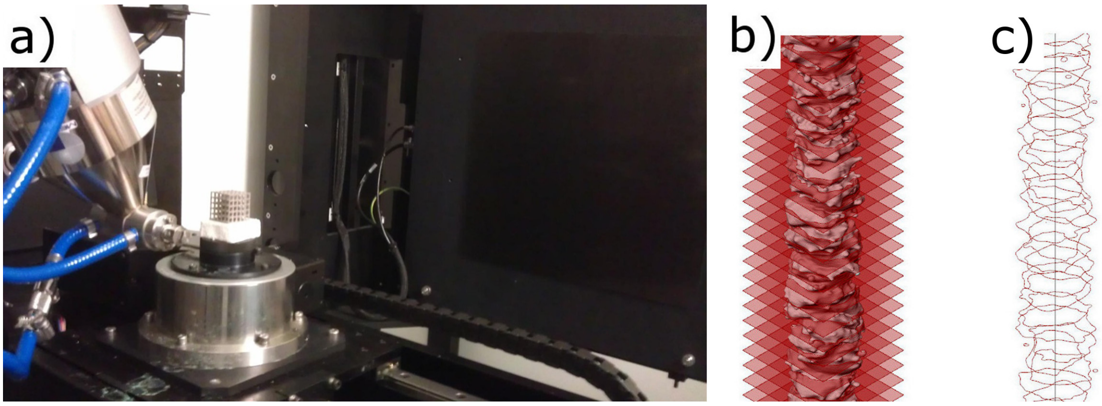

Figure 4.2: (a) The X-ray tomography equipment showing the x-ray source, the sample to be scanned and the panel detector. Schematic illustration of the XCT analysis of an imaged strut in (b) and (c).

4.2.1 Data acquisition

A Nikon Metrology 225/320kV Custom Bay system was employed with an accelerating voltage of 160kV and a 110μA current to produce a white beam of X-rays radiating from a spot of 5μm from a tungsten target. The source-sample-detector positions were such that 10× magnified images were collected on a Perkin Elmer 2048 × 2048 pixel 16-bit amorphous silicon flat panel detector having a pixel size of 200μm giving an effective pixel size of 20μm. The sample was rotated through 360 degrees and a total of 3142 radiographs taken using the Nikon-Metrology Inspect-X acquisition software.

4.2.2 Visualization

The 2D radiographs were computationally reconstructed into a 3D volume, using Nikon-Metrology's CT-pro software based on a filtered back-projection algorithm. The volume was reduced from 16-bit to 8-bit using VGStudio MAX in order to allow the data to be processed and visualised. The collected data was loaded into Avizo 7.1 and then cropped to manipulate the scanned data. Threshold values were chosen to segment the images giving different solid/air ratios at convenience. The 3D structures were exported to ScanIP software to produce volume and surface files for further use. The scanned surfaces were analysed once again in parametric studies constructed in Rhinoceros® 5 and Grasshopper^{TM}. The data was obtained after importing and aligning the STL files of all representative surfaces for each strut diameter. The mean area, second moment of area and radius (distant vertex length defined and quantified from virtual cross-sections taken every 70μm along the 10 mm length of the rods. The radius was extracted at aligned points along the axial direction of the strut, figure 4.2b and c, allowing a longitudinal profile to be obtained such that the roughness along the strut length.

4.3 Quasi static tests

Mechanical tests under quasistatic conditions were performed in order to characterise the strength of the material, these included compression and three point bending, see figure 4.3. While the compression test was the direct method to characterise the cellular materials, additional tensile tests were utilised as complementary methods. It is worth to mention that compression and three point bending tests were carried out in the university labs, while the tensile tests were performed in specialised testing laboratories.

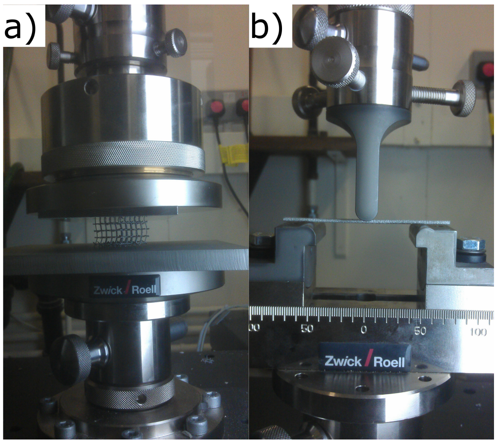

Figure 4.3: Zwick/Roell Z050 test rig machines tests of (a) compression and (b) three-point bending.

4.3.1 Tensile testing

The parent material properties were obtained through tensile tests, such characterisation was carried out in Special testing LTD Sheffield UK. The methodology included the manufacturing of boxes of 16 × 16 × 65 to be further machined threaded-ends out and finished surfaces off (see figure 4.4) according the rounded specimen specifications for the ASTM E813a standard testing method. Properties of 0.2% Yield Strength, Ultimate Tensile Strength, Young's Modulus and percentage elongation were reported.

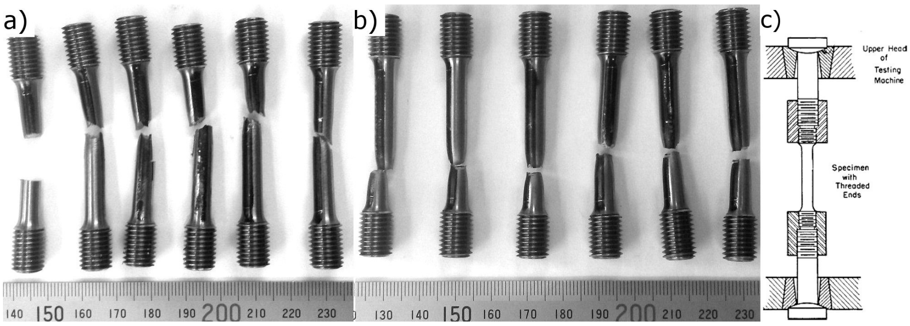

Figure 4.4: Horizontal and vertical tensile specimens, (a) and (b) respectively, after tensile tests showing fracture due to "necking" effects typically found in ductile metals. (c) Schematic drawing of the gripping system prior tensile testing.

4.3.2 Compression testing

Compression testing was carried out using two servo hydraulic machines. The first equipment employed was a Hounsfield universal test rig TX0039. All tests were performed at room temperature and at an initial strain rate of $10^{-4}s^{-1}$. The second equipment was a Zwick/Roell Z050 test rig machine equipped with video extensometer. All tests, similar to those performed in the previous testing machine, were performed at an initial strain rate of the order of $10^{-4}s^{-1}$ at room temperature. Stress-strain histories could be obtained from the load displacement curves after correcting for the test rig compliance, which was done using compressive cycles up to the highest tested load with no sample present between the compression platens. Such curves were used to determine, for all cases, the Young's modulus from the gradient of the linear elastic portion of the curve, the 0.1% offset yield strength and the maximum compressive resistance.

The contact surfaces of all compression tests consisted in polished *Ti-6Al-4V* plates, carefully placed between the lattice samples and the compression platens of the machine. This as a recommendation to reduce frictional forces that can render the strength data unreliable.

4.3.3 Three point bending

The Zwick/Roell Z050 machine was also employed for three point bending test. Test were performed at a constant strain rate ($2.2\times\ 10^{-3} \pm 3.5 \times 10^{-4}s^{-1}$) according the standard ASTM C1684-13, and span-to-depth ratio of 36. Flexural 0.1% Yield strength was extracted once the stress-strain data was obtained. The equations to flexural stress and strain were $\sigma_{flex} = \frac{8FL_s}{\pi d^3}$ and $\epsilon_{flex} = \frac{6d_{th}\delta}{L_s^2}$where F represent the load, L_s the span length, d the rod diameter sample, δ is the maximum deflection of the centre of the beam and d_{th} is the depth of the tested beam.

4.4 Dynamic tests

Hopkinson Bar (HB) tests were performed at Blastech LTD in collaboration to the department of Civil and Structurally Engineering in order to evaluate the deformation mode at high strain rates, figure 4.5a. Co-axially aligned with the gas gun that provided the high speed impulse, figure 4.5b and the HB was mounted in ball bearing units to minimize friction. A 25 mm diameter and 250 mm long EN24T steel bar was used as the impactor. With a mass of 963 g fired at velocities in the range of ≈25 m/s, the specific impulse and kinetic energy density delivered to the target specimen was ≈40000 kPa·msec and 400 kJ/m^2 respectively. The compressive stress pulses from the applied transient load were effectively recorded by an axially aligned strain gauge station.

All tests were recorded by a Phantom v 4.2 high speed digital video camera, figure 4.5c, operating typically at 40-50 µs per frame. The high speed video footage was later used to establish the velocity of the impactor during the impact event and the displacement vs time record of the compressed specimens.

The tests were first carried out in the absence of material at the impact face of the HB to establish the baseline for the impactor's signal. Impact tests were later repeated compressing the intended samples in order to assess the loading response.

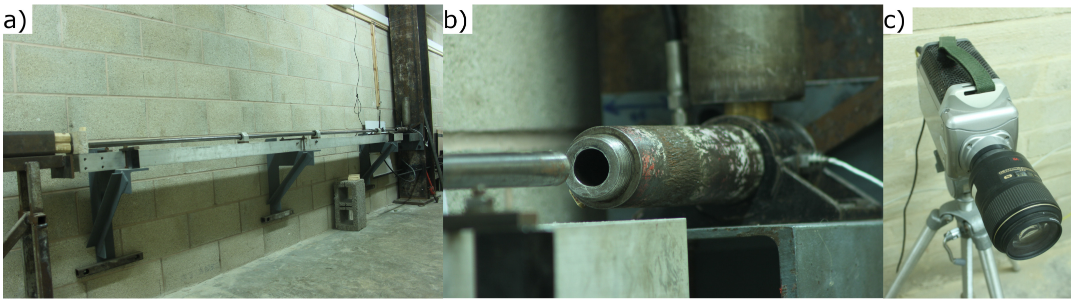

Figure 4.5: Hopkinson bar set-up and image recording. (a) the Hopkinson bar, (b) the striker canon, (c) the high speed video camera.

$$\epsilon_t = \frac{4V_{out}}{2S_gGV_{in}} \tag{4.1}$$

where ϵ_t is the strain transmitted, V_{in} the input voltage, V_{out} the output voltage, S_G the gauge factor and G is the gain. The HB was equipped with a gauge in one position along the bar sufficiently far from the impact face to avoid end effects.

4.5 Heat treatments

Two thermal histories were explored besides the "as-built" condition; heat treatments above the β–transus temperature and high in the $\alpha + \beta$ region. The temperature profiles of the heat treatments, carried out under high vacuum, were a heating rate of 10°C/min to 960°C or 1200°C for 2 hours followed by furnace cooling (FC).

The first heat treatment (960°C/2h/FC) was an attempt to retain the columnar β grain microstructure. It is reported that during heat treatments in the $\alpha+\beta$ region the α phase can be altered without a significant effect on prior β grains [37]. The second heat treatment (1200°C/2h/FC), which is usually not applied for bulk Ti-6Al-4V, was intended to break down the typical columnar β grain shape that is found in EBM components [26]. Such microstructure forms because of the build directional and the preferred growth direction.

4.6 Sample micropreparation

The metallographic sample preparation started with cutting the material using a Struers Minitom precision machine with a diamond abrasive disc and a solution of 90% water and 10% of low foam triethanolamine additive as a cooling media. Then, all samples were hot mounted in a conductive Bakelite resin using a Buehler Simplimet 1000 automatic press with a programed cycle of 290bar in pressure, 2 minutes heating and 4 minutes cooling time. Grinding was carried out in a Tegramin-20 Struers preparation system using water and a 9 μm grain size Diamet suspension. The samples were polished immediately after using 20 vol% colloidal silica (6 μm) in 80 vol% water. Finally, the samples were etched in Kroll's reagent for 10 seconds.

4.7 Optical Microscopy

Most of the microscopical observations were carried out in a Nikon eclipse LV150 microscope using polarized light (PL). As most of the titanium alloys respond favourably to

PL, only in few occasions the use of microetching was employed.

4.7.1 alpha lath thickness measurements

The α lath thickness was measured using OM images with 1000x in magnification and a set of overlaid ovals, see image 4.6. The manual technique consisted of drawing ovals on the micrograph of known line length and counting the number of intersections to allow the values to be calculated according to the linear intercept average.

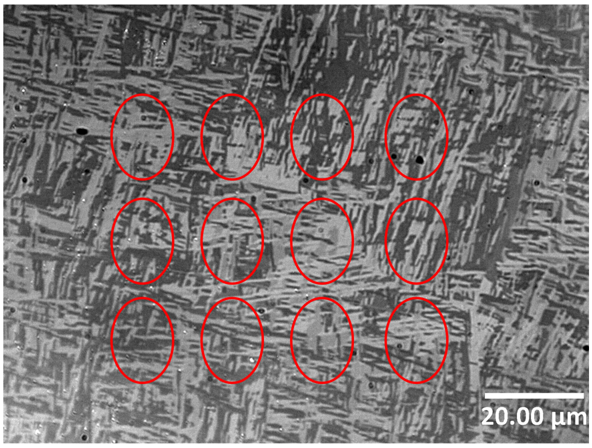

Figure 4.6: Measurement of α lath thickness by intersecting closed lines.

4.7.2 Alpha colony size measurements

Besides the α lath thickness, microstructural analysis was done through alpha colony size. Using the line intersection method (see figure 4.7), assumptions about shape and morphology need to be made prior to their measurements [25]. The method therefore reports a *colony scale factor*. Etching techniques were applied in order to gain contrast for better imaging.

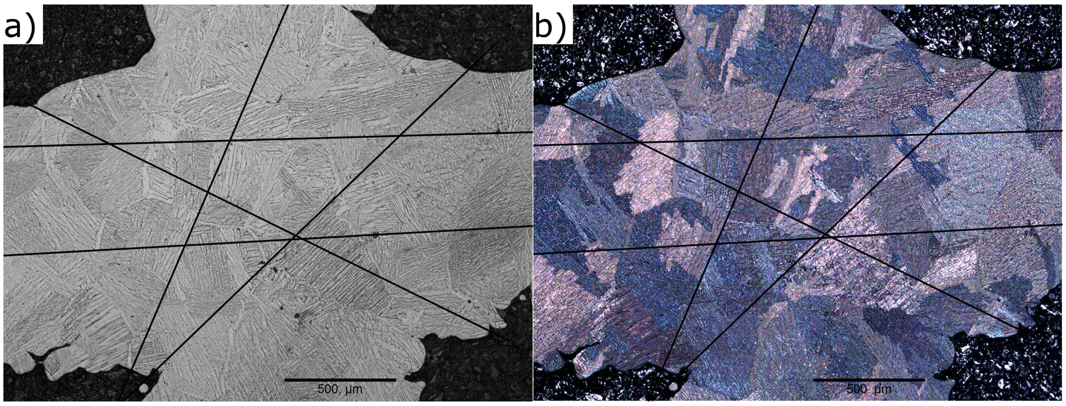

Figure 4.7: Colony size determination through a random array of lines on OM images [25].

4.8 Scanning Electron Microscopy (SEM)

Scanning electron microscopy FEI Inspect F was used for high resolution imaging. The images were obtained typically with backscattered electrons but also with secondary electrons. The observations were carried out using an accelerating voltage of 15kV, $3mu$m of spot size and 10mm of working distance.

4.9 X-ray Diffraction (XRD)

The validation of the present phases in the Ti-6Al-4V system was through X-ray diffraction patterns (XRD). Peak phases were determined using Bragg's law after obtaining the patterns in a SIEMENS 3000 diffractometer with Cu as the source to emit the k(alpha) radiation. Key peak identification was in the 2θ range of 30 to 60.

4.10 Microhardness Vickers (VH)

A Struers Durascan 70 automated system was used to analyse the strength at micro scale through Vickers microhardness (HV). Standardized ASTM speed approach, 0.1 kg in load and 10 s dwell time were the main equipment parameters, figure 4.8a. The resistance to penetration was interpreted by the force-area ratio F/A from the average length of the indentation diagonals. Because of the pyramidal shape, the area A can be determined by:

$$A = \frac{d_l^2}{2sin\left(\frac{136}{2}\right)} \tag{4.2}$$

where d_l is the average length of the diagonal left by the indenter. Therefore the hardness ratio (hardness number) is given by:

$$HV = \frac{F}{A} \approx \frac{1.8544F}{d_l^2} \tag{4.3}$$

where F is in kgf. Upon a series of micro indentations, (100μm spaced between each other shown in figure 4.8b), contour maps were plotted in order to report hardness variation with location in the specimen (see figure 4.8c).

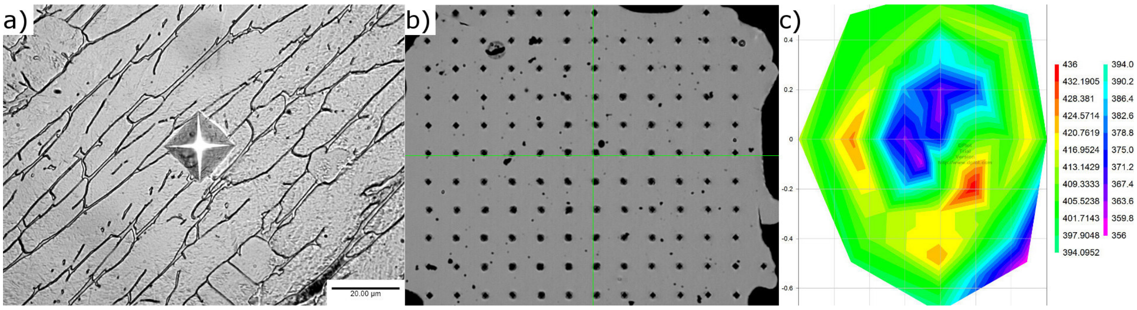

Figure 4.8: Vickers microhardness measurements, (a) grid of indentations with 100μm separation. (b) Contour plots showing microhardness distribution.

5

EBM deposition and material characterization

The present chapter is devoted to the analysis of the beam absorption by the material, the resulting microstructure and bulk mechanical properties. The beam absorption was analysed in terms of the melt pool depth created by the beam current and speed found in standard ARCAM themes. Through Rosenthal's model for point heat sources, theoretical values were obtained which were further compared with experimental results from depositions of single-pass lines onto solid plates of the same material. Subsequently, the same beam parameters were applied repeatedly in layers of 70μm thickness to create solid monoliths from which tensile specimens could be machined. Because of the solidification conditions within the melt pool, a columnar microstructure was found in previous work, associated with the development of high solidification gradients and cooling rates [4]. Observations here using optical microscopy are in agreement with these previous studies. Although a similar microstructure was found throughout all the specimens from tensile testing, a slight variation in properties was found for different build orientations. This difference suggests an intrinsic influence of thermal history through *scan length* values affecting the heat input and modifying the final properties.

5.1 Electron beam penetration

Several responses are possible when a conductive material is subjected to the bombardment of electrons. Some of the incident electrons may be reflected and some others will penetrate into the material, resulting in the loss of their kinetic energy. The interactions and resulting effects can be used in many areas of material science, including in characterisation, machining, welding, etc. For the EBM process the level of electron penetration is related to the power used to create the melt pool, varying in size and shape and influencing the solidification conditions, e.g. thermal gradient, cooling rate.

5.1.1 Rosenthal's approach

The electron beam parameters affecting the melt pool depth and shape have been studied previously by Rosenthal [123] assuming a point heat source. Such a heat source model (see equation 2.1), represents a simplified form of the heat flow equation based on the principle of a quasi-stationary thermal state [76], requiring certain assumptions to be made such that they can be applied. First, the heating effect of the electron beam is described by an infinite single point heat source, therefore, the depth of penetration can be predicted once the surrounding temperature distribution is solved. Second, the heat point source remains constant on its moving path the x direction, travelling with the beam speed. Third, there is no heat loss and finally, the thermal properties of the material remain constant.

Despite these assumptions, the approximations developed by the model need to be further adjusted with the fitting parameter η to account for possible energy loss. It is known that electron beams are diffuse, presenting a Gaussian distribution of energy where losses are unavoidable [77]; the situation is further complicated by the ability to be defocused through *focus offset* values during the process.

To overcome mismatch in predictions, Bontha et al. [74], proposed a fitting parameter η value of 0.35 for *Ti6Al-4V* using a selective laser melting (SLM) system; however, for EBM a different parameter would be needed. It is known that electron beams are more efficient and a large fraction of the incoming energy is converted to heat. While in an EBM system most of the voltage difference applied to the filament is converted, laser systems convert only around the 20% of the electrical energy into beam energy [38]. Studies on electron beams on the other hand have reported higher values of η of 0.55 for welding systems and 0.6 for ARCAM systems [77] after comparing numerically predicted depth values with experimental results.

5.1.2 Experimental beam depth correlation

In order to observe the area affected by the electron beam absorption, a series of single melting lines was made for further observations. The weldtracks were performed on previously deposited material in the form of *Ti-6Al-4V* plates in the "as-built" condition. Values of beam power, speed and focus offset, given in table 5.1, were chosen to be applied, corresponding to the beam conditions found in the hatching and contouring of current themes as given in table 4.1. The ARCAM equipment was used in a manual mode in order to obtain the desired single pass welds with no preheat. This allowed the material properties at room temperature to be used for the numerical model.

Table 5.1: Beam current, speed and focus offset of the weldtracks under study.

Weldtrack	Current (mA)	Speed (mm/sec)	FO (mA)	Speed function	Used for: (melting stage and theme)
a	1.7	200	0	1 and 6	Hatching/contouring, 70μm Net
b	5	280	0	6	Contouring, 70μm Melt
c	2.4	470	0	1	Contouring, 50μm Net
d	1.7	500	0	1	Hatching, 50μm Net
e	15	4530	3	98	Hatching, 50μm Melt
f	15	4530	0	–	Focused beam comparison
g	4	340	3	6	Contouring, 50μm Melt
h	4	340	0	–	Focused beam comparison
i	10	800	3	30	Contouring, 50μm Melt
j	10	800	0	–	Focused beam comparison
k	17	500	19	36	Hatching, 70μm Melt
l	17	500	0	–	Focused beam comparison

Melt pool size and shape. The melt pool depths can be seen in figure 5.1 where the affected zone is measured from the top of the sample to the bottom of the highlighted dashed blue lines. In order to compare the melt pools, paired figures with changes in beam current and focus offset are compared respectively, see figures 5.1(a to l). From figures 5.1(a to d) it can be seen that differences in depth arise for those made with higher beam current at a similar relative speed. This is due to more energy input at a similar relative speed hence increasing the melt pool size. On the other hand, figures 5.1(e to f), (g to h), (i to j) and (k to l) are examples of what seem to be a transition from deep to shallow morphology as the beam is defocused at constant speed and current. It is well known that manipulation of physical conditions in electron processes affects the ideal semicircular melt pool shapes from point heat sources, therefore Gaussian energy distributions even approaching to zero are likely to create shallow melt pools [124].

It can also be observed that size cavities are created for all the weldtracks. This has been reported widely as a intrinsic feature of the changing energy density. Low densities (see figure 5.1(e and f)) are less likely to create vapour cavities where the heat is transferred to the surface of the work piece, creating depth-to-width ratios less than 1:10 [125] contrary to the ideal value of 1:2 predicted by the Rosenthal model. The values of all the obtained ratios can be found in table 5.2 along with the experimental depths and numerical predictions from the model.

Table 5.2: Experimental measurements of melt pool and numerical depth values using $\eta = 0.8$, 7W/mK of thermal conductivity, $T_m = 1660$, 580 J/kgk of heat capacity [37].

Weldtrack (1-10)	Experimental depth-to-width ratio	Experimental depth (μm)	Numerical depth, $\eta = 0.8$ (μm)
a	0.55	176.3	148.7
b	0.62	275.1	218
c	0.33	135.2	116.5
d	0.35	84.1	94.9
e	0.11	63.5	94.2
f	0.10	61.2	94.2
g	0.43	227.7	176.9
h	0.38	213.8	176.9
i	0.41	211.5	183.0
j	0.38	198.2	183.0
k	0.40	302.8	301.9
l	0.50	381.5	301.9

Fitting parameter η**.** In order to compare the predicted depths from the Rosenthal equation, several values of the fitting parameter η were used. The results are shown in table 5.2 and figure 5.2. It is difficult to determine which value of efficiency is the best to predict the melt pool depth for all the weldtracks. This can be explained as the shape of the weldtrack behaves in a way that it is not accurately represented by the heat point source model despite the assumed boundary conditions. It can also be seen that ideal values of 1:2 depth-to-width found experimentally (see weldtrack "l") are well above the spectrum for the efficiency η values plotted in figure 5.2.

Recent investigations have found a good correlation between predicted and experimental results using high values of efficiency ≈ 0.90 [126]. Wang et al. reported this match in

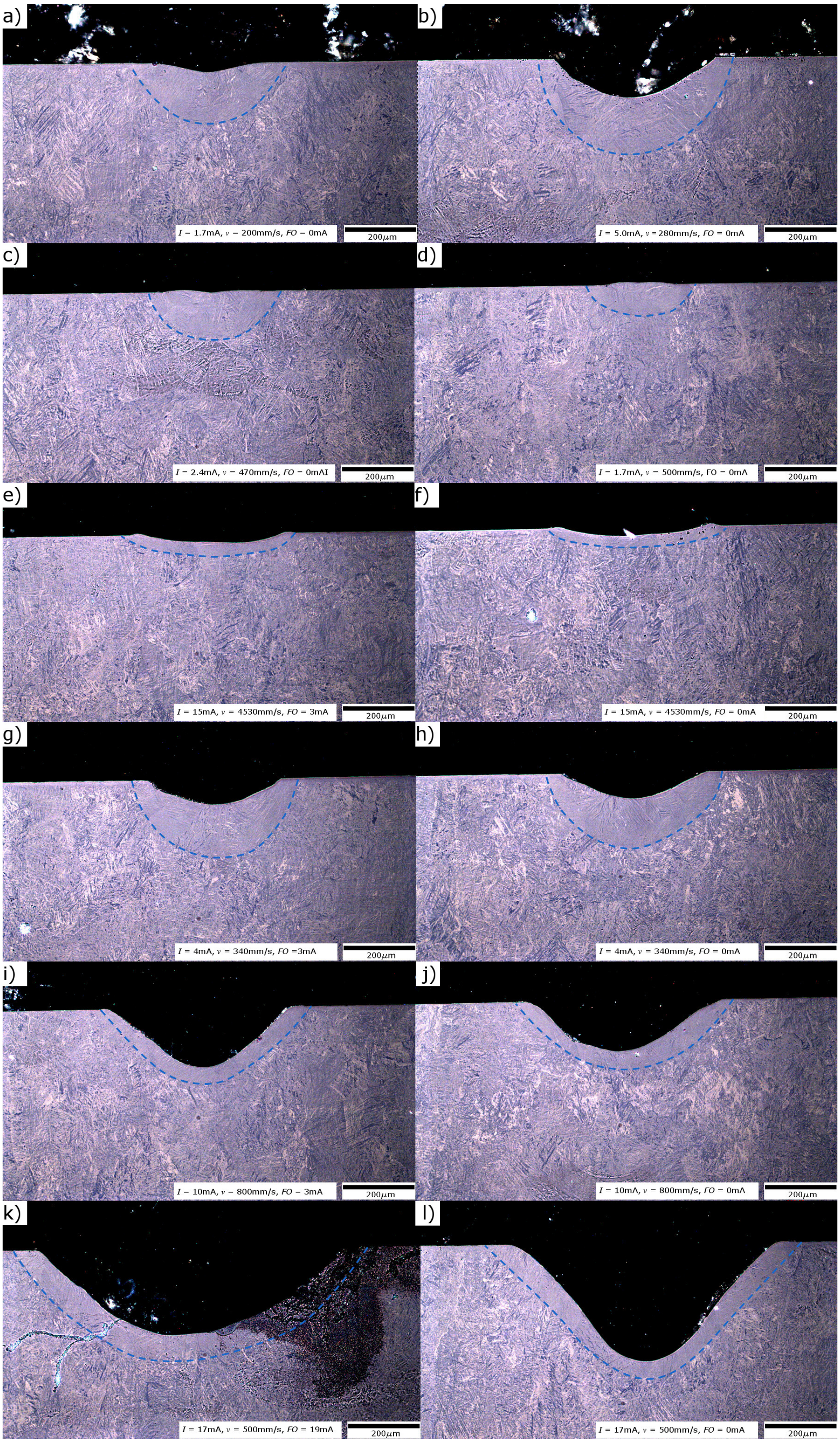

Figure 5.1: Melt pool depths for all the weldtracks according the table 5.1 the blue dashed line highlights the change in microstructure from the affected zone.

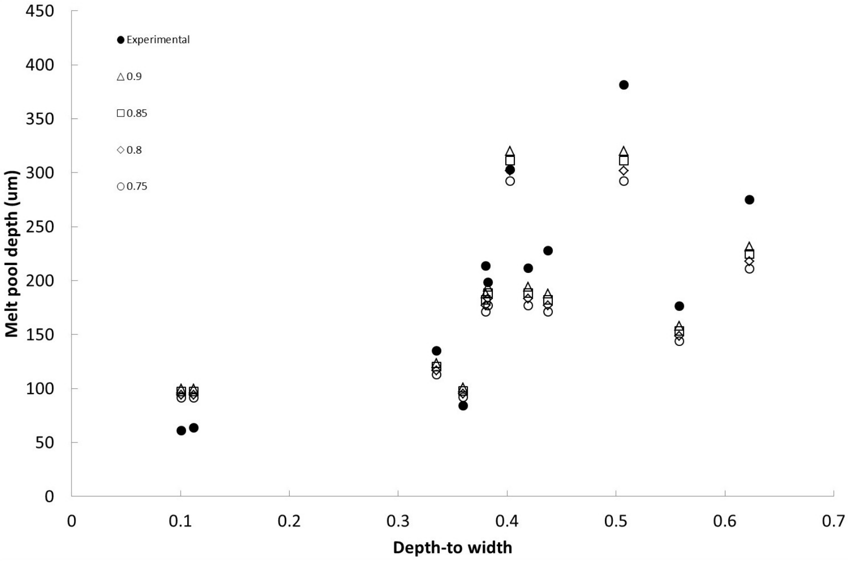

Figure 5.2: Experimental melt pool depth comparison with η values of 0.9, 0.85, 0.8 and 0.75.

numerical models combining point-linear heat sources. Here in this work the η values used (0.75-0.90) show a good agreement for melt pool depth in different situations of melt pool shape. This variety in shape can be seen in figure 5.2; for a single point was found for a value with focus offset = 19, see table 5.1. This limited agreement suggests that additional factors may need to be incorporated into the numerical calculations to approach a better match, possibly taking into account the efficiency with the focus offset influence, internal porosity, and Gaussian energy distributions [124].

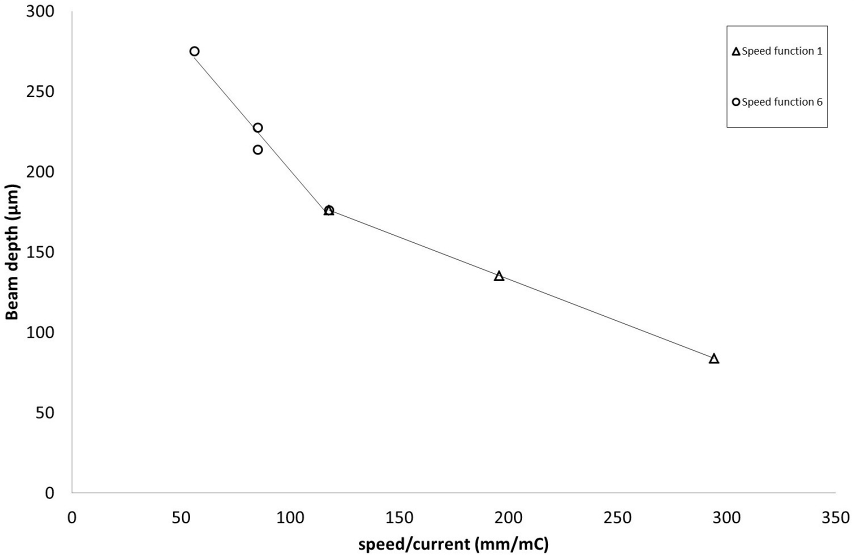

Figure 5.3: Experimental melt pool depth versus the speed/current for two *speed functions*.

Despite the size and shape range found in the weldtracks, the melt pool depth and speed/current are found to be related linearly. This match in absorbed beam with changes for speed and current are a key feature in the melting themes to melt at a constant depth for a particular *speed function*, see figure 5.3.

5.2 Microstructure development

The conditions that define the microstructural development are given by the solidification conditions arising from the beam power to the powder particles. This however complicates the simulation of the melt pool and its morphology considerably. Effects of wettability, heat conduction and density variation between particles are of importance for the solidification conditions leading to irregular shapes of melt pools [41].

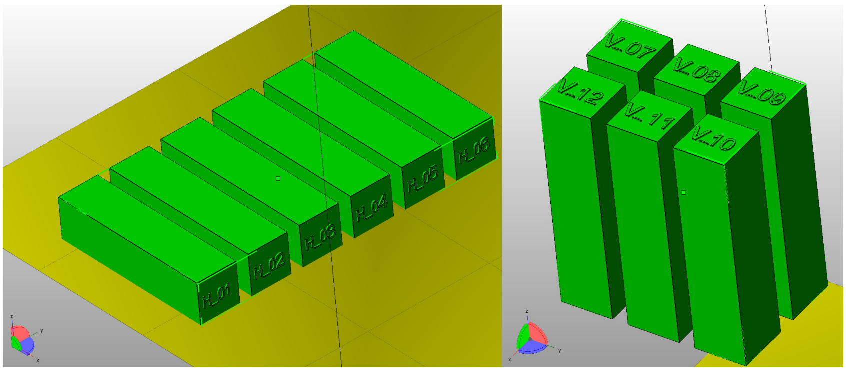

Figure 5.4: Horizontally and vertically oriented EBM specimens for metallographic observations and tensile tests.

In order to characterise the resulting "as-built" microstructure from prealloyed *Ti-6Al-4V* powder melted with the beam parameters mentioned earlier, boxes of 16×16×65 mm were manufactured to be machined into tensile specimens, followed by metallographic observations as shown in figures 4.4, 5.6 and 5.7. The characterisation included two build orientations, horizontally and vertically aligned samples relative to the build orientation, see figure 5.4. Optical microscopy was carried out using polarised light.

5.2.1 As-built microstructure

The identification of the "as-built" microstructure is shown in figure 5.5. The features include traces of a prior β columnar grain and transformed α phases that can be observed in different areas (see figure 5.5a, b, and c). While the columnar β grain microstructure was observed parallel to the build direction, and through few millimetres, a very fine α basket-like microstructure and a diffusionless α' martensite could be seen in different areas.

β grain morphology

As mentioned in chapter 2, the grain size and morphology of the β phase is dependent to the liquid-solid transformation. Until the β transus temperature is reached β grain growth may occur. The rate of this depends upon initial temperature, cooling rate and driving force. Figure 5.5a shows the typical EBM columnar microstructure along the build direction. This columnar morphology is due to the direction of the maximum gradient of temperature during solidification, determining the rapid direction for the grains to grow [127]. This is determined by the heat source on the top surface and the starting plate acting as a heat sink.

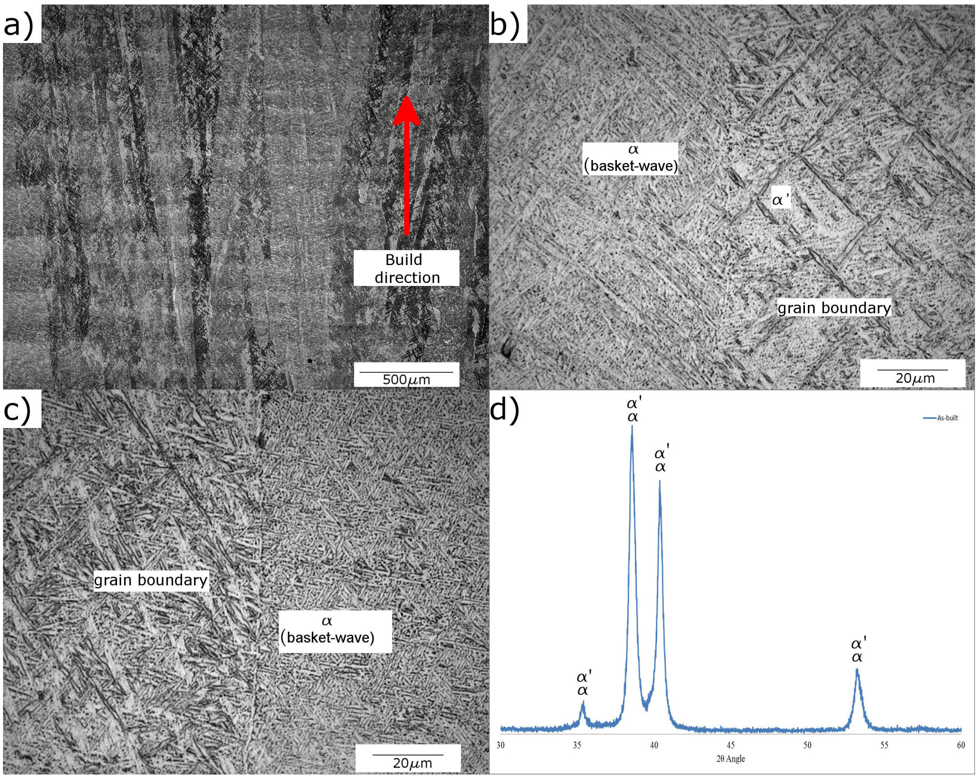

Figure 5.5: (a) Typical columnar β grain microstructure shown for EBM components, the build direction from bottom to top. (b) and (c) showing fine Widmanstatten α and small α colony. (d)XRD pattern for the "as-built" condition

Additionally to the gradient of temperature, the grains also have their preferential growth direction. This is known as dendritic growth. For BCC metals, as in the case of the β phase in *Ti-6Al-4V*, the phase solidifies in the $< 100 >$ direction which is the easy growth direction [128]. This is the case found in figure 5.5, where a columnar β prior morphology goes through many layers of material, the preferential growth following on from the previously nucleated grains.

Transformed α microstructure

Morphology. The transformed microstructure consists of a very fine basket-wave α distributed across the prior β grain, see figure 5.5b and c. Occasionally arranged as colonies, the α laths shown different orientations according the 12 possible orientations relative to the β phase given by the Burgers relationship [129].

Size. The α lath thickness of all samples was measured by the intercept method described in section 4.7.1 showing a mean value of $2.43 \pm 0.44 \mu$m and $2.59 \pm 0.47 \mu$m for horizontal and vertical orientations respectively, see figures 5.6 and 5.7. It can be seen that, despite no significant difference in the mean value of α thickness, a different orientation in the prior β grain can be distinguished as a result of the build orientation. This is of importance if it is taken into account that the strength of lamellar structures (as in the case of "as-built" *Ti-6Al-4V*) is directly related to the α lath size (and α colony) as a component of the effective slip length [45].

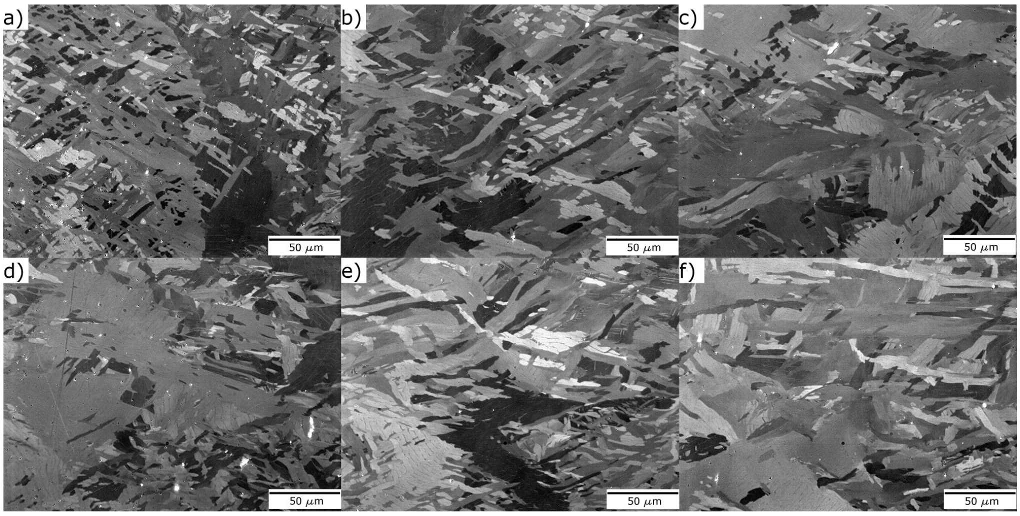

Figure 5.6: Microstructure of the horizontal tensile specimens were a similar α lath thickness can be seen.

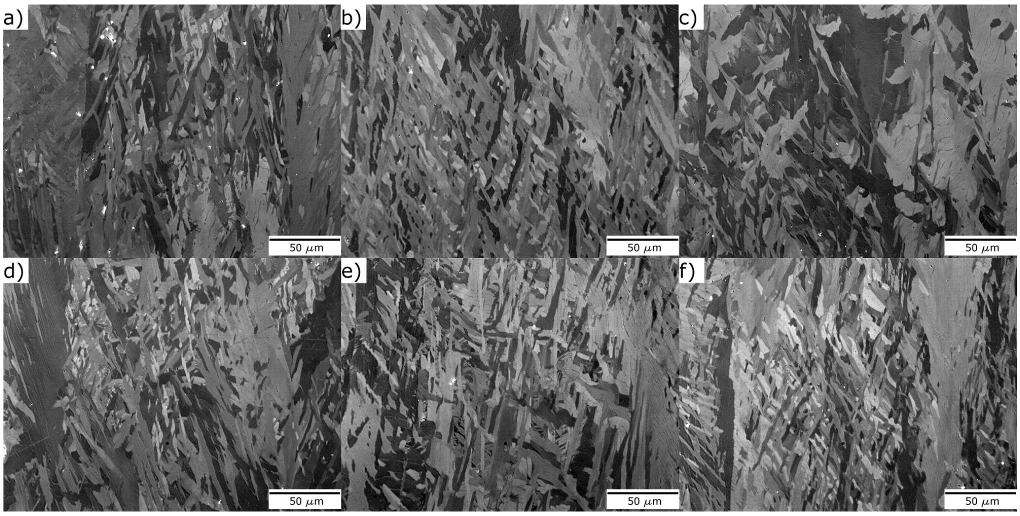

Figure 5.7: Micrographs of the vertical tensile samples showing; the columnar β morphology and relatively fine α laths for all specimens.

Diffusionless martensite (α'). The transformation into α' in EBM *Ti-6Al-4V* has been reported widely [26][31], and attributed to the high cooling rates above the martensite start temperature ($> 410Ks^{-1}$) [5]. The cooling rate for the powder-feed AM process is up to 3500 K s^1 [130], and the generation of α' martensite is expected in the current technique as the cooling rates are anticipated to be comparable. The presence of α' martensite was shown optically and was consistent with the trace obtained through XRD, see figure 5.5b and d. XRD discrimination of the α phase and the α' martensite is not possible since the peaks in the diffraction pattern of both phases coincide as they share the same crystallographic structure.

5.3 Mechanical properties

The mechanical properties discussed here concern to tensile specimens processed by EBM using recycled *Ti-6Al-4V* powder, i.e. powder that has been previously been used in the machine but not incorporated into the artefact made. The chemical composition was assessed on two samples before and after processing, and it was found that the quantities matched closely for each element, with the exception of a aluminium (see table 5.3). It has to be mentioned that due to the process of recycling, the oxygen content was significantly higher compared to virgin *Ti-6Al-4V* powder, see table 2.1.

Table 5.3: Chemistry composition in wt% before (powder) and after (solid sample) the EBM process.

	Al	Fe	V	C	N	O
Powder	6.88	0.18	4.27	0.007	0.026	0.329
Solid sample	6.37	0.19	4.38	0.011	0.029	0.339

It can be seen that besides the oxygen content, all elements fall in the standard range of *Ti-6Al-4V* for cast and wrought material according ASTM F1108 and F1472 respectively. The difference in aluminium, showing a lower level after the process, represents a difficulty of this technique for processing some materials, where the chemical composition of the material is affected by the energy input evaporating such elements. The vaporisation temperatures as a function of pressure has been studied [131] by finding the evaporation rate of an alloy component and calculating the mass transfer coefficient for the surface evaporation. For the solute elements in *Ti-6Al-4V*, the vaporisation temperatures under the vacuum conditions of the EBM process (1.5×10^{-3} Torr) are 1082 and 1687° C for aluminium and vanadium respectively. Comparing these temperatures to those reported in isotherms in the region surrounding of the melt pool (1665° C for *Ti-6Al-4V* in EBM systems) it is expected that the melting temperature will cause a loss in aluminium.

Conversely, the mechanical properties in *Ti-6Al-4V* are strongly related to the oxygen content as mentioned earlier, increasing the mechanical resistance significantly and reducing ductility with oxygen pick-up. Despite the high oxygen content, the mechanical properties obtained fall in the range of as-cast and wrought products, see table 5.4.

5.3.1 Tensile response

The tensile 0.2% yield strength and ductility for the set of 12 samples, six built in each direction are given in table 5.4. Taking all samples together gives a mean and standard deviation of 902 ± 23MPa. Such uncertainty fall within the variability range of 50 to 100 MPa for cooling rates up to 1000°C/min reported in the literature [132]. Despite this agreement, a fundamental difference in the manufacturing conditions exists, the build directions. When the data are examined for these two sets separately there seems to be a clear deviation between the two sets. While the *horizontal* samples display a mean value of 881 ± 8 MPa, the *vertical* specimens show a higher resistance of 923 ± 10 MPa.

Table 5.4: Mechanical properties of the tensile specimens.

Samples	0.2% Y.S. (MPa)	U.T.S. (MPa)	Young Modulus (GPa)	Elongation %
Horizontal	881 ± 8	1040 ± 6	110.0 ± 2.2	16 ± 1
Vertical	923 ± 10	1042 ± 9	116.5 ± 2.8	14 ± 1

Even though the raw materials and the beam parameters were the same, the processing conditions were forced to differ due to the total area where the material deposition was carried out. This can be seen in figure 5.8 where schematic images show the area to be melted, the *scan length*, along with example temperature-time data for different builds. From the graphs, it can be seen that the plateau temperature for the horizontal samples remains almost constant through the whole process. This can be attributed to the higher temperature profile and a more prolonged beam exposure inside the build envelope because of a larger melting area. On the other hand, the temperature profile for the vertical specimens shows a pronounced slope due to temperature losses. Although oscillations are present after the peak temperature (due to powder delivery delays), the final temperature is significantly lower than the specimens from the horizontal build orientation.

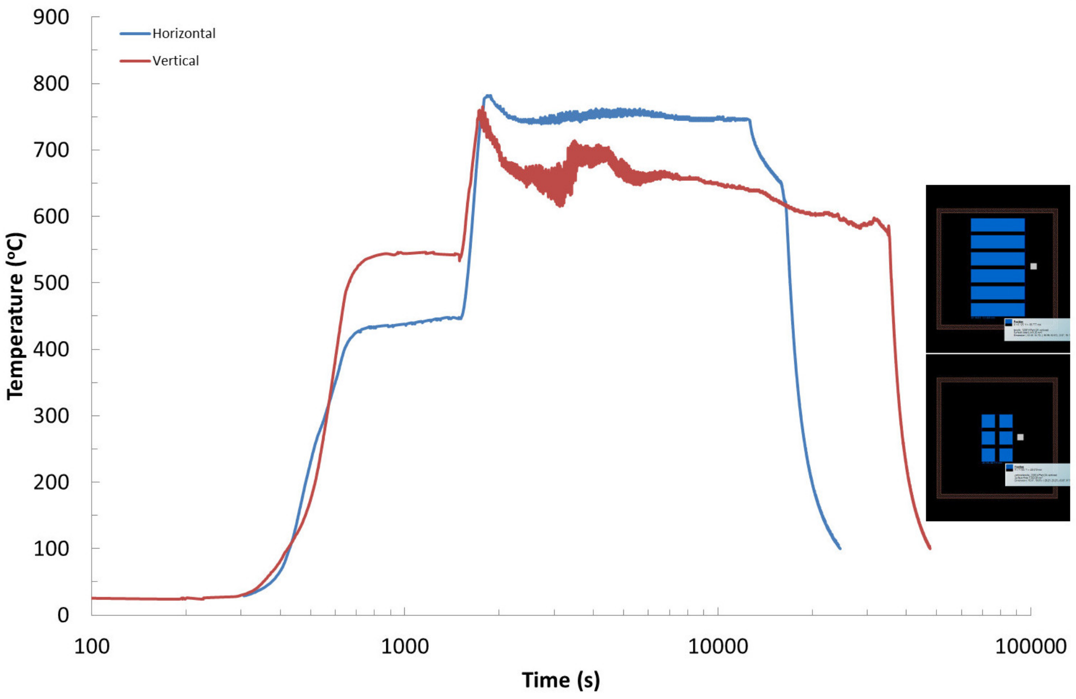

Figure 5.8: Temperature versus time for the two set of specimens. The first drop in temperature represents the *out gassing*, a common cleaning practise for the build chamber before the process starts.

For titanium ($\alpha + \beta$) alloys, the mechanical properties can be related to the platelet thickness of alpha [133]. A typical approach is by Hall-Petch relationships where the α thickness is related to yield strength. Altogether, it is well known that the process temperature and cooling rates may determine the size of the alpha features eventually contributing to the effective slip length and so influencing the mechanical properties [45]. Figure 5.9 shows a compilation of α lath thickness for titanium alloys and *Ti-6Al-4V* manufactured by different routes and electron beam melting. It can be seen that the square root of the lath thickness can be used to give a good guide to the mechanical properties such as the yield strength. The thickness identified from the specimens assessed and those from the current work, are plotted in the same graph. It can be seen that, while the vertical samples display a relatively higher strength, the horizontal samples fit in agreement with the main trend. Although, it is worth to mention that the measurements of α lath thickness in this case could be debated. This is due to the measurements using polarised light may not be precise, especially for finer features, underestimated yield strength correlations.

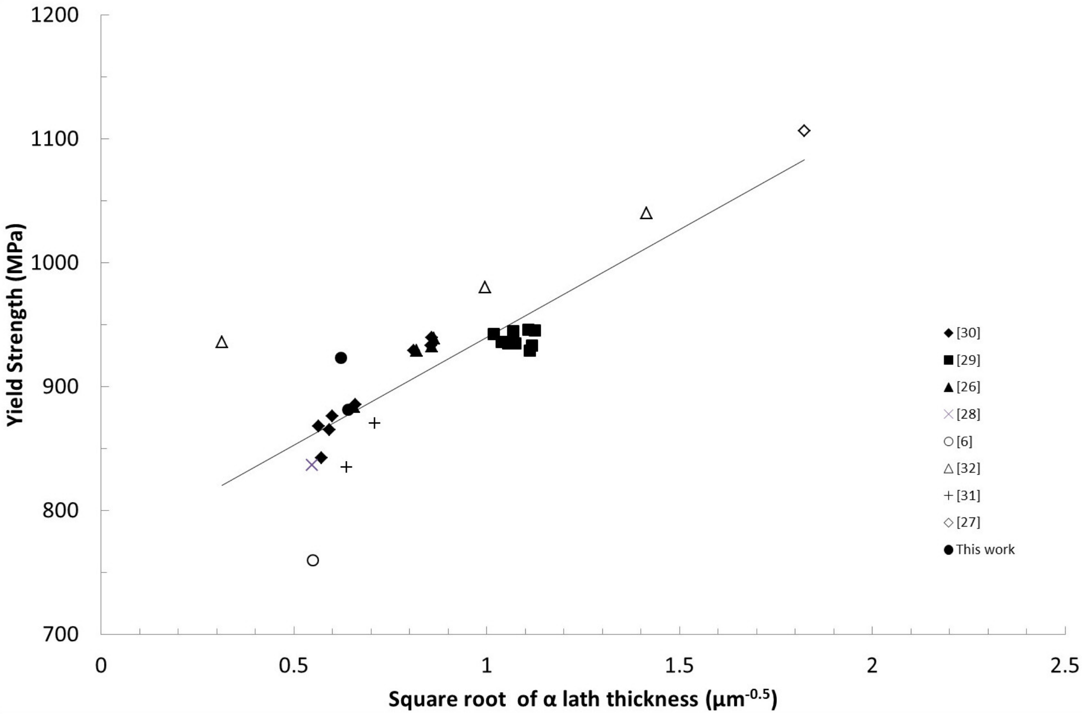

Figure 5.9: Yield strength versus the inverse square root of the alpha lath thickness [6] [26] [27][28][29][30][31][32].

On the other hand, the ductility before failure of *Ti-6Al-4V* is well known to be influenced by the cooling rate during processing, establishing fracture modes during testing to failure. A maximum ductility has been previously reported to be found at cooling rates close to 300°C/min [45]. This is related to a ductile transcrystalline fracture found at low cooling rates and a ductile intercrystalline mode for higher cooling rates [132]. As the cooling rate for the powder-feed AM process is up to 3500 K s^{-1} [130] the expected range of cooling rates for the current process suggests that reduced ductilities will be found in the material produced. For the present investigation, even though the cooling rate values are not reported, the reduction in ductility for the vertical specimens agrees with the expectation of a higher cooling rate from the process, see figure 5.8. The values for the maximum ductility prior to failure are strongly related to the yield strength. This can be seen in figure 5.10 where values from titanium and *Ti-6Al-4V* are shown [27][31][33][34][134]. The values obtained from the two build orientations follow a good agreement with the plotted reported data.

On the other hand, it is well known that the Young's modulus in *Ti-6Al-4V*, as well as yield strength, can be affected by the oxygen content, the heat treatment [135] and texture [55]. Since the EBM process was carried out using high oxygen *Ti-6Al-4V* powder, the levels of Young's modulus were expected to be relatively high; this property is reported to scale linearly with oxygen content [135]. Typical Young's modulus values for *Ti-6Al-4V* are reported to be between 100 GPa to 145 GPa [57] and the obtained values fall within this range. However, it is difficult to assess to what extent the process variables may influence this further by the development of texture effects and cooling rate changes. Even though there is evidence of directionality in properties and microstructure (see figure

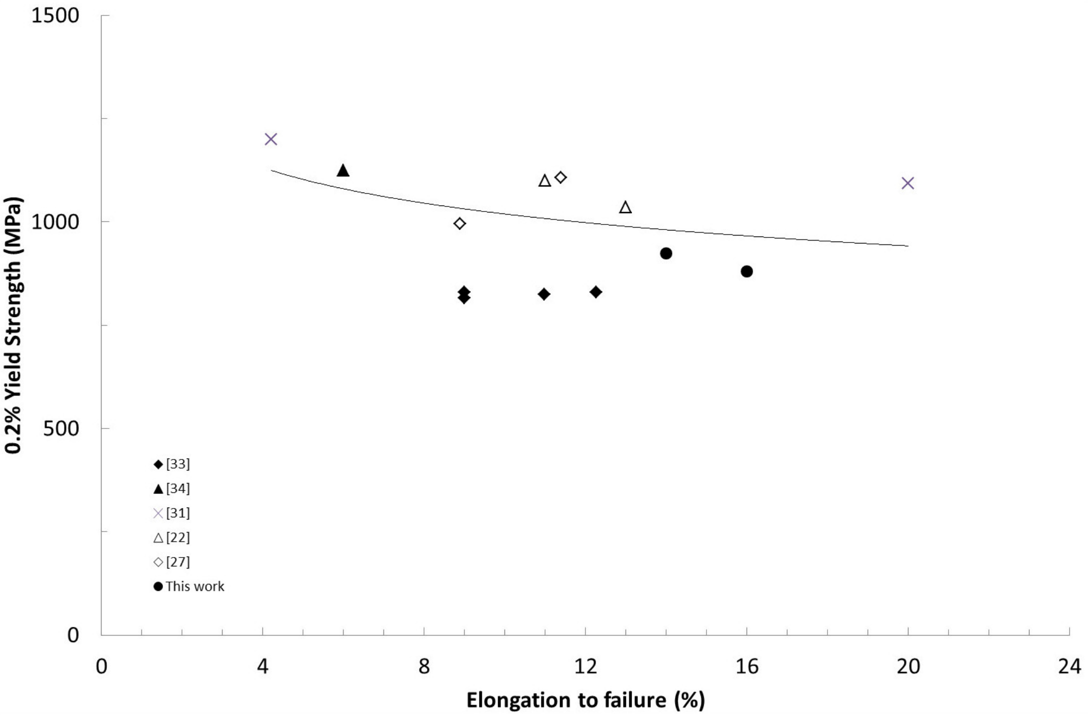

Figure 5.10: Maximum elongation prior failure found in titanium alloys and *Ti-6Al-4V* alloys manufactured by SLM and EBM data from this work and [22][27][31][33][34].

5.11), it is highly complex to assess the contribution in EBM materials. Nonetheless, the values obtained in this research represent a baseline for further work to investigate such behaviours.

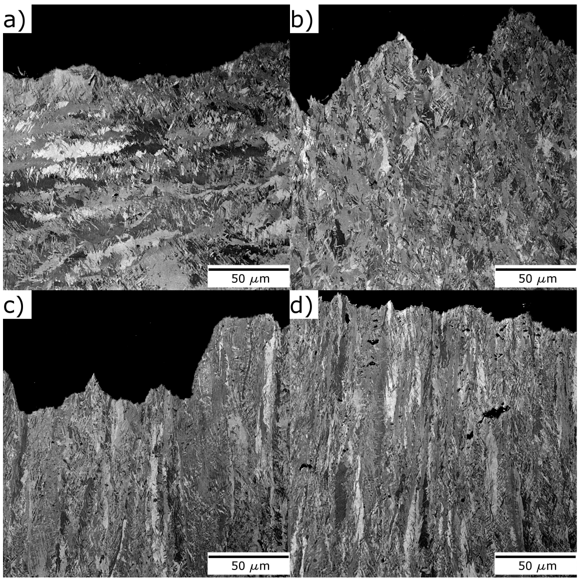

Figure 5.11: Side views of fracture surfaces in horizontal (a and b) and vertical (c and d) specimens after the tensile tests. While the vertical samples show an interrupted columnar microstructure at the failure point, a more random distribution is seen in horizontal specimens.

5.4 Chapter conclusions

In this chapter the electron beam absorption in *Ti-6Al-4V* was analysed after the characterisation of single pass weldtracks on solid material. Its depth was compared to numerical values obtained from a single point heat source model for a set of beam parameters already employed in EBM machines. The match of numerical and experimental values showed that the assumptions of heat source, material properties and process efficiency were acceptable when the depth is compared. Additionally, it was demonstrated that a linear relationship exists between beam melt pool depth with speed/current ratios, concluding that all changes in power and speed during the process reach a constant depth for beam parameters found in ARCAM themes. The same parameters were applied to melt powder particles to obtain tensile specimens for material properties characterisation. The microstructure consisted of lamellar $\alpha + \beta$ within typical β columnar prior morphology parallel to the build direction. Two directions were explored to compare the strength. Despite the similar microstructure, the two directions show a difference in tensile yield strength. These results can be referred to the processing conditions were the thermal histories show different cooling rates because of the scan length, keeping an even plateau temperature for wider melting areas in short heights.

6

The effect of density and feature size on mechanical properties of metal foams

As part of the research of EBM cellular structures, this chapter aims to analyse the compressive response of metallic foams. The topology, constructed by 3D x-ray scans initially represented a volume of “air” and spherical spacers to be inverted into the foam. This geometry allowed to simulate foams made by replication processes [136] with a constant pore location and geometry throughout a set of different samples varied in density. This approach allowed to contribute to the mechanics of foams [97] by tailoring experimentally the compressive response models for materials with this ideal topology [35].

6.1 Files construction

As mentioned earlier, the 3D scan files of two densities (air and glass beads) were reversely engineered to obtain a foam topology, image 6.1. During the data processing mentioned in section 4.2, two threshold values were chosen so the production of two volumes were generated. It is well known that the threshold operations can be critical in order to obtain an improved accuracy of the models to scan [137]. For this case, the achieved degree distortion from the scanned models, was employed to generate two distinct densities only. Further surface dilating and contracting steps of 100 μm using $Magics^{®}$ (figure 6.2), allowed to complete a set of five different densities. In figure 6.3 can be seen that the surface operations did not introduce a significant change to the foam structure, beyond affecting the density.

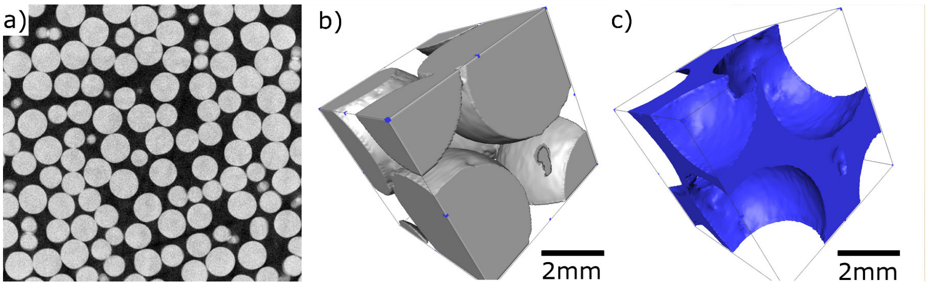

Figure 6.1: Porous foam file creation from: (a) A region taken from a 2-D virtual slice through the 3-D CT image of the 3.9 mm spheres, (b) segmented 3-D representation of a small part of the 3-D image and (c) inverted image showing the spheres as cavities within a solid framework.

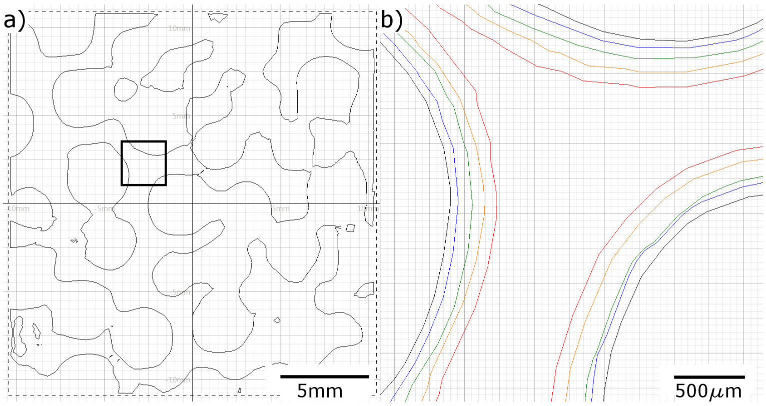

Figure 6.2: 2-D cross-section of the inverted bead pack and (b) a node in the STL files used showing the difference in thickness produced by a surface offset of 100μm.

6.2 EBM manufacturing

The investigation of stochastic structures properties involved the EBM fabrication of three set of samples; the metallic foams, tensile specimens and bending specimens. The testing of tensile and bending specimens was carried out as explained in sections 4.3.1 and 4.3.3.

6.2.1 Metallic foams

A total of 15 samples (three each of the five densities) were manufactured using an ARCAM EBM S12 machine loaded with Ti–6Al–4V prealloyed powder. All foam samples were fabricated in one build operation in order to avoid differences in chemical composition. The electron beam processing was carried out with standard *Net theme* parameters and raw material mentioned in section 4.1. Eventually cleaned with the PRS, an example of each of the five structures is shown in figure 6.3. Weight and volume was measured so their relative density could be obtained, table 6.1. As can be noticed, the density differences between the CAD files and the manufactured samples is similar. Deviations however, exist due to limitations to reproduce the materials as the virtual designs demand. The accuracy from the melting operations need to be such that all parameters, beam energy and beam coordinates, are optimized when changing sections in thickness are required. Further improvements in the beam parameters are therefore needed.

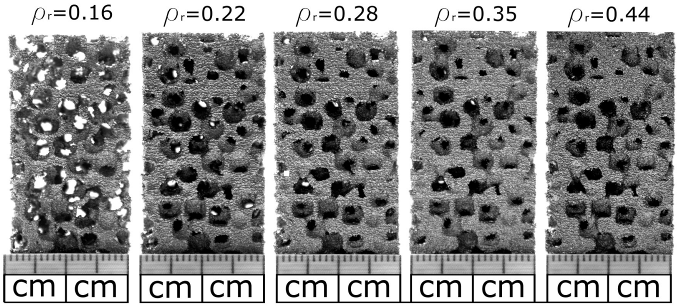

Figure 6.3: Foam samples produced by XCT and EBM, with the measured relative density listed explicitly.

6.2.2 Specimens for parent properties

In order to obtain parent material properties, a set of three rectangular boxes were fabricated to be machined out as tensile specimens. A second EBM build thus was needed as initial fears to disturb the thermal history in the foams build existed. The EBM equipment was prepared with the melt theme mentioned in table 4.1. For this time, the build orientation was chosen as horizontal. Despite the differences found in chapter 5, further research is needed to investigate the thermal history from different build orientations. Potentially modifying the bulk strength and collapse resistance in *Ti-6Al-4V* foams with this topology. Altogether with chemistry changes as powder from this experiments reported a lower Oxygen %wt content of 0.121 and 6.35 Al, 4.19 V, 0.007 C, 0.15 Fe, 0.015 N, 0.0015 H with the balance being titanium.

6.3 Mechanical properties

Following the compression tests, the properties of Young's Modulus, 0.1% yield strength and peak resistance were obtained after the appropriate compression tests. Although there are no strict methods to obtain the yield strength in foams, the 0.1% is reported. In the other hand, the Young's modulus preceded the tangent modulus method.

6.3.1 Compressive response

Upon compression testing and the appropriate machine compliance, all samples tests were reported as stress-strain curves, figure 6.4. In all cases the stress–strain curves shown the initial linear elastic stage, followed by a post-yielding reduction in stress, which was observed experimentally to be coincident with failure of some of the foam struts in a brittle manner. This brittle failure is expected because of the low ductility of the alloy (arising from the low defect tolerance of Ti–6Al–4V [138]). This is not an inherent feature of the structure, as aluminium foams having a similar architecture show a long flat plateau after peak resistance [14].

A list of property values can be found in table 6.1. Because of the intrinsically nature of the experiments the values show a discrete variability. It has to be pointed out that the only variable that may influence the results are the variations in cross sections from sample to sample, and cannot be attributed to the structure. Also, it has to be mentioned all samples were fabricated in the same batch thus eliminating possible variations in chemistry from reused particles having an impact on mechanical properties.

Table 6.1: Mean properties of the 5 set of samples after manufacturing and compression testing

Sample set	File	Virtual Relative density	Measured Relative density	Y.M. (GPa)	0.1% Y.S. (MPa)	Peak (MPa)
I	STL	0.13	0.16	0.65	7.72	11.7
II	XCT	0.20	0.24	1.79	29.7	35.0
III	XCT	0.26	0.28	3.19	48.3	56.7
IV	STL	0.33	0.35	5.63	88.7	102.7
V	STL	0.40	0.44	10.92	119.4	156.9

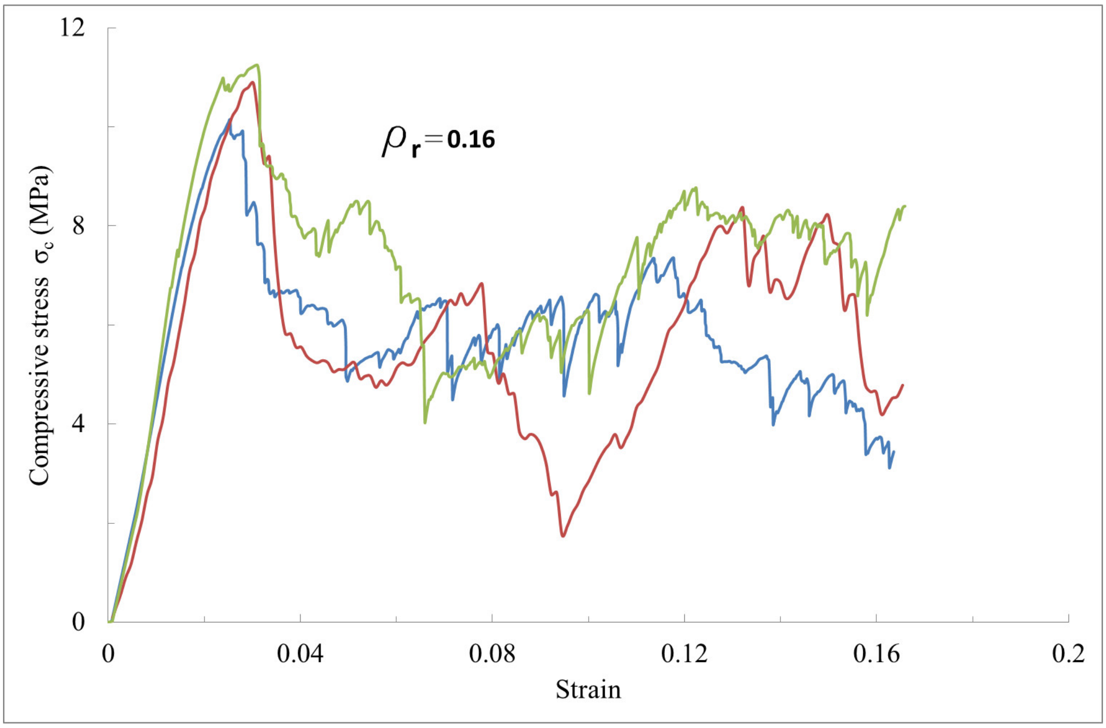

Figure 6.4: Engineering stress strain response of the three foam samples at 0.16 relative density.

6.3.2 Elastic properties

The variation in elastic properties with density is usually expressed in terms of the Young's modulus relative to that of the fully dense parent metal, E_s. Here a value of 114 GPa is taken from tests on 100% dense EBM machined tensile specimens, although in the absence of 3-D CT data it is not possible to ascertain the amount of porosity contained within the struts. Some porosity is likely and this will compromise the properties to some extent [69].

The Young's modulus data is plotted in figure 6.5. The results shown a least squares fit of a 2.96 exponent, giving consistency to the range of values predicted by the model of replicated foams [35]. This falls in agreement where variations in density produce the same structural variation, showing a higher sensitivity to density than other type of foams. It can be seen that although the model captures the trend, the absolute values are over-predicted. This suggests that a constant prefactor must be included, similarly to what is needed in Gibson-Ashby predictions.

Simple calculations report a better fit using a value of 0.053, figure 6.6 (*knockdown* factor of 20 times) indicating a much less efficient structure than the one considered for the Mortensen model. It can be therefore be inferred that imperfect reproduction of the structure in the additive manufacturing process or redundant sections with unconnected members within the solid network exist.

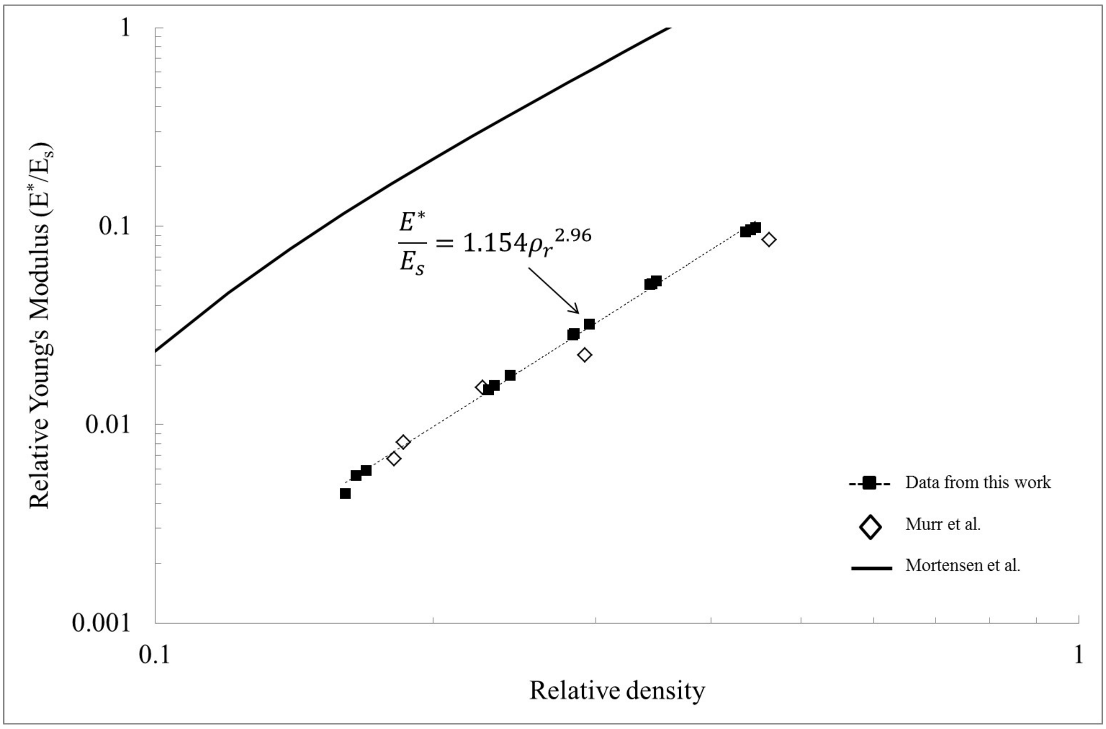

Figure 6.5: Relative Young's modulus plotted against relative density for Ti–6Al–4V foams from this work against the prediction from the model of Mortensen et al. [35]. Additionally, data points are included for other additively manufactured foams from Murr et al. [22].

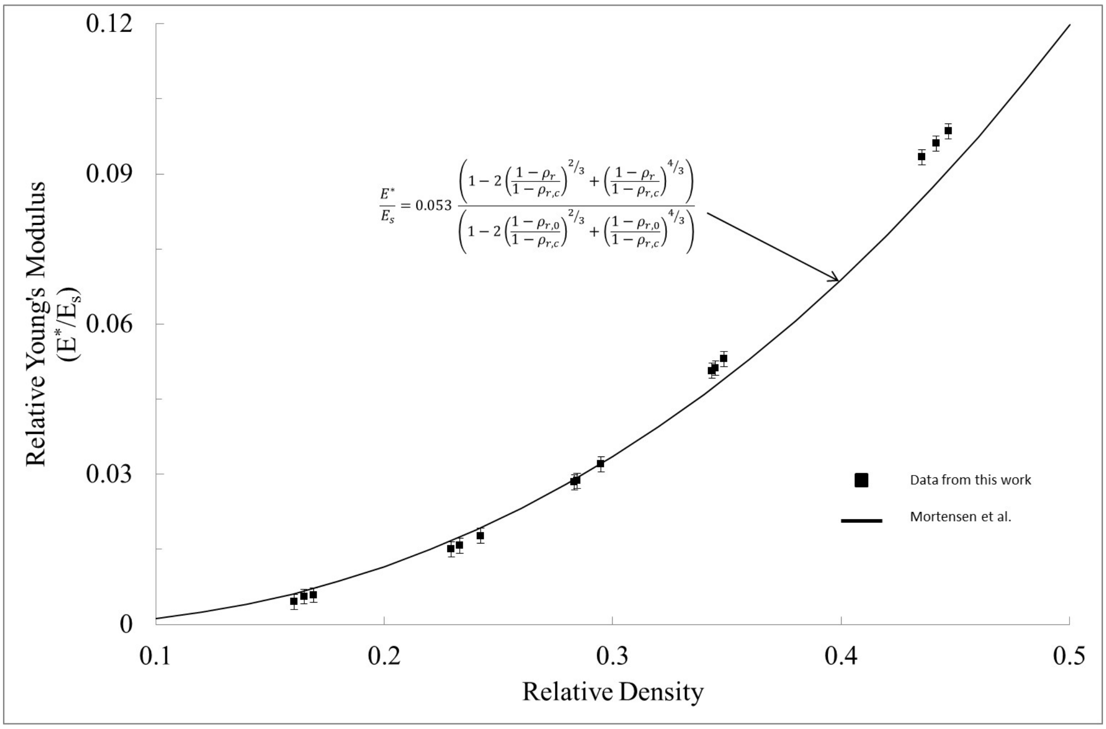

Figure 6.6: Relative Young's modulus data matched against the model from Ref. [35], including a knockdown parameter of 0.053. Error bars represent the standard deviation within tested samples.

6.3.3 Compressive strength

The yield strength-relative density of the foams could be plotted in a similar fashion to the elastic response, see image 6.7. In order to fit the data values to the equations 3.7

and 3.8, a 0.2% Yield strength of 848 MPa was used. Such strength obtained from the tensile specimens machined from nominally fully dense material. Although because of microstructural effects, it is less clear what the correct value of the parent metal strength should be. For comparison purposes, it is worth to mention that similar yield strength values fall within the 5% to the reported data by Al-bermani et al. [26].

Fitting data for the expressions gave a constant value C_2 of 1.67 and an exponent of 2.81. Both values are different from what is normally expected for cellular materials [13]. However, the indicative character of these values allow the equations not to be followed rigorously. Very few has been reported about compressive resistance of EBM foams. EBM *Ti-6Al-4V* foams but other topology shown a similar range of constants [116], matching predictions of equations 3.7 and 3.8. Similarly, *Ti-6Al-4V* foams processed by sintering at 1200°with spherical space holders, therefore alike geometry, show comparable values of 2.28 in exponent and 1.07 as a C_2 constant [139].

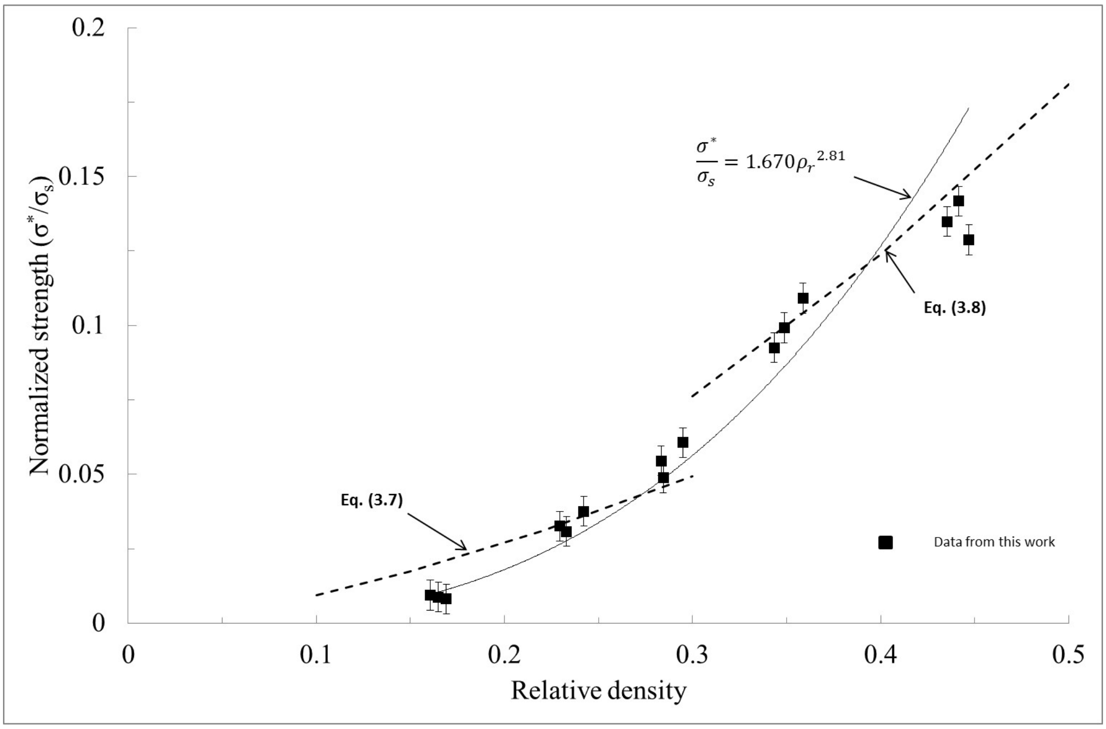

Figure 6.7: Compressive resistance against relative density of the Ti–6Al–4V foam. Multiple fits can be observed from Eqs. 3.7 and 3.8. Error bars represent the standard deviation within tested samples

6.4 Parent metal strength

Theory on porous metal deformation [140], can be used to analyse the resistance to plastic deformation of the constituent metal. This is done by using a modified secant modulus method. This model follows a function linking the Young's modulus to the parent material in order to predict the plastic flow stress, 6.1. Such function acting as a measurement of load bearing efficiency that the foam structure can display.

$$E^* = F(\rho_r) \cdot E_S \tag{6.1}$$

where E^* is the Young's modulus, ρ_r is the relative density, and E_s is the parent metal Young's modulus. It is further assumed that the metal within the foam thus the foam itself, is deformed plastically according to a Holloman power law, equation 6.2.

$$\sigma = c\epsilon^n \tag{6.2}$$

where c and n are constants. The method thus predict a plastic deformation as:

$$\sigma^* = C\epsilon^n \tag{6.3}$$

and

$$\frac{C}{c} = F^{\frac{1+n}{2}} \cdot \rho_r^{\frac{1-n}{2}} \tag{6.4}$$

where σ^* is the stress the foam will support at a certain value of strain, ϵ. The high density foams data was used to obtain the value of n, as these show the large strain before the cell collapse. It is worth to recall that the n value is also predicted to be the same for the bulk metal. The fitting procedure of the equation 6.2 to the initial plastic deformation part of the stress-strain curves gave a $n = 0.124$ as an average. Further adoption of the least square equation (shown in figure 6.4) as the F function is shown as equation 6.5.

$$F(\rho_r) = 1.154\rho_r^{2.96} \tag{6.5}$$

Substitution of equation 6.5 into equation 6.4 with the n value allows σ to be determined by the expression to be found from σ^*. As a result, the variation of calculated matrix stresses for each set of foams is shown in figure 6.8

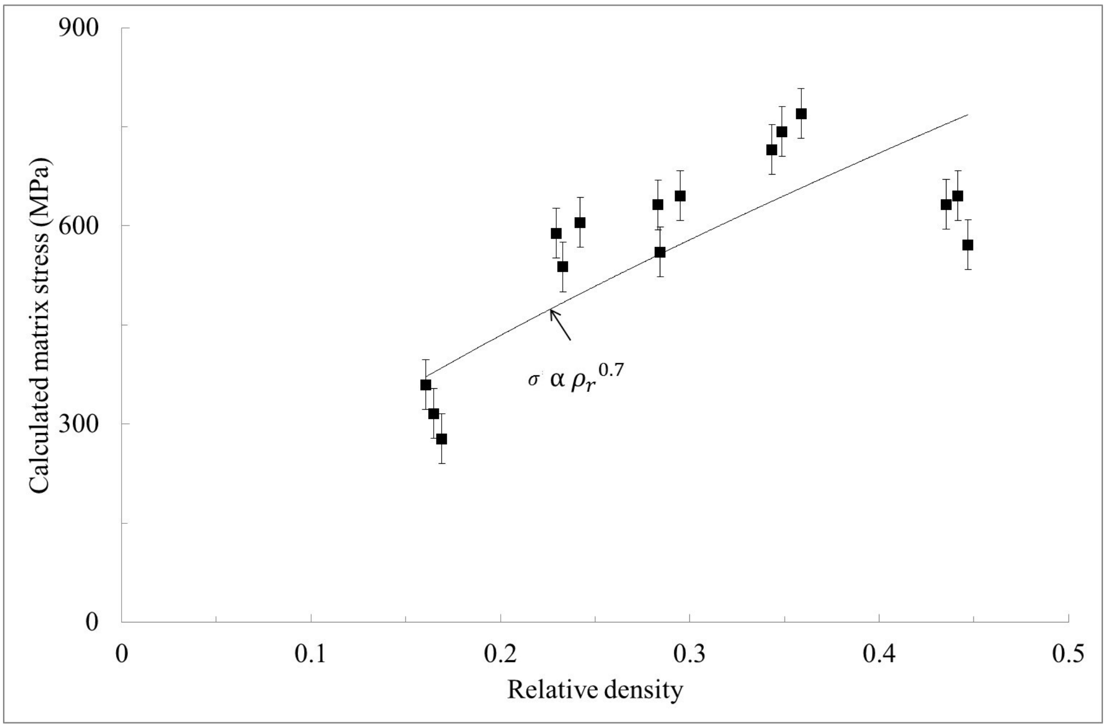

Figure 6.8: The metal flow stresses for all foam samples, the variation with relative density is represented. The error bars represent the standard deviation.

A progressive increment in the parent metal flow stress up to a relative density of 0.35 can be seen. The lower value at the highest relative density may be part of a transition in the matrix strength or, yielding mechanism acting instead of bending. This yielding mechanisms may be an indicative of the high density reported for foams [13], deviating the uniform mode that underlies the assumptions of the method.

On the other hand, the lowest metal flow stress (shown in the less dense foams), may be due to the loss of material from volumetric defects within the body of the struts. This can be highly possible if the fraction of defects remain constant as the solid volume decreases. Moreover, it is worth to recall that all changes of foam porosity are expected to be removed by the analysis. Further studies are also required as factors of phase transformation and textural anisotropy could affect the strength in *Ti-6Al-4V* alloys.

6.4.1 Flexural strength

Complementary to the analysis on the parent metal flow stresses, a study on the flexural strength of fully dense rods has been carried out. Such measurements after the evaluation of three point bending testing, see image 6.9. Although different boundary conditions may apply for the case of flexural strength (supported rather than fixed), the two of them depart from the structural beam deflection analysis. From image 6.9, it can be seen that a fair match of properties an be found for dense rods of 1 mm of diameter. This after taking into account that yield strength of *Ti-6Al-4V* is around 900 MPa for chemical compositions of a %wt of 0.12 [3] reported for these experiments. On the other hand, the tendency of reduced strength in low diameters is consisted with the results shown for the foam response. Furthermore, in order to find the possible causes, characterisation on the mesostructure (3D scanning) and microstructure was carried out.

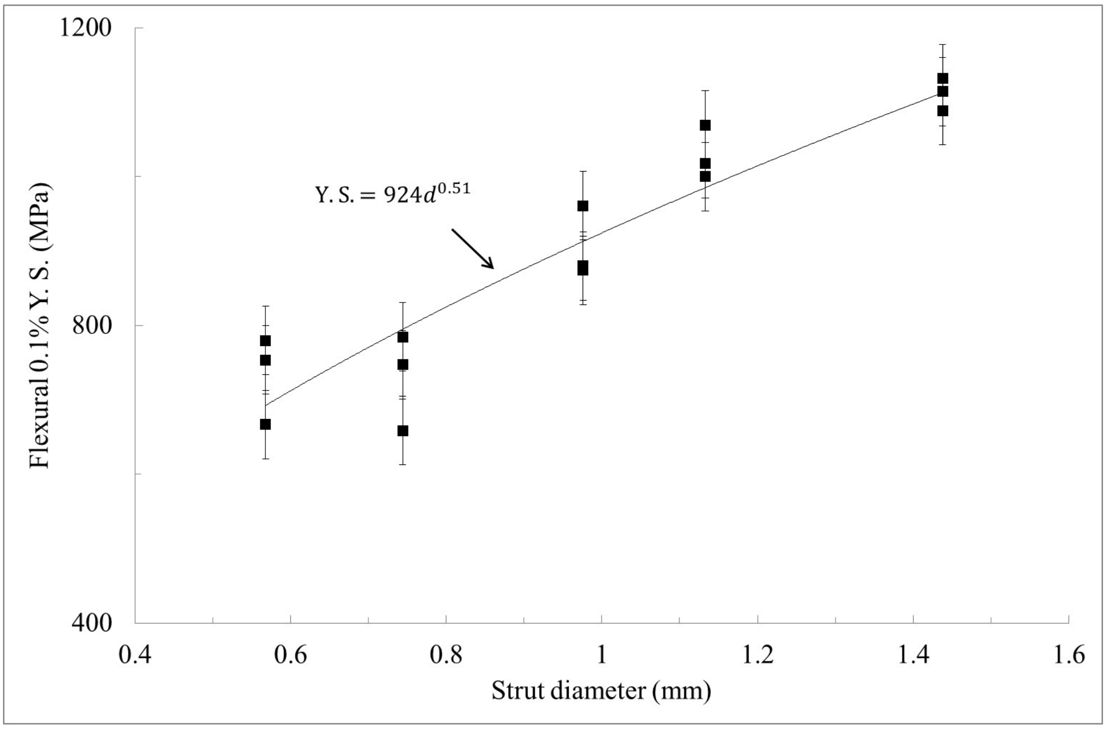

Figure 6.9: Flexural strength variation for fully dense rods of diameters up to 1.5 mm. The error bars represent the standard deviation.

The microstructure developed from the cooling rates was evaluated by optical microscopy. The metallographic results, figures 6.10(a)(b) and (c), shown a fine Widmästatten $\alpha+\beta$ microstructure hardly varying from one strut to another. Although a slightly finer α lath can be appreciated for the thinnest strut , Vickers micro hardness maps do not report a indicate any significant variation, and the average values for each maps are consistent throughout the samples, figures 6.10(d)(e) and (f). The porosity volume fraction is shown in figure 6.12. It can be seen that a fairly constant porosity is found for all struts with the exception of one of 744 μm diameter, fairly isolated. This quasi-constant variation may suggests the porosity found at small sizes is not enough, although not absolute, for the decrease in strength.

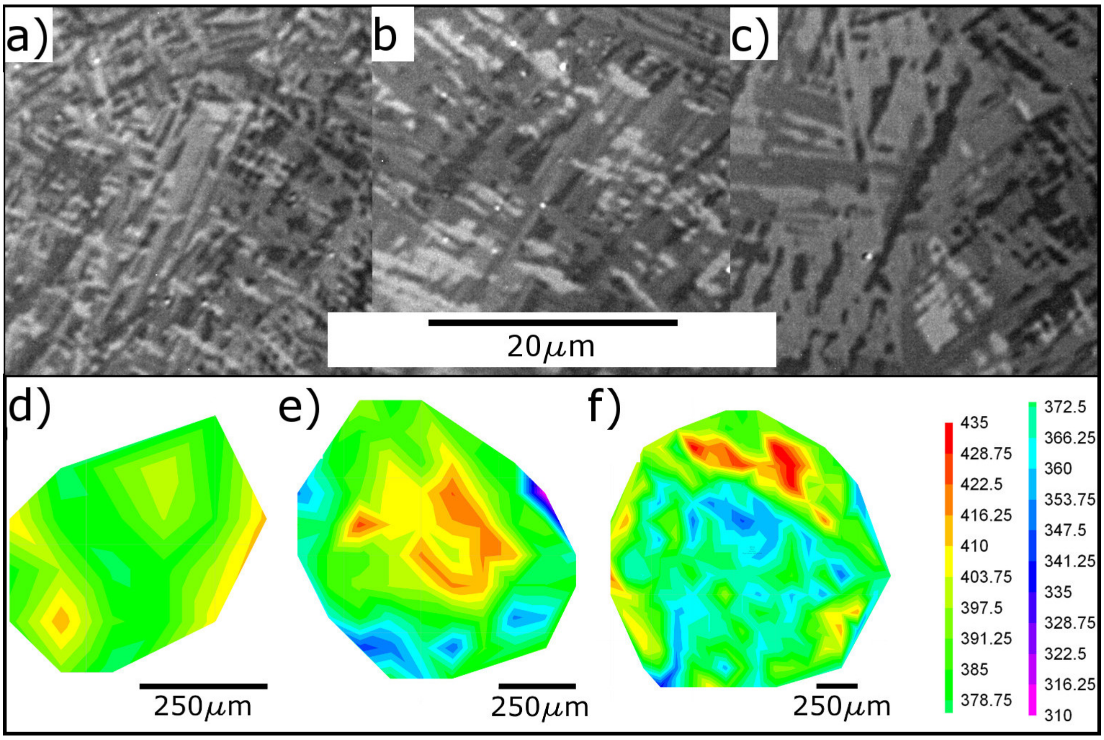

Figure 6.10: Figures (a)(b) and (c) show a Widmästatten $\alpha+\beta$ microstructure within samples of 0.56, 0.744 and 1.8 mm diameter. Figures (e)(d) and (f) show the respectively microhardness Vickers maps.

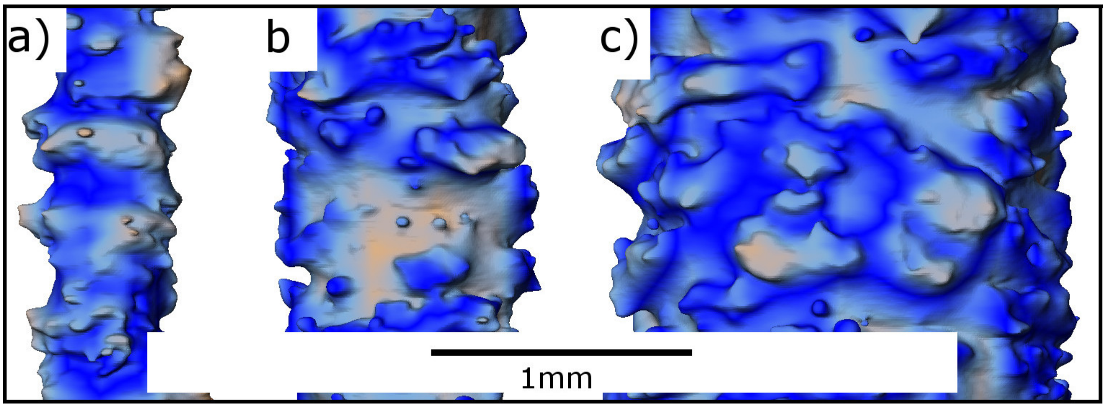

Figure 6.11: Surface representation obtained from the XCT scans for strut diameters of 0.56, 0.744 and 1.8 mm.

On the other hand, the presence of surface stress concentrations at the surface, e.g. notches and cracks, are likely to lower the strength of the struts. This means that, if the likelihood of surface defects and the scale of surface roughness are the same irrespective of sample dimensions, the effect on the strength will become more significant for the thinner struts. From the XCT scans of the rods shown in Fig. 6.11(a)(b) and (c), the scale of the surface roughness remains comparable (of the order of 100 μm) as the rod diameter is changed. It is therefore suggested that, of the possible contributors to the decrease in strength at smaller diameters, this is likely to be the most significant.

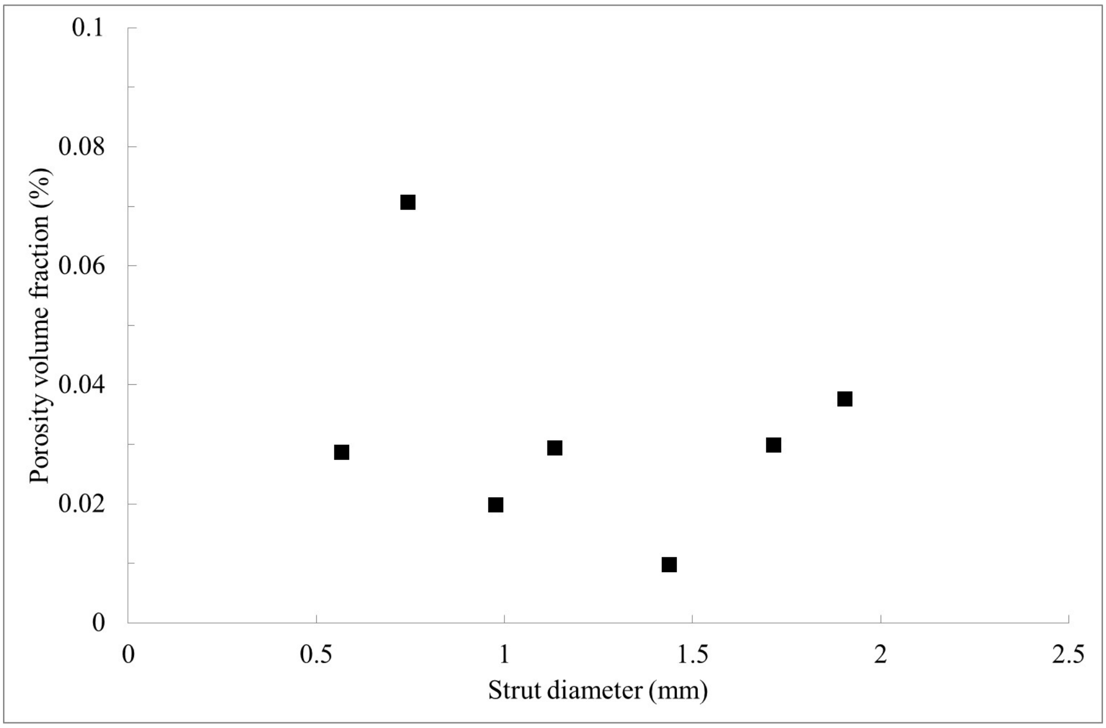

Figure 6.12: Variation of the porosity volume fraction in different strut diameters.

6.5 Chapter conclusion

A 3-D model of a porous foam with stochastic structure and uniform pore size was obtained by imaging a random array of glass spheres using XCT. This was used as a template for the production of five stochastic foams having the same geometries and pore arrangements but thicker walls (and hence higher density), thereby allowing the effect of this variable on the strength of foams to be systematically investigated.

When additively manufactured in Ti–6Al–4V by EBM these samples were found to display a variation in Young's modulus that was different from that predicted by the ideal case of Gibson and Ashby in that the exponent relating stiffness to relative density was not of order 2 but of order 3. This exponent has been predicted by Mortensen et al.[35] on the basis that the shape of the stiffness determining controlling struts evolve with relative density differently from that of the material as a whole.

The yield strength of the foams was also found to increase approximately as the third power of the density. For strength, the variation against relative density was found to be in accord with previous results on materials with similar structures processed by other means [13]. An alternative model developed for the replication processed foams captures the trend and shows good correlation with the data on elastic properties reported here, provided a knockdown factor of ∼20 is used. This is a large decrease in the properties from that predicted, even though this factor can cover a wide range. It is likely to be due to the foam structure produced being very inefficient, with a large amount of material concentrated in the nodes where struts meet, adding mass but contributing relatively little to the strength. By the application of a modified secant modulus model the yield stress for the parent metal was deduced for each foam and the results indicate a decrease in yield stress with decreasing strut dimensions, at least for fine struts.

Further investigation through the measurement of flexural yield stress on nominally fully dense additively manufactured rods shows a similar fall in yield stress as the diameter was reduced. It is speculated that this is likely to be due to the effect of the surface roughness of material processed by EBM. This suggests that, in order to retain parent material strength values (as obtained here from tensile test machined EBM samples), the section size of components should be kept above a minimum value in the region of 1 mm.

7

The effect of defects and microstructure for lattices loaded under equilibrium conditions

This chapter is devoted to the study the effect of defects departing from equilibrium conditions. In order to assess it, cubic-like lattice structures were manufactured at different densities. A detrimental effect on the compressive response was found when the microstructure is affected by heat treatments above the $\beta - transus$ temperature followed by furnace cooling (FC). No significant change in mechanical resistance was observed for heat treatments below the $\beta - transus$ with FC. Analytical predictions are employed to validate the effect of defects under compression. Although a considerable fraction of defects such as; internal porosity and surface roughness, plus volume mismatch, the experimental results agreed the analytical model.

7.1 Materials processing

The samples processing included the design and EBM fabrication for compression testing previously described in chapter 3 and detailed in the following subsections.

7.1.1 Structure design

The sample design started with the construction of a cubic unit cell in Netfabb, figure 7.1a. Furthermore, the unit was duplicated in a 20 × 20 × 20 mm volume to generate the lattice sample, figure 7.1b. The lattice thus was exported as STL file (Standard Tessellation Language), representing cubic volumes of four unit cells, 5mm in side length each. The cross sectional profile for the struts was fixed as an octagon (figure 7.1c), making it possible to form with a relatively low number of triangles in the STL file, while permitting a relatively rounded shape to be produced. By doing this, a fast transferring step to the EBM software is expected. Furthermore, STL files (figure 7.1d) have been converted into 2D as “sliced” files for manufacturing purposes. Four different strut diameters were used; 0.8, 1, 1.5 and 1.8mm each with a 5mm unit cell size. The calculations to determine the relative density of the structures designed were therefore based on the smallest repeating element, being the ratio of solid volume, V_s, for three intersecting cylinders within the volume of a unit cell V_u, shown in figure 7.1 and equation 7.1.

$$\rho_r = \frac{V_s}{V_u} = \frac{3V_c - 3V_{I2} + V_{I3}}{l^2} = \left(\frac{d}{l}\right)^2 \left[\frac{3\pi}{4} - \frac{d\sqrt{2}}{l}\right] \tag{7.1}$$

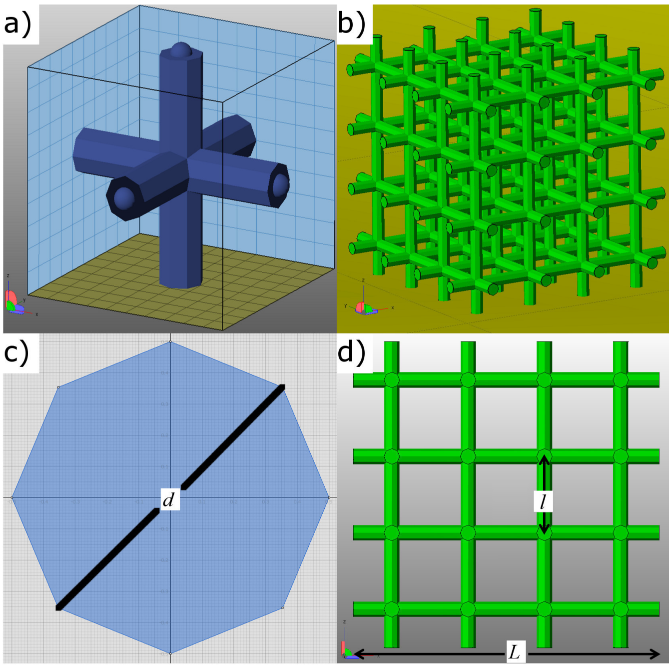

Figure 7.1: a) Unit cell designed as the minimum repeatable symmetric unit, b) Samples populated with the unit cell, c) Cross section profile as an octagon of diameter "*d*", d) Lattice front view showing dimensions of sample length "L" upon compressive load.

where V_c, V_{I2} and V_{I3} are the volumes of a cylinder of length L and diameter d, the intersection of two cylinders and the intersection of three cylinders respectively.

7.1.2 EBM fabrication

18 lattice samples were manufactured for compression testing: 12 (3 of each strut thickness) for testing in the "as-built condition" (i.e. with no further heat treatment) and 6 (of 1.5mm strut thickness) were heat treated. In addition, 9 (66 × 16 × 6mm) cuboidal samples were made from which tensile bars were machined. The samples were fabricated using the same titanium powder as used for the lattices, but using the EB "Melt" settings described in table 4.1. Intended for the processing of larger volumes without the requirement to produce small features accurately, the melt theme employed a faster speed and increased beam power. Upon build completion, values of relative density (from measurements of lattice dimensions and mass) and strut diameter (using callipers) were taken and reported in table 7.1. Figure 7.2 shows an example of each type of lattice. Although in general a good reproduction of the lattices was found, strut dimensions differed from the specified

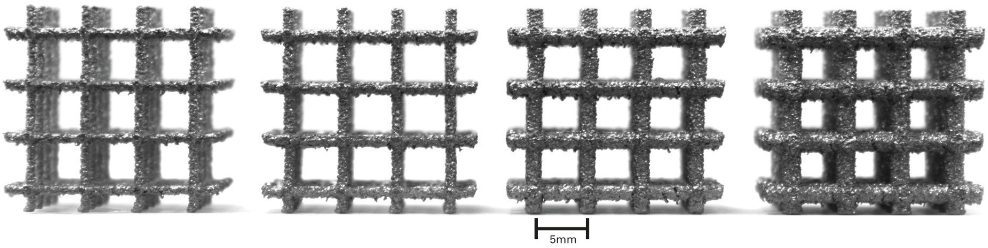

Figure 7.2: EBM manufactured Ti-6Al-4V scaffold samples. The STL strut diameters were 0.8, 1, 1.5 and 1.8mm.

designs. In almost all cases (see table 7.1), undersized member diameters were found, possibly due to the offset in the contour parameters not being optimal. The effect of the mismatch in strut dimensions can be observed in the deviation of measured relative density from predictions for low densities. However, there are also departures where the actual density is lower than the predicted one. This can be an indication of a lack of solid volume throughout the lattice; the presence of holes for example. As the material added during the AM process has a tendency to collapse in unsupported areas, this unfilled volume may potentially be located in the horizontal trusses of the lattices where such collapses are more likely. Conversely, vertical trusses are expected to show a better integrity as the pre-deposited material is self-supportive. A more precise measure of the mismatch can be seen from the results with CT scanned specimens. The parametric measurements are also reported in table 7.1. Only the struts which macroscopically had strut dimensions coinciding with those designed are reported in this section. As can be seen no data is shown for struts designed as 0.8mm and only calliper measurements of these struts will be used for further analysis.

Table 7.1: Comparison between specified and observed strut diameters and relative densities for the "as-manufactured" lattices. The uncertainties were estimated based on the standard deviation from each batch of samples.

Number of samples		Strut diameter (mm)			Relative density	
Batch	Specimens	STL	Callipers	Parametric study	Analytical	Experimental
1	3	0.8	0.81 ± 0.022	No data	0.05	0.063 ± 0.003
2	3	1	0.97 ± 0.023	0.88 ± 0.252	0.08	0.079 ± 0.004
3	9	1.5	1.48 ± 0.019	1.35 ± 0.223	0.17	0.158 ± 0.002
4	3	1.8	1.78 ± 0.028	1.65 ± 0.216	0.23	0.216 ± 0.005

7.2 Investigation of thermal histories

Three thermal treatments were explored; "as-manufactured", heat treated high in the α+β region and heat treated above the β–transus temperature. The temperature profiles of the heat treatments (which were carried out under high vacuum) comprised a heating rate of 10° C/min to 960°C or 1200°C for 2 hours followed by furnace cooling (FC). The former (960°C/2h/FC) was designed to retain the columnar β grain microstructure. It is reported that during heat treatments in the $\alpha+\beta$ region the α phase can be altered without a significant effect on prior β grains [37]. The second heat treatment (1200°C/2h/FC), which is usually not applied for bulk *Ti-6Al-4V*, was intended to break down the typical columnar β grain shape that is found in EBM components [26]. Such microstructure forms because of the directional formation of the specimens and the preferred growth direction of the material.

While the cuboidal samples were machined to tensile specimens after the heat treatments, the heat treated lattice samples were compressed without any further processing. Once machined, the tensile bars were sent to Special Testing LTD, Sheffield, UK, and tested according to ASTM E8 standard to obtain 0.2% Yield Strength, Ultimate Tensile Strength, elongation and Young Modulus, table 7.2.

7.2.1 Lattices in the "As-built" condition

Microstructures from optical microscopy for material in the "As built" condition are shown in figure 7.3. Three areas were imaged (Figure 7.3a) to compare the microstructures; the middle height of a vertical strut (figure 7.3b), the top section of a horizontal strut (figure 7.3c) and sections close to the start plate where the EBM build begins (figure 7.3d).

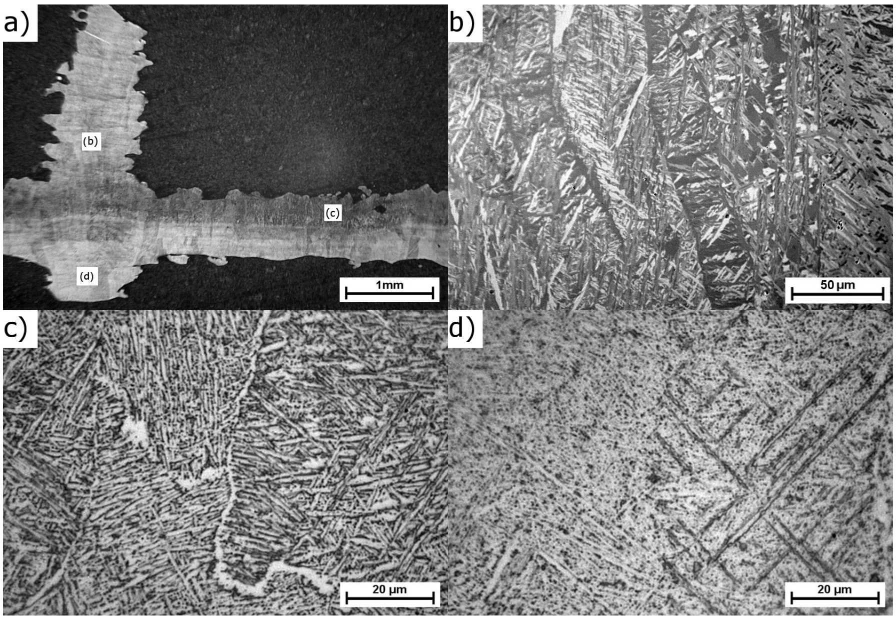

Figure 7.3: Microstructural features in "As built" bulk microstructure: (a) Lattice build orientation from top to bottom, (b) columnar β prior grains, (4c) $\alpha + \beta$ wave basket microstructure and (4d) diffusionless α'martensite.

The deposited material shown a microstructure composed of columnar prior β grains parallel to the build direction, (figure 7.3b). Such traces, are highly dependent on solidification route as they are the easiest structure to solidify from this alloy. The decomposition products were identified as a basket-weave structure, interestingly observed in areas within the final deposited layers and close to sintered (i.e. unmelted but adhered) powder, figure 7.3c. Also, diffusionless α' martensite in areas close to the start plate is identified, figure 7.3d. Such features have been reported for titanium alloys under similar solidification conditions [37]. Such a distribution seems to be related to areas subjected to different thermal conditions affected by the heat flux away from the electron beam to the start plate. This is not homogeneous throughout the solidified material, as areas surrounded by sintered powder become relatively more highly insulated than those close to the build start plate.

The formation of α' martensite in EBM bulk components has been debated recently [26]. For lattice structures [22], it is related to the low thermal mass of the structure, leading to the transformation of martensite due to high cooling rates (> 410 Ks^{-1}) above the martensite start temperature [5]. As mentioned earlier in chapter 4, the cooling rates for AM are expected to be higher therefore developing α' martensite.

Additional evidence showed a thinner α within a basket-weave microstructure plate compared to the microstructure in tensile samples, table 7.2. This is the result of different

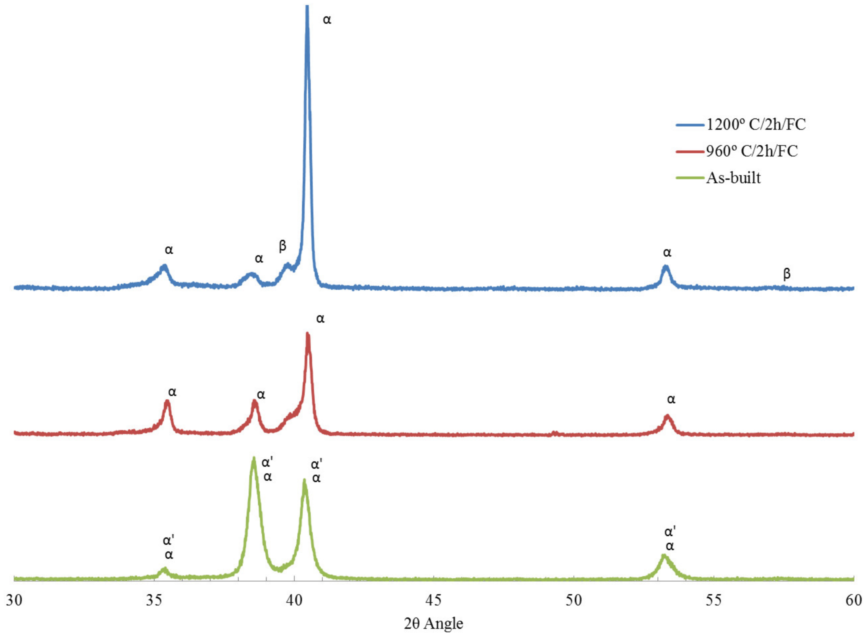

Figure 7.4: X-ray diffraction scans of Ti-6Al-4V lattice truss sections in; a) as built EBM condition, b) 960°C/2h/FC and, c) 1200°C/2h/FC samples

cooling rates experienced owing to the difference in thermal mass, between the lattice structures and the bulk blocks produced for fabrication of tensile samples. It is well known that the cooling rates in $\alpha + \beta$ titanium alloys from the β phase field determine the size of α laths and α colonies, although occurring at different ranges. Previous investigations have shown drastic reductions of α lath size appears upon cooling rates of 1.66 Ks^{-1} resulting in reductions from 5μm to about 0.5μm and further reductions to 0.2μm for cooling rates up to 133 Ks^{-1} [45]. Because of higher cooling rates experienced by lattice structures as mentioned earlier, it seems reasonable that the thickness of α laths found here fall are around 0.8μm. Because of this high cooling rate, further reductions in lath thickness would be difficult to achieve by thermal processing. This could be desirable because the microstructural scale is linked to mechanical properties. The hardness values of around 3.49 GPa found for the metal making up the lattice structures is in agreement with previous observations [43].

7.2.2 Lattices in the 960°C/2h/FC condition

After the 960°C/2h/FC heat treatments, a clear modification in the microstructure from the “as-built” condition can be seen in figure 7.5a and (c). As previously mentioned, the heat treatments in the $\alpha+\beta$ region were applied expecting a modification on the $\alpha-$phase morphology without significantly changing the prior β phase grains. This is indeed what is observed for the lattice samples (figure 7.5a) and the tensile specimens (figure 7.5b) where a microstructure of columnar β grains from the as built condition is retained. Additional X-ray diffraction showed no crystallographic modification, figure 7.4b, as the $\alpha-$phase could be identified in the “as-built” condition. In the other hand, microstructural changes in the form of alterations to the $\alpha-$phase morphology, mainly consisting of coarser α plates were observed, table 7.2. Additionally, no significant fraction of α' martensite could be found using optical microscopy. This in agreement with annealing heat treatments applied in the high $\alpha+\beta$ temperature range on the dense alloy, where a martensitic microstructure

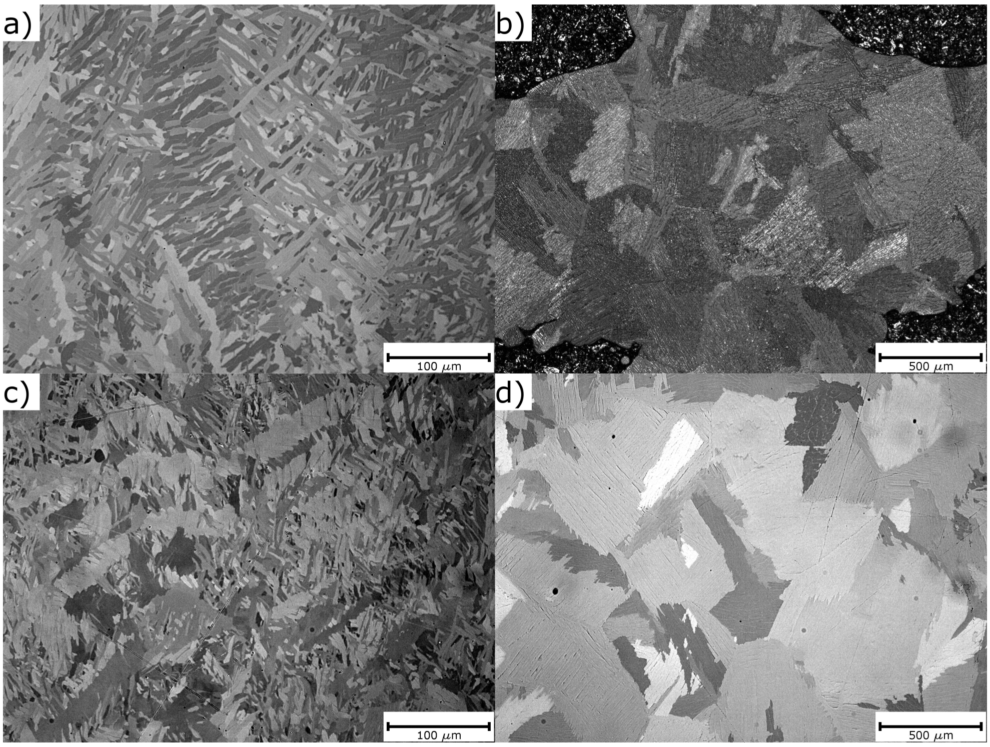

Figure 7.5: Microstructure of lattice specimens; (a) and (b) after 960°C/2h/FC and 1200°C/2h/FC heat treatment respectively. Tensile specimen microstructure; (b) and (d) after 960°C/2h/FC and 1200°C/2h/FC heat treatment respectively

can be changed to $\alpha + \beta$ lamellar form [45].

The consequences of the microstructural homogenization were validated through microhardness measurements, table 7.2. Indentations on the lattice structures showed no significant difference to those on material in the "as-built" condition. This can be seen as a mechanically unchanged $\alpha + \beta$ microstructure from the "as-built" condition, although with a coarser α plate thickness, making the absence of martensite not significant for the strengthening mechanism [45]. Because of high similarities with the "as-built" properties it could be suggested the EBM microstructure is equivalent to annealed materials after the process.

7.2.3 Lattices in the 1200°C/2h/FC condition

In contrast to the lower temperature heat treatment, heat treatments above the $\beta-$transus temperature drastically modify the as-built microstructure. This is achieved through a degree of homogenization (at 1200°C for 2h) and retained by a slow cooling rate (FC). As a result, α and β partitioning in a diffusion-controlled mode can occur, producing a lamellar microstructure of broad α and fine β alternating lamellae packets, figure 7.6a. The $\beta-$phase can be identified this time through XRD, figure 7.4. This microstructure seems to be dominant without changing throughout the strut section, figure 7.6b, mainly composed of plate-like α organized in α colonies and α boundaries within the prior β grains.

Because of this coarsening, the mechanical resistance of the metal making up the lattice specimens, evaluated through Vicker microhardness, decreased significantly from the "as-

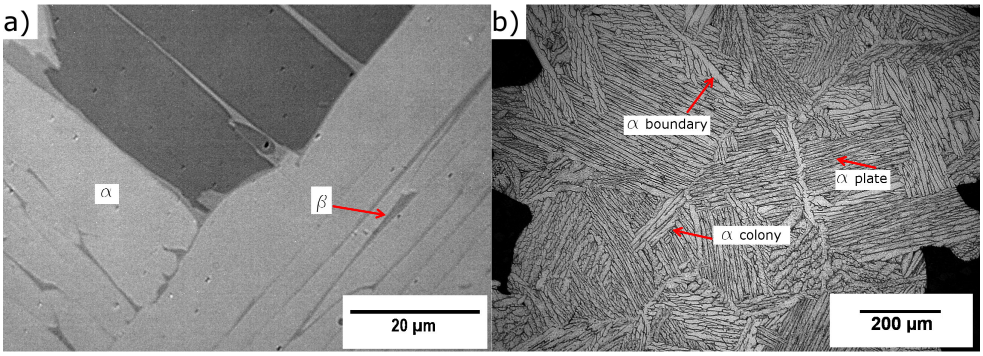

Figure 7.6: a) Alternating α and β lamellae packets, b) Equiaxed grains with a α plates-like and α grain boundaries across the lattice strut member

built" condition, as expected. However, upon comparison with the microstructure and microhardness values in the tensile specimens, higher values are found with a similar α plate-like microstructure, figures 7.5b and 7.5d.

The effective length of the α colonies was evaluated by the mean intercept length method for randomly oriented lines [25]. The lattice structures had a colony length of $110 \pm 20\mu$m while micrographs of the tensile specimens showed the length to be $180 \pm 150\mu$m (no information about colony shape or morphology was obtained in either case). This suggests that the difference in size is related to the degree of recrystallization achieved in both volumes. This recrystallization effect has been seen on wire deposition additively manufactured structures after similar heat treatments [141], and also in microstructures after cold and hot working [142]. This is attributed, to some extent, to the high dislocation density created from going at high cooling rates from the β phase region giving an important driving force for the recrystallization process. As the "as-built" EBM microstructure has been suggested to solidify at high cooling rates, therefore a strong tendency to recrystallize through a high dislocation density is latent.

As the heat treatment was applied to the specimens produced from different material deposition strategies (*hatching/contouring*) further studies are necessary to investigate the generation of dislocations and their effects on deposited EBM *Ti-6Al-4V* materials. In this study, it is observed that in heat treatments above the $\beta-$transus temperature with FC applied to thin sections, as in the lattice samples, the excessive coarsening generated a small number of grains across the width of the struts (see image 7.6b), contributing to a decrease in mechanical properties discussed in the next section.

7.3 Compressive response

Strain-stress curves examples of the *Ti-6Al-4V* lattice samples under compression are shown in figure 7.7. As mentioned earlier, all samples were axially loaded in the EBM build direction. One sample with a relative density of 0.15 (a 1.5mm strut diameter in the STL file), is shown for each condition. In the early stage of compression, a linear elastic region was displayed, followed by a peak and subsequent strength reduction. The latter feature represents the failure of the sample under load. The values for the collapse strength exhibited a systematic variation as a function of relative density, ρ_r, reporting: 23.7 ± 2.4 MPa, 34.7 ± 1.5 MPa, 180.2 ± 14.3 MPa for batches 1, 2 and 4 respectively, for batch 3 see table 7.2. Once plotted, the data was approximately fitted by a power law of exponent

Table 7.2: Microstructural features and mechanical properties comparison for the lattices and tensile samples in the three conditions under study

Samples	Batch 3 (condition)	$\alpha-$lath thickness (μm)	Vickers microhardness (GPa)	0.2% Y.S (MPa)
Lattices	As-built	0.9±0.5	3.5±0.1	88 ± 1
	960°C/2h/FC	6.3±1.5	3.5±0.2	85 ± 2
	1200°C/2h/FC	13.8±1.1	3.1±0.1	67 ± 9
Tensile specimens	As-built	2.9±0.9	3.5±0.1	850±13
	960°C/2h/FC	4.1±1.2	3.5±0.1	865±5
	1200°C/2h/FC	9.2±2.7	3.6±0.2	783±6

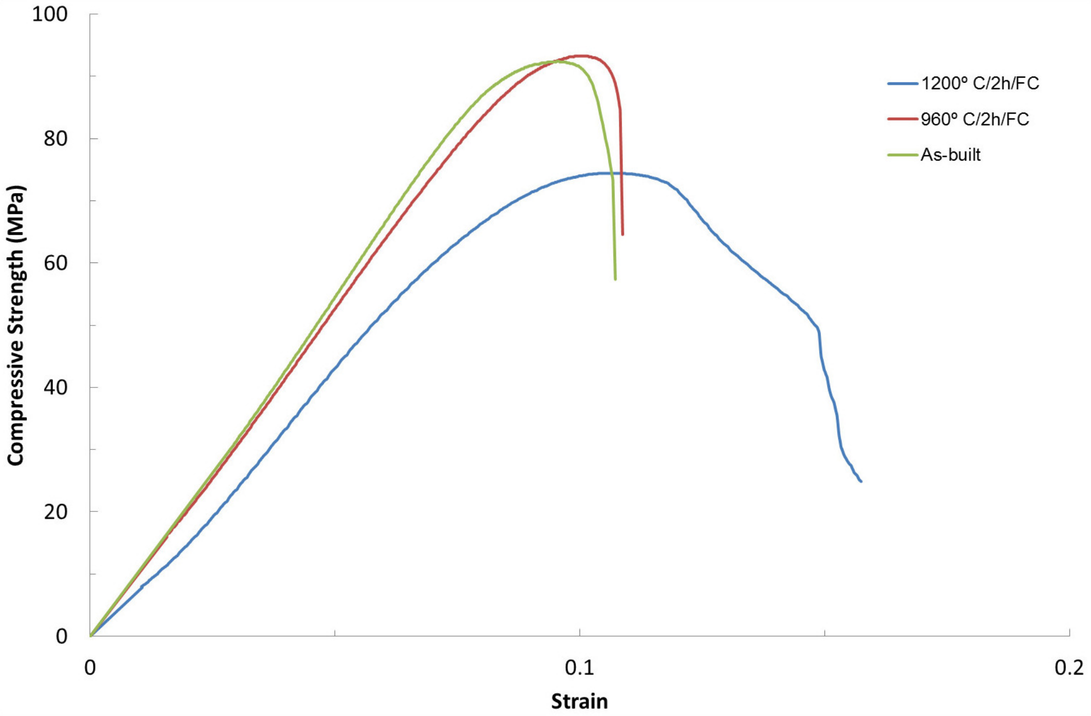

Figure 7.7: A lattice stress-strain curve for each condition from batch 3 showing linear behaviour followed by the maximum peak resistance and failure as a sudden drop in stress supported.

1.63 determined by the least-squares method (see figure 7.8), in broad accordance with equation 3.7 albeit with a significantly higher constant of proportionality out of the range commonly reported for some cellular solids, e.g. metal foams [14]. This can be seen when comparing the two curves plotted in figure 7.8, where a significant difference is found from the simple bending dominated behaviour model, which gives rise to equation 3.7 [13]. This departure in prediction can be seen as a consequence of increased density structures seeing significant increment in volume (which of course contributes to the density) in parts of the structure that do not carry a significant fraction of the applied load, i.e. strut members orthogonal to the applied load direction. As a result, while one side of the trend (samples with low density) shows a closer match to the model predictions, the opposite shows a significant difference.

In order compose an analytical model to predict the properties under compressive loading, a few assumptions need first to be taken into account. First, among the possible stresses acting under loading only axial stresses are considered, see eq. 7.2.

$$\sigma^* = \cancel{\sigma_{beding}} + \cancel{\sigma_{shearing}} + \sigma_{axial} \tag{7.2}$$

Hence, the lattice failure force (F^*) can be calculated from the failure force acting on each of the vertical trusses only (f^*). Axial stress upon compressive loading can therefore be derived based on the forces acting on the number of vertical trusses (n) in x and y direction that is n_x and n_y, see equation 7.3.

$$F^* = n_x n_y f^* \tag{7.3}$$

Substituting the lattice and truss member failure force in each term (F^* and f^* respectively) by the product of stress and area ($\sigma \times A$) gives,

$$\sigma^* A^* = n_x n_y \sigma_s A_s \tag{7.4}$$

where the lattice area A^* is the squared sample length L^2 and L is defined as length of the truss (l) times the number of trusses in x or y direction. Analogously, for the solid truss member of yield stress σ_s and circular cross area of A_s gives the failure stress in equation 7.5 as,

$$\sigma^* = \sigma_s \frac{\pi}{4} \left(\frac{d}{l} \right)^2 \tag{7.5}$$

where d and l are the strut diameter and the unit cell length respectively. Substituting the relative density term (equation 7.1) into equation 7.5, it gives:

$$\sigma^* = C \sigma_s \rho_r \tag{7.6}$$

where $C = \frac{1}{3-(\frac{4\sqrt{2}}{\pi})(\frac{d}{l})} \approx 0.286$ for the range studied here. Such constant C is left to be compared with previous models for metal foams [13], and cubic core structures made of fibre composites [143], the last one obtained after derivations of the critical strength of individual members based on the assumption of no interaction among other truss members than the axially loaded. These constants fall within the range for cellular solids for scaling relationships [14] however, their character is merely indicative helping in the early stages of design. It has to be noted too that the parent material properties σ_s were taken from the parameters measured in the tensile test. This is valid for yielding values (in tension–compression) as it represents the early material instability after the linear elastic region, although taking any further point from the curve would be misleading as plasticity from necking effects may be present [50]. Furthermore the assumption is made that struts fail by compressive yielding, not by elastic buckling.

The experimental data fit well to this simple model based on pillar compression (Figure 7.9) indicating that the initial yield is determined by pillar compression and not buckling at this strut lengths and diameters and secondly, that the yield strength of the bulk additively manufactured material is representative of that in the finer struts manufactured here. The proximity of the curve for the onset of buckling approaches the compressive yielding curve for our struts at 0.81 mm (batch 1) diameter suggest that they are close to the buckling condition.

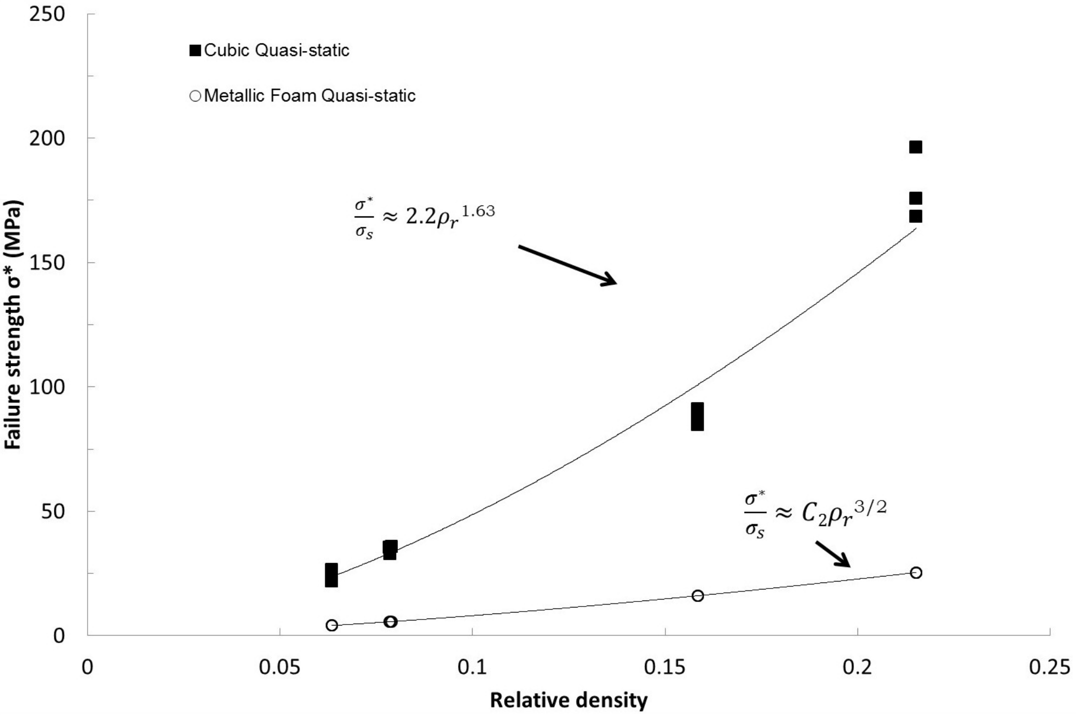

Figure 7.8: Compressive resistance found in lattice samples compared to current models for cellular materials with a C constant of 0.3.

Indeed pictures from the test (Figures 7.10 a and b) seem to confirm this as prior to failure, as a type of cooperative buckling with linked nodes resisting the deformation; however, shearing stresses need to be considered as well. If the strut is analysed locally, it can be seen that their length-to-diameter ratio decreases from node to node as the relative density increases. This becomes of importance for samples of batch 4 where a potential shear distortions can affect the total strength (σ^*). This is suggested as the shearing effects under compression are likely to be present if a length-to-diameter (l/d) is as low as 2.5 [50]. These conditions are close to those present in batch 4 (1.8 mm diameter and 5 mm length) where SEM images show a transition in fracture, from a microvoid coalescence to a cleavage fracture see fig. 7.11. Despite this transition in fracture and the flow of stresses determining the total lattice strength, the prediction based on yielding mechanisms suggests a satisfactory tendency for the range tested in this investigation.

The buckling calculation is included (see figure 7.9) to highlight that this failure is above the experienced mode. As all possible collapse mechanisms compete, the one with lowest stress is the dominant. It can be seen that a buckling failure mode seems to be close at low strut diameters for this topology (batch 1), and pictures from the test (7.10a) seems to confirm this as prior to failure the deformation of all vertical struts can be appreciated. However, yielding at every node is still the dominant mechanism matching the equilibrium model. Although, it has to be mentioned that, as table 7.1 shows, batch 1 samples displayed that element diameter because they are oversized. This is due to resolution capabilities further discussed in section 3.5. In the other hand, the figure 7.10b shows a dramatic fracture along the entire layer leaving no place for deformation of neighbouring strut elements. The influence of the parent material properties is shown in figure 7.12. While the "As built" and 960°C/2h/FC samples shown a 1.8 and 2.7% deviation from the predictions, 1200°C/2h/FC samples deviated up to 11%. This can

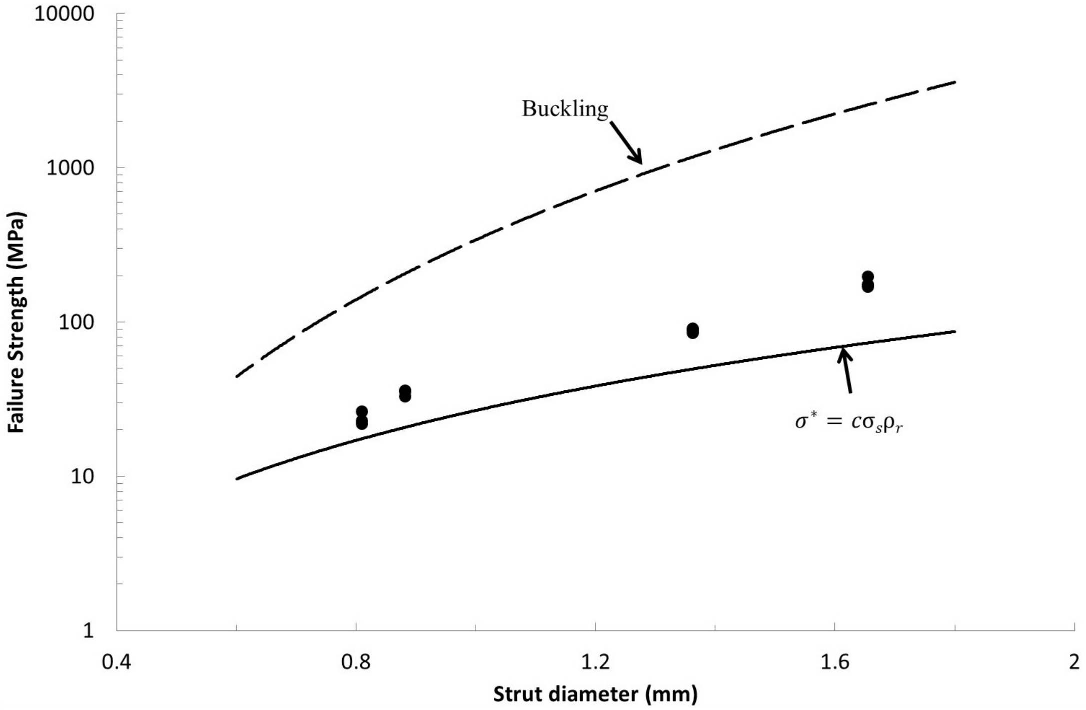

Figure 7.9: Experimental data and analytical model prediction. The buckling failure mode was calculated as the height of one layer with nodes built in that cannot rotate therefore using a column effective length factor k of 0.5.

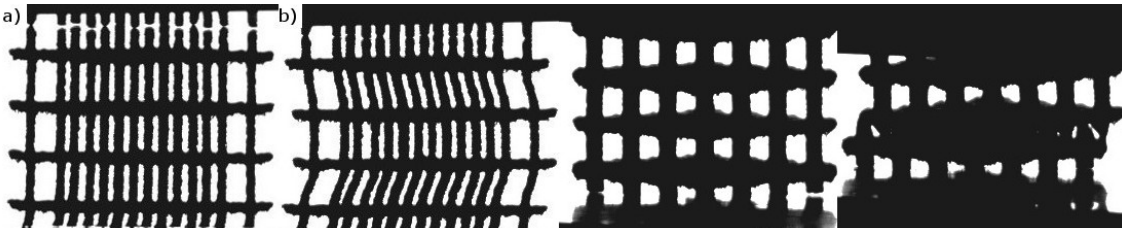

Figure 7.10: Silhouette images from the video extensometer showing the pre-test and post-yield (pre-failure) forms of samples from batch 1 (a, b) and batch 4 (c, d).

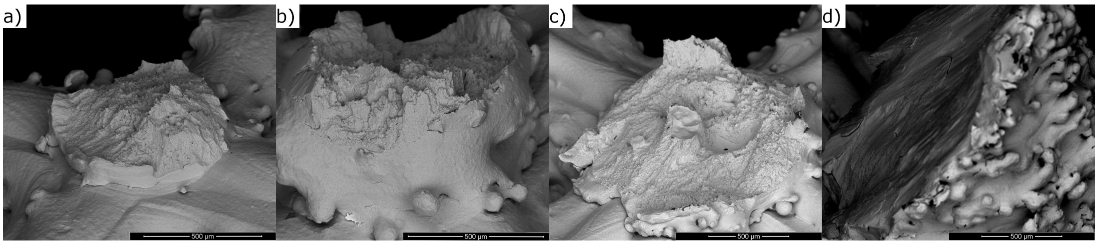

Figure 7.11: SEM images of the node fractures for the compressed specimens, 0.8, 1, 1.5 and 1.8 mm in diameter respectively. A transition in fracture can be seen from a “dimpled” one to a cleavage fracture.

be matched from the tensile properties reported in table 7.2 where the Yield Strength is considerably lower for the samples heat treated above the $\beta - transus$ temperature. This difference can potentially be attributed to the detrimental effect of a coarse microstructure in narrow sections. Similar effects have been noted for annealed β in thin sheet form where the possible formation of a single β grain microstructure through the thickness could drastically affect the resistance [37]. Although it is unknown up to what strut diameter the yield resistance can be affected by similar heat treatments for topologies presented here.

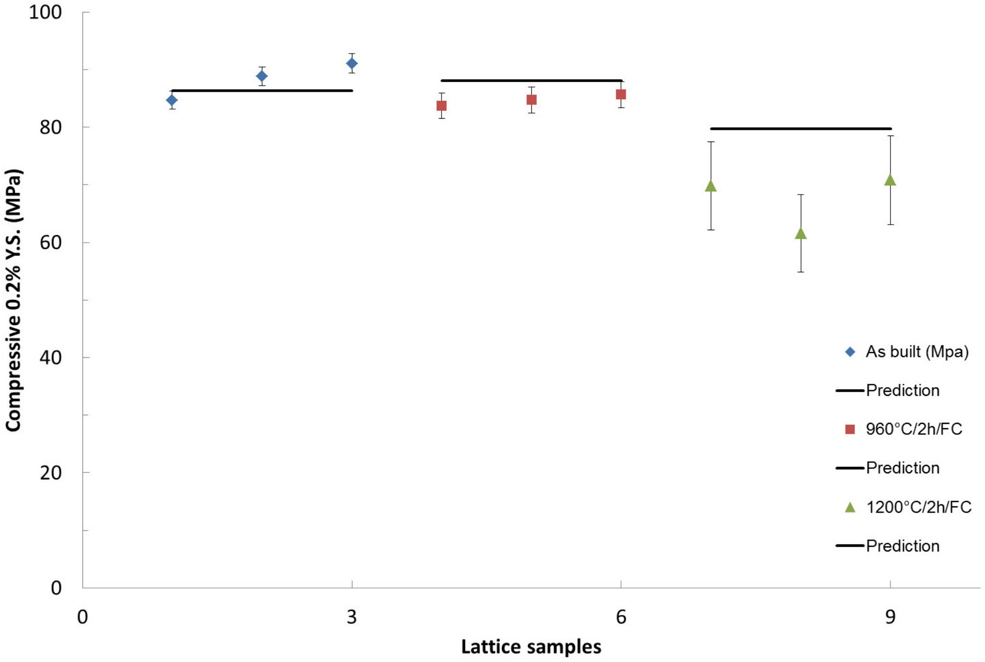

Figure 7.12: Experimental compressive yield strength values compared to predictions from parent material properties. "As built" samples falling within a 1.8% deviation, 9600°C/2h/FC samples within 2.7% deviation and 1200°C/2h/FC within 11% deviation.

7.4 Strut cross sectional area

In order to assess the geometrical fidelity of EBM and the manufactures lattices, the 7 single struts (named S1 to S7) previously CT scanned and mentioned in chapter 5, are commented for this chapter. The cross area range of these struts (0.45 to 2 mm) aims to complement the range of struts previously discussed (0.8-1.8 mm) to build up the cubic lattices. The results are summarised in table 7.3. These observations show that fine struts ≤ 0.6mm tend to be oversized while struts ≥ 1mm appear to be slight undersized (negative percentage). It should be pointed out that the set of single struts were processed using the same beam parameters as for the lattices, and same powder size particles. Therefore, this over/under sizing can be attributed to the way the "weldtrack" was accommodated when the contouring and hatching took place while varying the strut size.

Further refinements to the analytical predictions as fitting parameters need to be included in expressions of the type of equation 7.6. For the range of lattices discussed here, only relatively undersized features are obtained, see tables 7.1 and 7.3. Therefore, the overall plotted tendency in strength shown in figure 7.9 would be affected as $\sigma^* \approx \gamma C \sigma_s \rho_r$, where γ is the fitting parameter due to the area deviation.

For the specimens presenting oversized dimensions, a similar situation has been reported previously showing the EBM processing method to be incapable of reproducing fine features [144]. The parameters used in this process produce a weldtrack width large enough to cover areas up to 600μm with a single beam pass on solid *Ti-6Al-4V* substrates (see the single contour pass column in figure 7.14a). Figures 7.14b and c show redundant melting for full contouring and contouring plus hatching for areas of the same size. It is therefore expected that melting thin sections (with similar melt pool size and offset) out of the powder bed would pick up satellite particles around the periphery, oversizing areas above this value, see figure 7.14d. For undersized components however, the beam offset could be re-adjusted for accurate dimensions. However, the intrinsic pick up of particles around the edges of the solid may always be present causing deviations from the intended shape and size.

In order to control the dimensions of EBM sections, especially avoiding oversized thin sections, prior adjustments in power input can be applied. As mentioned in earlier, the Rosenthal model (see equation 2.1) can be used to predict the electron beam absorption of the material and therefore, the related dimension of the section to melt. For the beam parameters used in this process, a single beam pass performed on a pre-existing solid substrate agrees the experimental results with a depth-to-width ratio close to the ideal proposed by the model, see table 5.2. It is worth mentioning that despite the possible effects of focus offset and the electron beam efficiency [26], the power input could further be investigated to obtain lower penetrations and as a result allow the formation of thinner melted sections.

7.5 Internal defects and surface roughness

As mentioned in chapter 5, the manufacturing of these materials introduce a sensible fraction of internal porosity. While the previous chapter focused on the likelihood of volumetric defects as a whole within the solid mass, a more detailed analysis on defect distribution is shown in this chapter. Extracted data was rearranged as gradient dependent from the most outer and dense scanned region suggesting a distribution of defects in relation to the manufacturing scheme and its scan sequence [65]. This arises because the viscous forces within the liquid titanium trap pre-existing pores which arrange in patterns determined by the electron beam pattern. For each strut, the voids were quantified down the length of the strut and then projected onto a strut cross-section. This indicates that the voids are concentrated in rings (see insert in figure 7.13). Consequently the radial distance of the porosity is shown in figure 7.13 for the struts of different diameters. It is evident that the porosity appears to be concentrated at two distances; one approximately 50μm from the surface and another at 400μm in cases where the strut is sufficiently thick.

In order to interpret these results it is helpful to layout the scan schemes used to fill struts of different diameters (Figure 7.14). It is noteworthy that the porosity 50μm from the surface coincides with the offset from the CAD contour at which the hatching process was commenced, while the 400μm distance is approached by the thickness of a single weld track in this material. For the four most slender struts, the cross sectional area is not sufficient for a well-defined contouring region, figure 7.14b, whereas thicker struts allow the contouring and the hatching regions to be clearly distinguished, figure 7.14c.

On the other hand, the size deviations from the beam path across the random arrangement of powder particles and melting strategies, generates roughness. To report this evidence, Arithmetic average values (Ra) was obtained from the visualization analysis. It

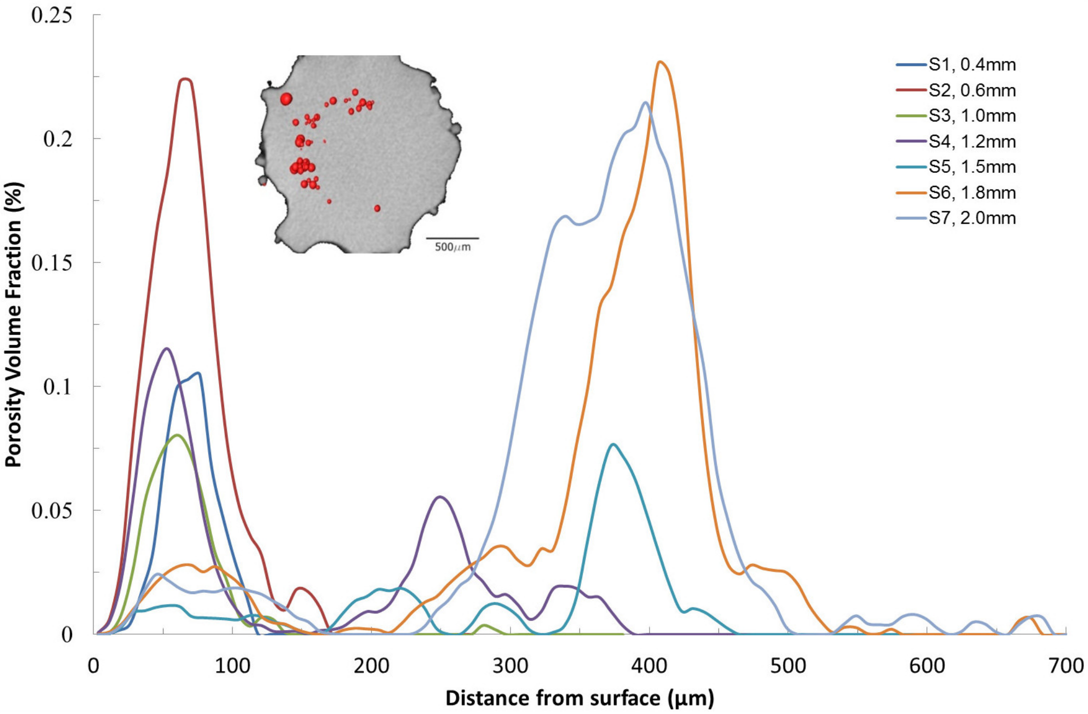

Figure 7.13: Porosity volume fraction with the distance from the outer contour for strut samples S1 to S7. Two main depths from contours can be appreciated at approximate 60 and 400μm.

can be seen that the roughness Ra is found in a range of $44 \pm 6.3\mu$m , which is close to the order of the smaller powder particle size. As mentioned earlier it is suggested that particles around the perimeter can be attached, leaving their trace on the surface defining the roughness. This effect can be compared with similar results published by Karlsson et al. [78] where two fractions of powder size were employed to melt components in EBM systems.

Table 7.3: Microstructural features and mechanical properties in lattice and tensile samples

sample	S1	S2	S3	S4	S5	S6	S7
STL diameter (mm)	0.4	0.6	1	1.2	1.5	1.8	2
Mean deviation cross Area (%)	52.9	18.5	-22.2	-18.0	-17.7	-15.5	-14.7
Ra (μm)	42.2	44.7	48.1	52.8	32.5	41.6	46.3

As part of the results it was shown that melted smaller particles create a roughness with higher average peak to valley ratio. It is perhaps surprising that the presence of these defects seems to have little influence on the lattice strength, with the experimental results in good agreement with the simple model prediction (which does not account for such defects). Of course failure as against the onset of yielding is much more likely to be sensitive to such defects and further research is needed both to improve dimensional accuracy (and models to account this for) but also to investigate the knock-down on ultimate properties due to such defects.

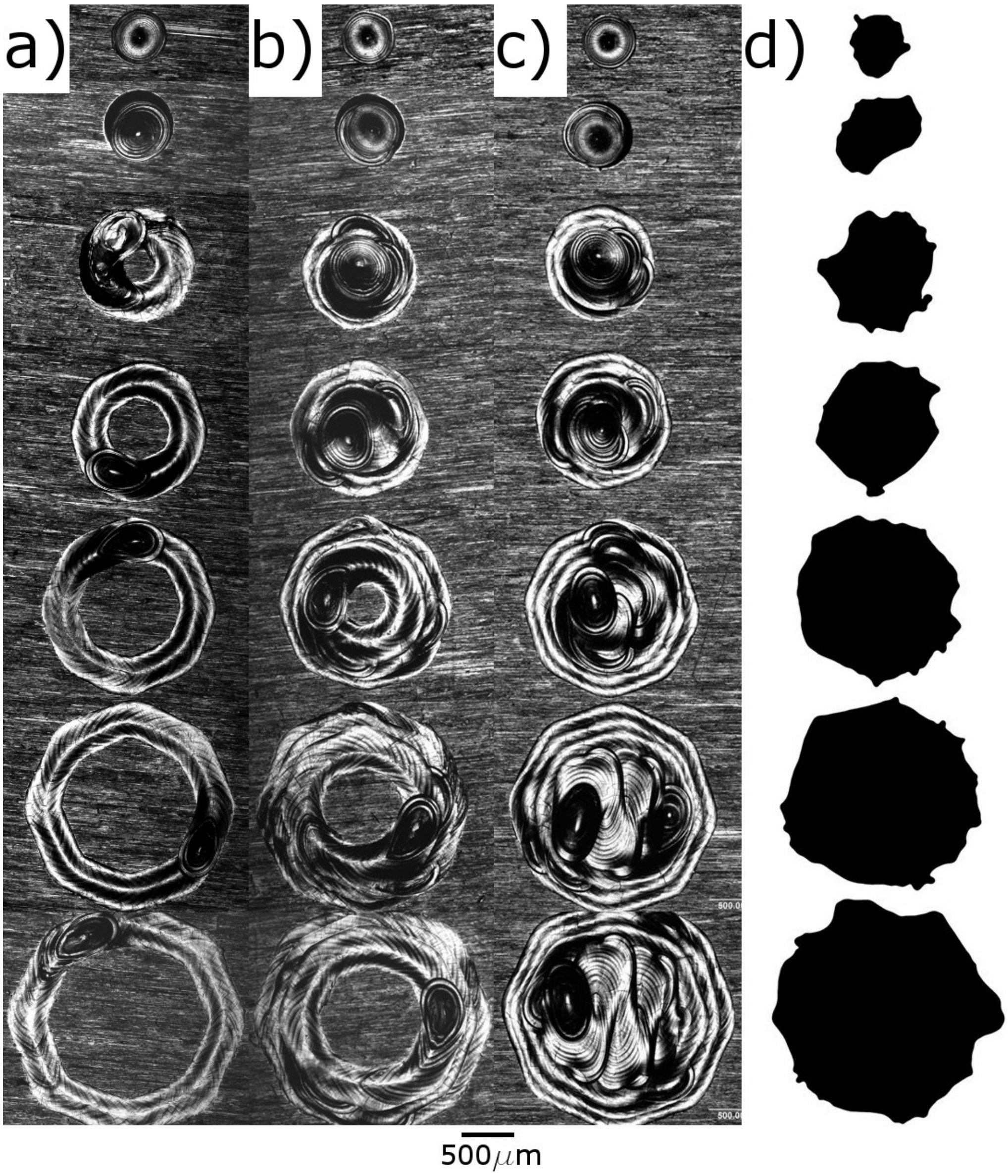

Figure 7.14: Comparison of melted zones with strut diameter. (a) Shows one contour and (b) the full contouring region. (c) Shows contouring plus hatching stages. (d) Illustrates the corresponding CT strut slice selected at a random height.

7.6 Deformation mode

The examination of fractured specimens under axial loading has uncovered the appearance of bands in the vicinity of the strut's fracture point. Such bands of deformation appear as white lines (see figure 7.15) previously reported in Ti-6Al-4V after intense deformation [145][146]. A closer view of the deformed zone, see figure 7.16, shows an intense deformation of the "as-built" microstructure, see figure 7.16a, b and c.

It is well known that upon intense plastic deformation an increase in temperature in the affected zone can appear in the material. This can become a sensitive issue if the material cannot dissipate the heat "efficiently" as the deformation progresses, creating *localisation* of the thermal energy. Depending on the material properties and deformation conditions i.e. thermal diffusivity and local strain rate, the dissipation of heat, if insufficient, can create an *instability* assisted by a *thermal softening* that usually ends in the material's fracture occasioned by the so-called *Adiabatic Shear Bands* (ASB) [147] extensively reported for Ti-6Al-4V [148][149][150]. In figure 7.15, shear bands can be distinguished along the fracture at an angle close to 45° from the loading direction. This falls in agreement to one of the requirements for localised deformation as planes of maximum shear stress are close to 45° [96] and localisation is one of the factors to develop ASB [151]. Up to this point however, it is not known which of the possible micro/macro structural features can develop the localisation of ASB along the strut lattice. Although it has been reported that the microstructure and mechanical properties influence the shear localisation [152], the feature effects of EBM material are desirable to be characterised.

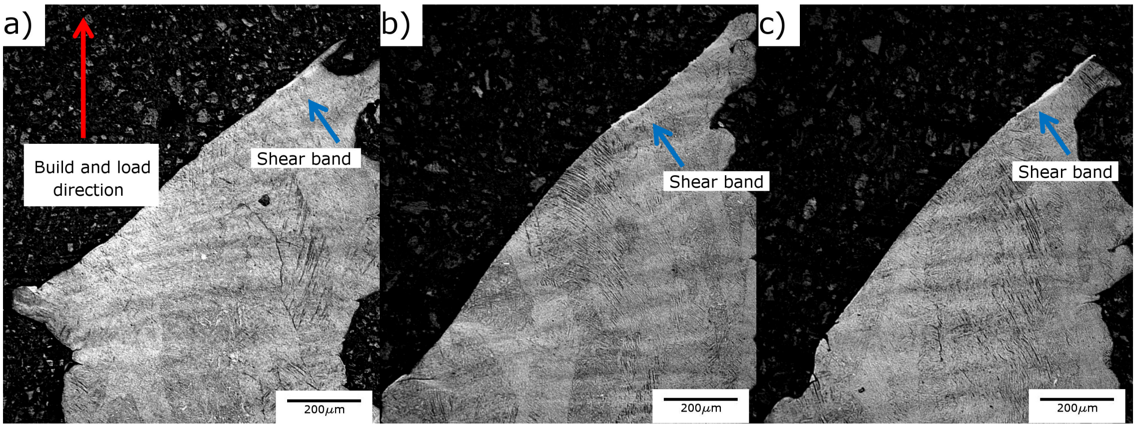

Figure 7.15: Appearance of shear bands in struts of a cubic lattice after being loaded axially.

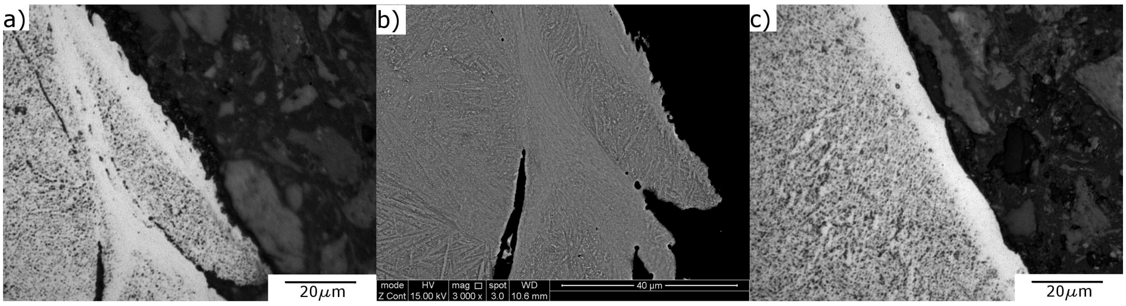

Figure 7.16: Magnification of the shear band zone in fractured struts of a cubic lattice after being loaded axially.

7.6.1 Systematic investigation of shear band thickness

Despite the clear appearance of ASB in deformed samples, a systematic investigation of their evolution in fractured struts is a difficult task. This is because the location of these narrow areas can become complicated, especially after high rates of deformation on elements of cellular solids. Therefore, in order to investigate their appearance and microstructural evolution, hat shaped specimens (see figure 7.17) were EBM manufactured to be further impacted and observed microscopically. Such specimens were initially proposed by Hartmann et al. for dense material samples [153], and were intended to be a controlled method to develop shear bands in between the punch section (r_1) and the hole base (r_2) of the hat specimen. Although provoked by edge effects, the development of the ASB can be gradually controlled through the shearing displacement [154][155][156].

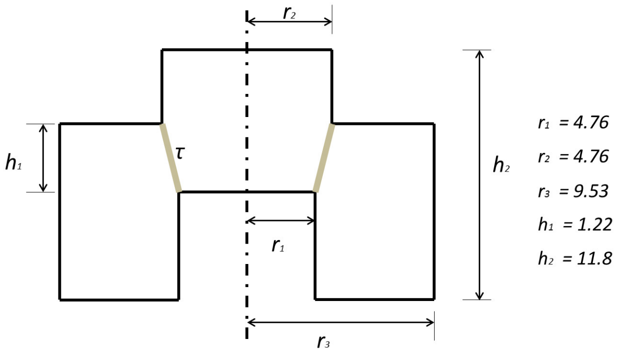

Figure 7.17: Schematic view of the hat specimen showing the key dimensions.

The analysis of a systematic shear evolution could be possible through the use of stopper rings to limit the axial displacement at a given speed of loading. The compression equipment employed was the Hopkinson Bar set-up described in section 4.4 with impacts of $\approx 26.5mm/s$ in speed and the axial displacements, allowed by the stopper rings, (see figure 7.18), reported in table 7.4. As mentioned previously, the set-up remained constant to reach similar impact speeds for all tests, that is keeping the pressure conditions of the gas gun constant. Taking into account the average impact speed mentioned earlier, the strain rate can therefore be calculated if the state of stress is assumed to be pure shear. This is done by dividing the velocity of the bar with the thickness of the plastic deformed region $\dot{\gamma} = \dot{v}/t$. The dimensions of the hat specimens indicate a very narrow shear section close to $\approx 230\mu m$ after the images from microscope observations, giving an approximate shear strain rate $\dot{\gamma}$ of the order of $\approx \times 10^5 s^{-1}$. The shear stress τ on the other hand can be calculated through the axial force and the surface of the shear region as $\tau = F_a/A_s$ where $A_s = \pi \times (r_1 + r_2) \times h$. The axial force F_a itself can be calculated from load equilibrium

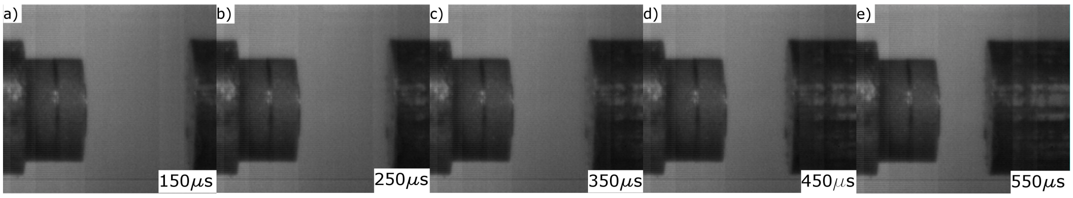

Figure 7.18: High speed camera shots indicating the accelerating time prior the impact by the bar(right side) to the hat specimen (shown in the left side).

at the impact as:

$$\sigma = E\epsilon_t \tag{7.7}$$

$$\frac{F_a}{A_a} = E \times \epsilon_t \tag{7.8}$$

where σ is the axial stress from the impact, E is the Young's modulus of the striker bar and ϵ_t is the strain pulse recorded. This is valid if the impact from the Hopkinson bar is not so intense to cause plastic deformation on the HB to lead to dispersion in the frequency. The shear strain γ on the other hand is obtained by dividing the displacement by the thickness of the sheared area $\gamma = \delta/t$, shown in table 7.4.

Table 7.4: Test conditions and results form the impacted hat shaped specimens with an impact speed of $\approx 26.5m/s$. † The deformed area found in sample A seems unclear to be ASB.

Specimen	Displacement (mm)	Shear strain ($\dot{\gamma}$)	ASB thickness (μm)
A	0.08	0.34	6.6†
B	0.25	1.08	8.2
C	0.44	1.91	9.76
D	0.64	2.78	13.6
E	0.97	4.21	15.9
F	1.06	4.60	16.5

7.6.2 Localisation from testing

The characterisation under impact velocities of the hat shaped specimens was plotted in figure 7.19. All samples left a voltage trace recorded from the gauge. Although this was not converted to strain transmitted ϵ_t due to lack of data, it is known that the output voltage scales linearly, see equation 4.1. It can be seen that a maximum in the recorded from the gauge is obtained for all samples (except sample A) for displacements close to $0.2mm$. This displacement can be seen as the onset of localization indicating the drop in load by the hat specimen (sample A was not allowed to go to this stage of the test), see table 7.4. All samples show similar voltage levels at the onset of localisation.

It can also be seen that the curves of samples E and F show a second drop on what seems to be a secondary localisation stage, also these two samples shown more extensive displacement when deformed. This behaviour can be explained as an imperfect contact between the samples surface and the surface of the striker bar, causing a localisation in stages when the fracture occurred. However, as these results appear at the end of the spectrum studied here, is it highly desirable to extend the range of deformations in order to assess reproducibility. Previous studies [151] have reported oscillations at displacements of $1.5mm$ at impact speeds of $8m/s$ and taking the midpoint as a reference. Here in this work as the mid point is well below the voltage scale referred to a load, it is believed the localisation was not homogeneous.

7.6.3 Shearing zones

The observation of the shear bands was carried out using OM and SEM, showing the specimen B (the sample with minimum displacement and localisation from impact) an example in figure 7.20 where the crack is pictured along the sheared zone. The transition

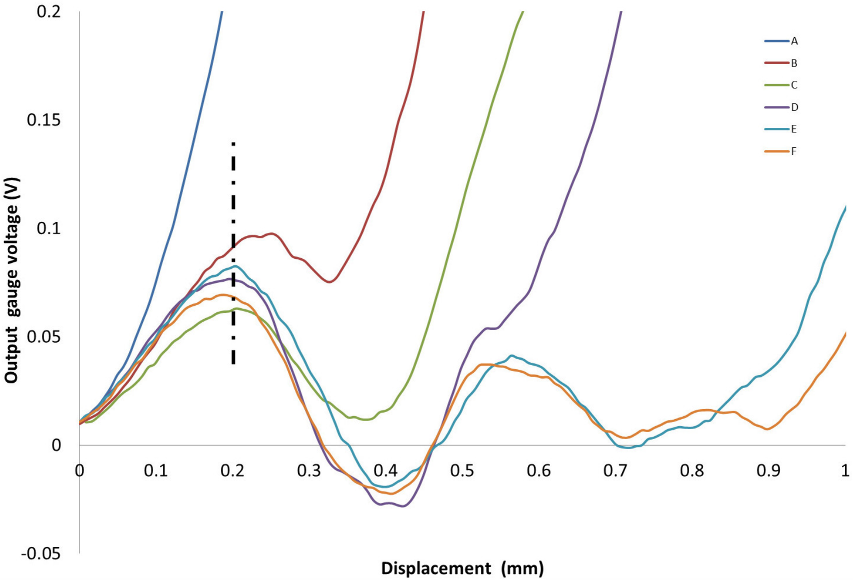

Figure 7.19: Output voltage gauge signal with displacement converted from the speed recorded out of the camera. The curves show a maximum for samples B to F close to 0.2 mm, indicating the onset of localisation.

from the matrix to the deformed material can be observed in figure 7.20b where bending of α laths can be seen at the limits of the shear band. An additional magnification within the shear band is shown with no trace of the lamellar microstructure, figure 7.20c. The thickness of each band, see figure 7.22, was plotted for all the displacements shown in figure 7.21. As can be seen, the developed shear strain γ at different displacements caused a variation in shear stress that developed a linear behaviour in ASB thickness with a range of 8 to 16 μm for samples B to F.

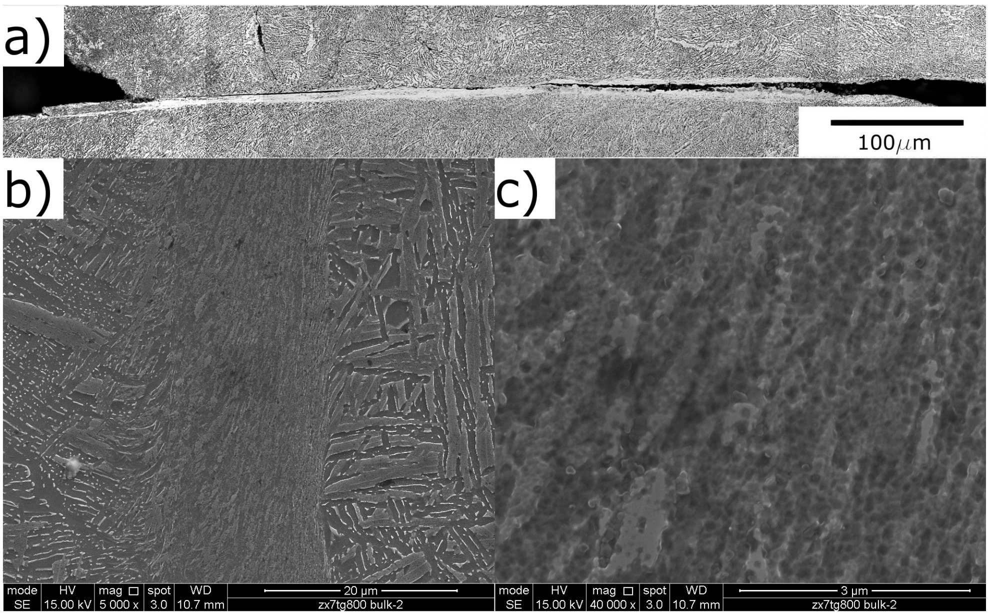

Figure 7.20: (a) Adiabatic shear band developed after the compression of the hat specimen where the shearing zone can be appreciate along the failure.(b) the deformed zone in between the lamellar $\alpha + \beta$ matrix. (c) shows the deformed zone at higher magnifications.

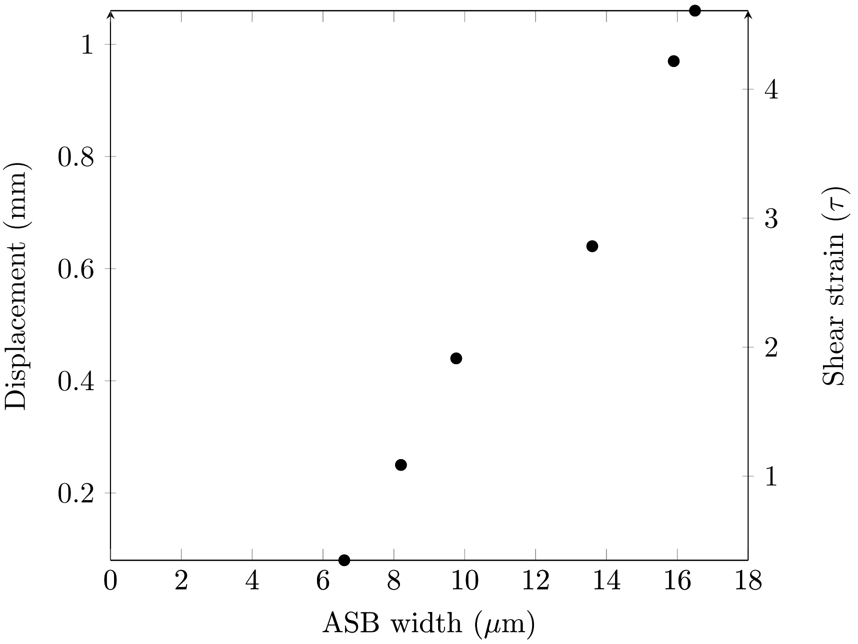

Figure 7.21: Thickness of the adiabatic shear band with axial displacement from impact.

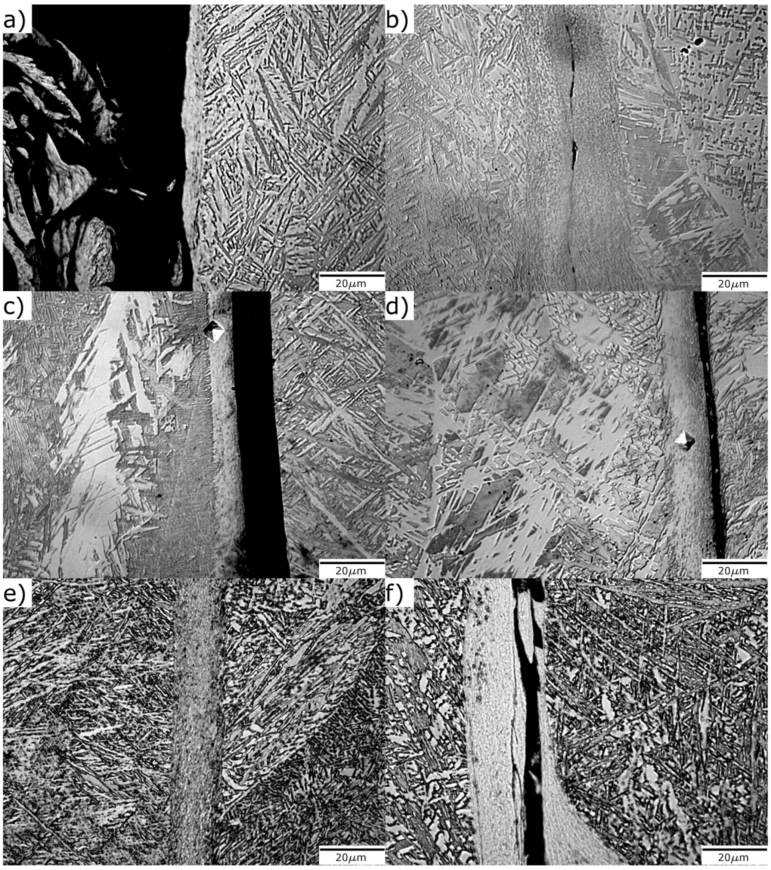

Figure 7.22: Adiabatic shear bands found in the hat specimens. (a) The only specimen with a non-homogeneous shear band in agreement with the lack of localisation in the impact curve, (b to f) show well delimited shear bands within the $\alpha + \beta$ microstructure.

Vickers hardness measurements were taken using a load of 0.01 kg and reported in single lines in order to compare the equidistant microstructural softening from the band, see figure 7.23 corresponding to specimen F mentioned in table 7.4. From this figure it can be seen that a maximum in resistance to indentation was developed although, not at significant levels as the non-deformed matrix.

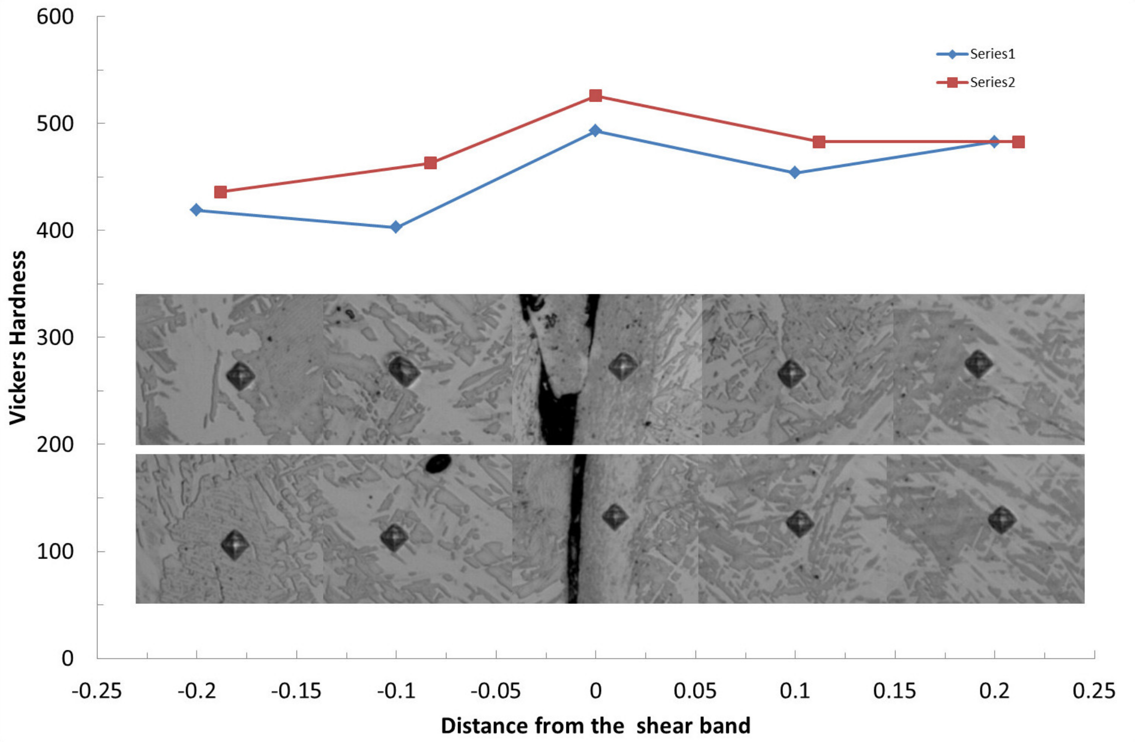

Figure 7.23: Single line Vickers hardness measurements. A lower indentation resistance can be seen as the distance form the shear band increases.

7.6.4 Microstructural evolution

The evolution of shear bands has been studied previously in α titanium by Meyers et al.[151], based on regions observed using TEM and analytical models. As a result, a process of elongation, deformation of grains and transformation into sub-grains with the development of high density regions of dislocations was reported. The microstructural aspects of shear localisation however, are extensive and need to be carefully reviewed. As an example, transformation in Ti-6Al-4V of coherent products Ti_3Al [157] and the co-existence of crystalline to amorphous states during dynamic deformation has been reported [158]. Although it is known that damage and fracture is caused by the coalescence of voids and micro-cracks (rather than the appearance of ASB) that propagate along the band and not into the material because of its higher yield strength. The propagation speed is reported to be up to $\approx 500m/s$ however, it is the external velocity of the deformation that determines it [159].

Here in this investigation, the final microstructure within the band and in the vicinity could only be assessed by hardness measurements reporting similar levels of strength for both regions. This can therefore be attributed to results of the work hardening and the ultra-fine grain structure within the shear band however, its microstructural evolution and propagation to determine the failure in lattice struts needs further characterisation.

7.7 Chapter conclusions

Electron Beam Melting (EBM) and CAD tools have successfully been applied to fabricate lattice structures using *Ti-6Al-4V* prealloyed powder. Due to the increasing interest in this type of material processed by AM, the effect of defects on the structural performance needs to be assessed. Even though the range and type of defects can vary widely, here in this chapter the influence of variation in parent material properties alongside certain volumetric defects were found and highlighted.

To validate such defect fraction in lattice elements, a systematic study on lattice compressive strength in function of density was carried out and analysed. Such response could successfully be predicted by analytical approaches derived from simplified descriptions of how the load is supported. The influence of parent material properties, included in the analysis, predicted the compressive performance under 2.7% deviation for samples heat treated below the $\beta - transus$ temperature with furnace cooling and a 11% mismatch for heat treatments above the $\beta - transus$ temperature with furnace cooling.

Intrinsic AM defects were seen, consisting of well-defined porosity patterns, surface roughness and dimensional mismatch. While the porosity patterns arise from porosity in the raw materials rearranged by the material deposition strategies, the dimensions mismatch was suggested to be strongly related to the energy absorbed by the powder particles and the electron beam resolution. As the minimum weldtrack width optically identified was close to 300μm, this produced oversized small features (as the case for struts of 0.4 and 0.6 mm) with an area deviation up to 52%. Raw materials and deposition strategies are suggested to be further investigated. Surface roughness is significant, yet, even in combination with the defects mentioned earlier, it seems not to play a significant role compared with the bulk properties in the mechanical response of cubic lattices loaded axially.

The failure mode identified in this geometry was found to be related to the development of Adiabatic Shear Bands. This was suggested to be due to areas under maximum shearing stresses developing thermal softening and facilitating the fracture. Although further study of the evolution of such bands is required, the preliminary results show that the shear stress from impact speeds linearly increases the thickness of the bands for the range studied.

8

Defect population and applications of EBM-processed TI lattices

The search for structural materials capable of showing suitable properties in fields of biomaterials, ballistics and body armour, aerospace as sandwich panels or light structures, etc., has been an extensive one, which has frequently involved exploration of lattices [43][99]. As an example, diamond-type lattices have been object of a variety of studies either focused on biomedical implants as a facilitator of tissue ingrowth [87], as a structure capable of spreading impact loading spatially and temporally [104], as part of meta-material concepts [160], with a co-linear and waviness in their truss elements [161] and composed of membrane systems as honeycomb structures [162] for quasi-static studies. Although with structural variations in the geometries, these studies can be seen as an effort to establish the structural capabilities of lattices under various conditions and environments. As an effort to clarify issues related to the structural response for the diamond lattices, this chapter comments not only mechanical properties but also the issues related on achieving as-designed shape. The methodology followed the exploration of relative density (batch 1) and sample aspect ratio (batches 2 and 3), tested under quasi-static conditions. Specimens of batches 1 and 3 were manufactured consecutively and, batch 2 corresponded to a single EBM build in order to avoid differences in raw materials chemistry arising from the reuse of powder. Differences in strength from exact solutions are noted however, as these models do not take into account the influence the lack of mass (internal porosity) therefore the models are left in terms of relative density values. Internal porosity within different geometries are also reported out of CT scans. A combination of the

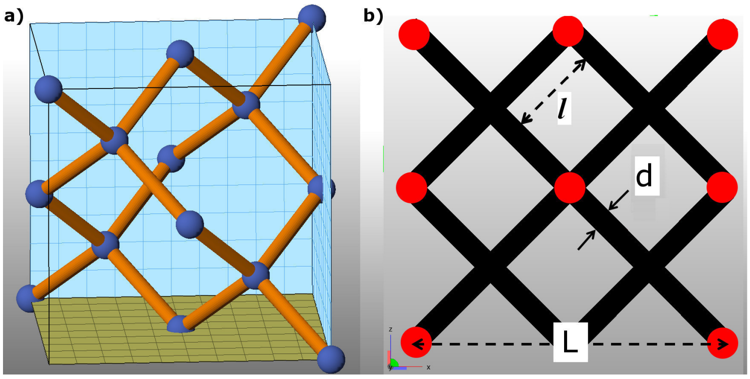

Figure 8.1: Schematic figure of a diamond-like geometry where the carbon atomic positions represent the nodes. (a) a perspective view, (b) a front view

conditions used for fabrication (the melting sequence, beam energy and the raw material) produced distinctive patterns for each topology. The results suggest that a high fraction of pores (irregular in shape) tend to appear in areas where the melting is compromised i.e. at nodes of high connectivity or trusses built perpendicularly to the built direction. On the other hand, if the strut is closely aligned to the build direction, the fraction of porosity appears to be much lower. In addition, data from impact tests is briefly included highlighting the importance of increased strength at high strain rates. In order to assess the capabilities of cellular solids (including diamond lattices), a comparison in terms of relative density for all the geometries studied in this investigation is briefly reported.

8.1 True density and the problem with design

The designed relative density of diamond lattices was calculated as the ratio of the solid material and the unit cell volume, see formula 8.1. Here γ is the angle between the strut (of length l and diameter d) and the xy plane (being 35.25° in the present case, see figure 8.1). Therefore, the volume L^3 and a unit cell length of $L = (2\sqrt{2}) l cos\gamma = l4\sqrt{3}/3$ gives a relative density of:

$$\rho_r = \frac{V_s}{V_u} = \frac{4\Pi l d^2}{L^3} = \frac{3\sqrt{3}\pi}{4^2}\left[\frac{d}{l}\right]^2 = \frac{2\Pi}{\sqrt{2}\cos\gamma}\left[\frac{d}{L}\right]^2 \tag{8.1}$$

This equation can either be in terms of strut length "l" or in terms of the unit cell length "L" for convenience in the STL design. However, it should be noted that equation 8.1 is derived after assuming ideal conditions of full node-to-node length and rounded strut section profile for the strut length and diameter respectively. This may introduce deviations in the predictions from the initial assumptions as double corner counting and other inherent issues raised by the process such as irregular strut cross sectional areas and internal porosity. While there are alternative methods to determine virtually the volume fraction, that is by applying boolean operations eliminating internal surfaces (requiring extra computational power), the analytical determination of the volume fraction requires knowledge of real dimensions achieved in the process. Four cases of relative density are analysed in table 8.1, ideally circular, boolean (based on one single unit cell and 100 triangles defining the rounded area), analytical adjusted or semi experimental (ideal with adjusted diameter) and experimental.

Table 8.1: Lattice diamond features of unit cell size, virtual strut diameter ϕ, scanned strut diameter ϕ_{CT}, ideal analytical, boolean, adjusted (with CT mean diameter) and experimental relative density.

U	ϕ	ϕ_{CT}	Ideal analytical	Boolean	Analytical adjusted	Experimental
(mm)	(mm)	(mm)	ρ_r	ρ_r	ρ_{r-ad}	ρ_r
10	0.5	–	0.013	0.013	–	0.020 ± 0.0002
10	1	0.88	0.054	0.051	0.45	0.044 ± 0.0005
8	1.3	–	0.143	0.132	–	0.106 ± 0.0009
8	1.8	1.65	0.275	0.244	0.231	0.184 ± 0.0050
5	0.8	–	0.139	0.128	–	0.111 ± 0.0010
5	1.3	–	0.367	0.320	–	0.240 ± 0.0008

As can be seen from table 8.1 an experimental deviation is found as the samples increase with the exception of the lowest value. The later can be related to the chosen melting strategy and the over-sizing issues commented in chapter 6 and not to analytical calculations. For the opposite tendency, a further assumption is therefore required to obtain a better analytical approximation. This can be approached by restricting a “rounded” strut cross section to a finite number of sides in order to approach real conditions. However, as reported in chapter 6, the strut profiles can be highly irregular and not easily related to a polygon making it difficult to analyse. For the following analysis, a squared cross section is employed in order to estimate the influence of the strut diameter profile and double counting corners.

By assuming a squared truss member, the volume of intersection V_I between two trusses meeting in each node at 109.5°, (see figure 8.2), that is $\gamma = 35.25°$ each truss from the horizontal plane is found to be:

$$V_I = \left[\frac{1}{2} + \frac{\sqrt{2}-1}{2} + (2-\sqrt{2})(1-X_1^2)^{\frac{1}{2}} X_1\right]\frac{t^3}{4} \tag{8.2}$$

where $X_1 = (sec\gamma - tan\gamma)$. As the intersection is repeated creating a tetra-intersection each node V_{TI} of width same as the thickness, see figure 8.2, the total intersecting volume is:

$$V_{TI} = \left[...\right]\frac{t^3}{2} \tag{8.3}$$

This analytical approximation can therefore be used to determine a fitting parameter between the analytical (ρ_A) and the experimental values (ρ_{exp}) in the form of $\rho_A = C_x \cdot \rho_{exp}$, giving an arithmetic mean value $\approx 0.82 \pm 0.06$. This corrected analytical approach is plotted in figure 8.3 along with the ideal equation 8.1, the boolean operation and the experimental values in terms of the node length-profile diameter ratio. From figure 8.3 it can be seen that the ideal asymptotic curve is approached closely by the boolean operations. However, this approach is difficult for lattices of high volume and requires large computational power as mentioned earlier.

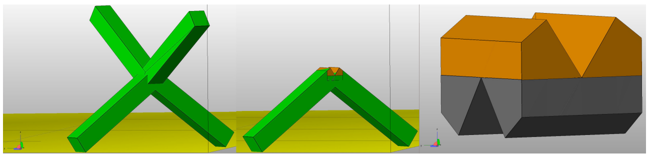

Figure 8.2: Schematic figure showing the trusses meeting at a node showing the top and lower part of the magnified intersection.

For analytical purposes, the experimental values can be predicted closely by taking into account the corner double counting and constant strut cross section, even at high relative densities. However, this approach can only be referred as indication of the intersecting volume and should not be considered as a real measure of this value. A further analytical approach may be possible by assuming different cross areas depending on the CAD-STL exporting practices [38]. These offset values for triangle tessellations are applied to constrain the shape models, see figure 8.4 however, it may depend on the resolution from the process, CAD-STL tolerance offset and the designed cross section. Finally, it is worth noting that a lack of solid volume may occur as part of the manufacturing process. As discussed earlier, internal porosity is a common issue found in materials manufactured

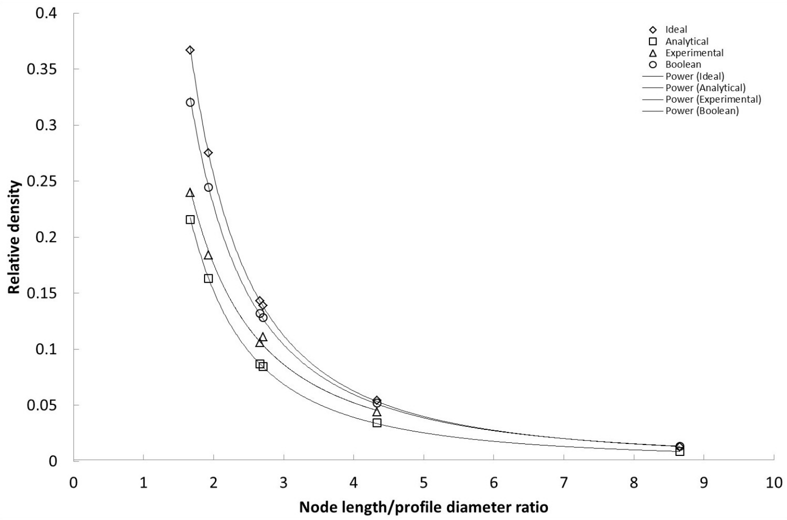

Figure 8.3: Relative density curves for diamond lattices in terms of node length-profile diameter ratio based on ideal circular cross section, boolean operations, analytical squared cross section and experimental values.

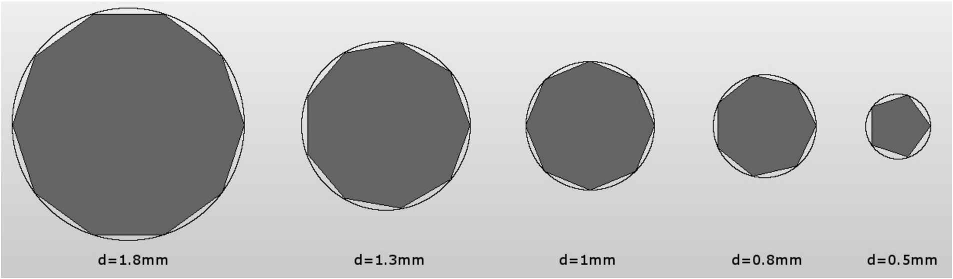

Figure 8.4: Schematic triangle tessellation with an offset of $40\mu m$, this value represents the smaller size of a powder particle and the approximated surface roughness found in these materials. The trace of an ideal circular shape for all truss diamond lattices diameters is also shown.

additively. The contribution to differences in volume from such defects is not taken into account for this set of results, however, this is further explored at the end of this chapter.

8.2 Compressive strength of diamond-like structures

Following the same approach used in chapter 6 and 7, the Young's modulus was obtained from the linear part of the stress-strain curve. Also the failure strength was taken as the 0.2% offset from the linear part, all values are plotted in figure 8.5. The variation in strength with density reported an increasing resistance which was fitted by power law of 1.9 according the least square method. In a similar fashion, an exponent of 1.8 for maximum strength and Young's modulus was found.

8.2.1 Mechanical properties

As discussed earlier in chapter 3, the analytical relationships for diamond-like lattice structures 3.12, 3.15 and 3.16 have been reported in previous literature [17]. These relationships are plotted in figure 8.5 along the experimental results for the range of density explored here. While Timoshenko's theory predicts a better match with experimental results particularly at high densities, Euler-Bernoulli over estimates the elastic properties. This is due

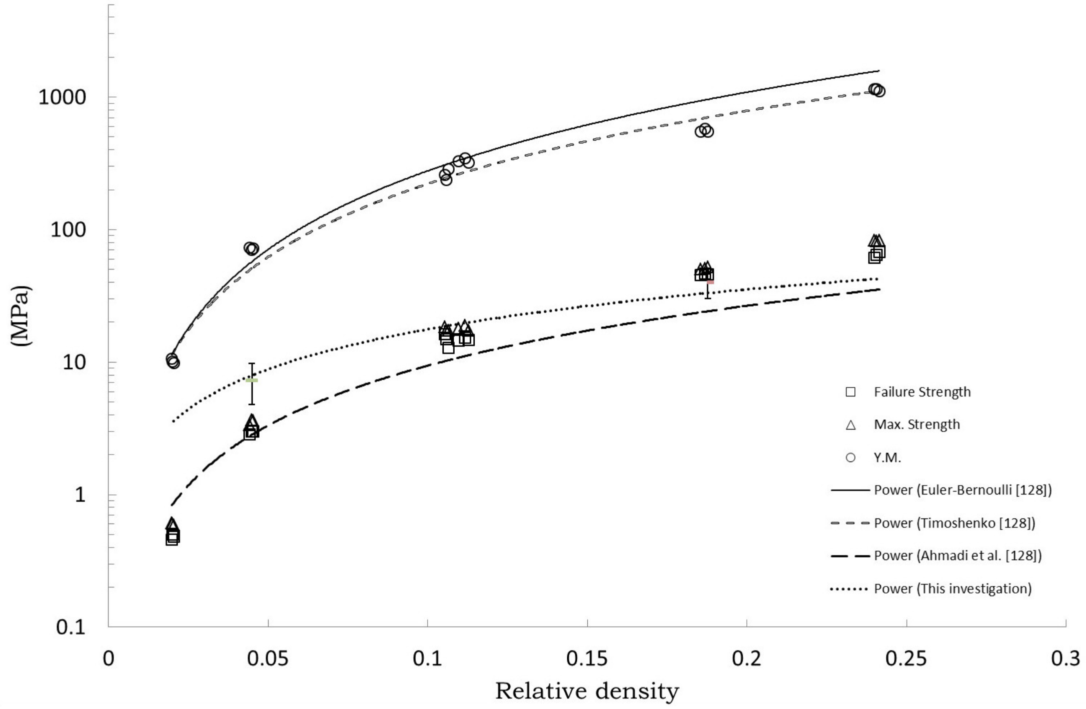

Figure 8.5: Mechanical properties of a diamond lattice under compressive loading with variation in relative density.

to the shearing forces and rotational inertia effects that Timoshenko's theory takes into account and may be present at the truss nodes especially at high density. In the case for low density lattices, the Euler-Bernoulli derivation with and without axial stresses taken into account (equations 3.12 3.13) gives a better prediction.

The equation for the plateau stress, in a similar fashion, overpredicts the failure resistance at low densities and under predicts for the extremes of the density range. Good agreement is found for relative densities up to 0.05. This makes it worthwhile to recall that equation 3.16 has been derived taking only the bending moment into account therefore, its asserted prediction coincides with the case for elastic properties using Euler-Bernoulli theory for low density values. A different approach to derive an equation able to predict

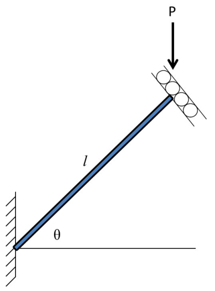

Figure 8.6: Diagram of a uniaxial loaded beam element.

a closer value at high densities was developed by assuming the diamond lattice as an arrangement of co-linear trusses at an angle of $\theta = 45°$, the projection of the XZ plane is shown in figure 8.1b. Assuming conditions of a fixed cantilever at one end and free rotation on the opposite side, see figure 8.6, the load P in the y direction is $Psin\gamma$. The stress caused purely by axial forces on a truss element of circular shape is therefore:

$$\sigma_a = \frac{4Psin\theta}{\pi d^2} \tag{8.4}$$

Hence, the exerted compressive load on the lattice is $A_{uc}\sigma^* = P^*$, where A_{uc} is the cross sectional area of the unit cell and σ^* the failure stress. Hence, when the critical yield force of the material P^* matches the failure force of the material P, the collapse stress can be determined. This is assumed to be after the two forces are in equilibrium by axial stresses σ_a only, giving the equation 8.5:

$$\frac{\sigma^*}{\sigma_a} = \frac{3\pi}{32\sqrt{2}}\left(\frac{d^2}{l^2}\right) = \frac{\rho_r}{2\sqrt{6}} \tag{8.5}$$

where l is the truss length and d the diameter, θ and γ the angles defined previously. A comparison for lattice strength between the two models, Ahmadi et al.[17] and that developed in this investigation (equation 8.5) can be seen in figure 8.5. It can be observed that while Ahmadi's formulation for plastic resistance [17] tends to underestimate the geometry at high densities ($\rho > 0.1$), the formulation developed in this investigation gives a better fit, although the value is still under predicted. In order to approach the experimental response, the added error bars show the standard deviation of the lattice strut diameter reported in table 8.1. This variation suggests that as the yielding may take place at an early stage in the thinner section of the truss, collapsing the lattice prematurely. As a result, it can be concluded that early stages of yielding of the bulk material can be related to failure stresses for the lattice to obtain the collapse strength. By doing this for specimens with high densities (0.18 and more), the failure stress is better predicted from the equilibrium of axial forces only.

8.2.2 Effect of specimen size

An additional response found in diamond samples was obtained after the compression of samples with an aspect ratio of 1 and different number of unit cells, the response is plotted in figure 8.7. It can be seen that a semi-linear trend in both plastic and elastic properties is found. For the density explored, an average value in failure stress of $\sigma^* = 27.8 \pm 2MPa$, a maximum stress value of $\sigma_{max} = 36.9 \pm 2.8MPa$ and a Young's modulus of $E^* = 614.03 \pm 55.2MPa$ are found. The predictions of analytical relationships mentioned earlier [17] and equation 8.5 have been added for comparison. It can be seen that the aspect ratio of 1 showed a slight variation in Young's modulus for the range of unit cell numbers tested here. Despite this variation its lowest value was found at a minimum number of unit cells. A similar case was found for the failure and maximum strength. Overall, the analytical expressions based on Euler-bernoulli theory [17] showed a better agreement with the elastic behaviour. In the case of plastic response, Amadhi's equation [17] underestimates the failure strength by almost half of the maximum strength. The failure stress of equation 8.5 on the other hand, gives a better approximation to the values obtained here. This closer prediction is based on the average diameter reported from XCT scans (undersized area) and seems to be in agreement to the assumptions of truss yielding on the thinnest part of the solid body mentioned earlier.

8.2.3 Effect of sample aspect ratio, $L/H \geq 1$

The mechanical properties obtained by compressive loading in lattices of ratios $L/H \geq 1$ is plotted in figure 8.8. As part of the properties reported in this section, it can be seen that

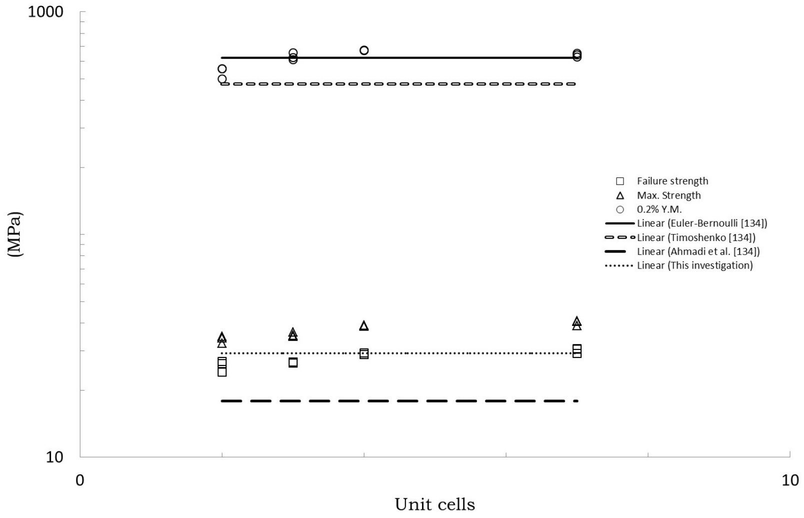

Figure 8.7: Mechanical properties of diamond lattice samples of aspect ratio of 1 and relative density of 0.15.

while the maximum stress (36 ± 2.6MPa) remains close to the values previously reported for the same relative density samples (shown in figure 8.7) the failure stress is increased reporting a mean value of 30 ± 2.6MPa. This can be seen as part of the increase in axial stresses that samples with high aspect ratio may be developing upon loading. Additionally, a more changing elastic response can be seen for all samples when the Young's modulus is plotted. Least square regression reports a fit with an exponent of $-0.44 \approx -\frac{1}{2}$. Despite this sample shape dependence of properties, with similar specimen/testing conditions of strain rate and relative density, a few highlights can be observed. First, at constant x and y length, the Y.M decreased linearly. The effect of width with length "L" can not be clearly established as the number of samples was not sufficient although, the "arbitrary" selection in coordinates for the width shows a decrease in Y.M. as the L/H ratio increases. It is therefore assumed that different models need to be applied taking into account the changing fraction of axial and bending forces that may act. This is concluded after the trend in Young's modulus could not be predicted by the analytical models [17].

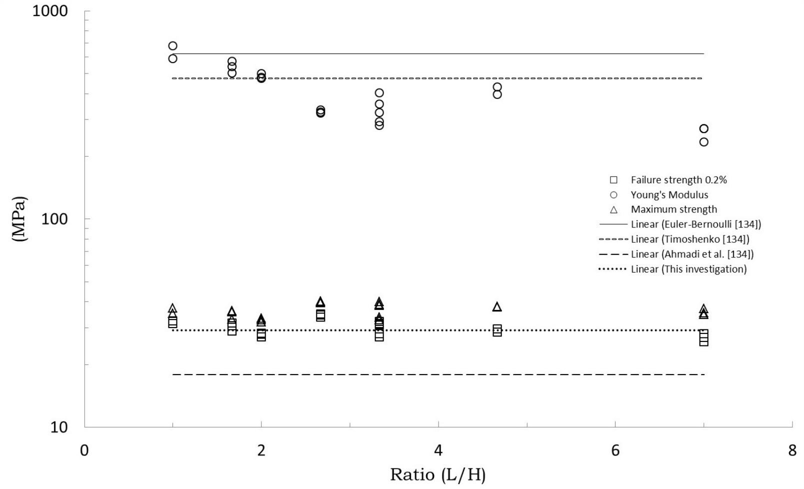

Figure 8.8: Mechanical properties of diamond lattice samples of aspect ratio $L/H > 1$ and relative density of 0.15.

8.3 Truss element orientation and the problem with manufacturing

It is well known that EBM parts are far from being defect free, as internal porosity (among other defects) are present [65]. The significant fractions of internal pores which are reported, derive mainly from pre-existing porosity in the feedstock, which can not escape at the melting range of energy density. This is claimed to be due to the liquid metal forces that restrict the escape of gas bubbles. Instead, the voids that are present are re-arranged onto patterns that appear to correlate with the electron beam path [163].

Non-optimum beam energy densities can also generate defects due to lack of fusion[65]. Contrary to defects coming from the feedstock, these appear as irregular in shape and larger than the particle size where traces of poor adhesion of new particles can sometimes be seen. Although this type of internal discontinuity can appear due to several factors, all can be related to non-optimum melting heat or unfavourable thermal variations.

Traditionally, the EBM process applies preheating stages (termed preheat I and II in the equipment) so when the melting step takes place, the powder particles should display a gradual liquid-solid transformation so that they are easily incorporated to the solid body minimising such lack-of-fusion defects. In practice however, this is usually not the case as factors affecting the adhesion of particles may appear (wetting and oxidation effects [41]) resulting in the formation of pores and “tunnels” [164]. In complex structures such as lattices, it can be expected that variations in heat may cause a significant fraction of defects, especially in thin sections of materials. Their continuously changing geometry (see figure 8.9) increases the risk of generating defects, as melting takes place over solidified and loose particles. This in turn may need optimised preheating strategies to be well developed prior to fabrication of defect-free lattice materials.

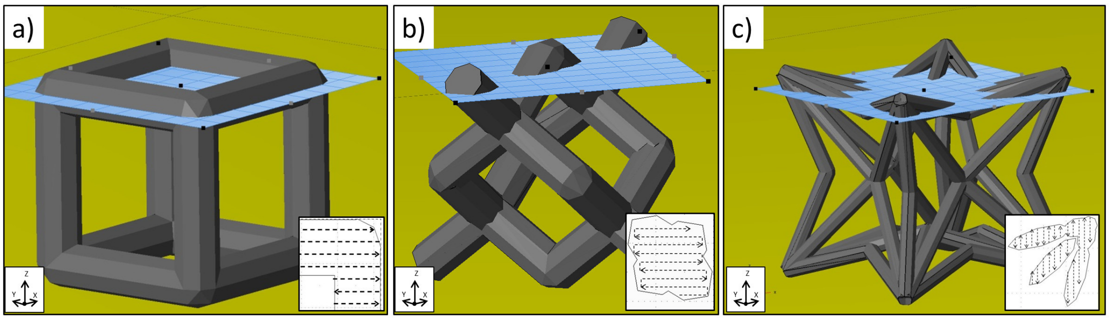

Figure 8.9: Schematic view of the three lattices at different heights of (a) cubic, (b) diamond-like and (c) re-entrant cube. Inserts on the node connectivity are highlighted.

In order to assess the appearance of defects with EBM build orientation and geometry, CT-tomography scans were carried out on three different topologies used here; diamond, cubic, and re-entrant cubic lattice. All three geometries were built with one lateral face laid on the start plate. The cubic and diamond topology (figure 8.10a and 8.10b) resemble the same conditions analysed earlier, while the re-entrant cube is a variant of the auxetic cube structure proposed by Lakes [165] with no lateral truss members, see figure 8.10c. The visualisation method reported the pore volume fraction analysed splitting the structure into planes one voxel thick along three orthogonal directions, see figure 8.11. As can be seen from figure 8.11a, the individual pore volume distribution in a diamond lattice

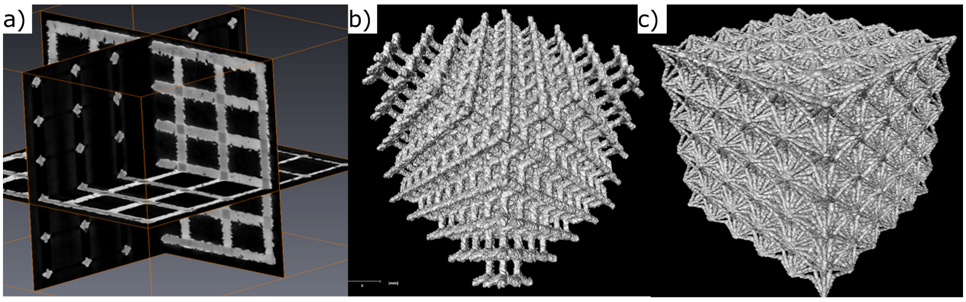

Figure 8.10: Scanned geometry of (a) cubic, (b) diamond, (c) re-entrant cube.

appears fairly constant across each of the 3 spatial dimensions. This suggests that the build conditions are equally likely to result in pores being positioned throughout the lattice, with no regions (on the macroscopic scale of the structure at least) where porosity is more likely to occur than others. In addition to this, the absolute level of porosity (not exceeding 0.03% of the solid volume in any measured slice) is low within the solid struts of the diamond structure. In contrast, the porosity distribution found for the cubic lattice, figure 8.11b, shows relatively higher levels of porosity. As can be seen, peaks showing higher volumetric fractions are often distributed in all the orthogonal reconstructed scanned directions. As the cubic lattice was built so that their truss elements were either parallel or perpendicular to the build direction, the material response may not have been equally when adding melted material on new layers of powder as in pre-existing solidified. This in turn leaves a bigger chance to create discontinuities within the solid. Previous studies reporting internal porosity in trusses built fully parallel to the build direction (so that new solidified material was always added over pre-existing one) show similar levels of porosity as those found in the diamond-like lattice [97]. It can therefore be suggested that the used beam power (same for both investigation cases) leaves almost identical fractions of porosity in both orientations. On the contrary, when there is a combination of parallel and perpendicular elements to melt as in the cubic lattice, the volumetric porosity fraction increases significantly.

For the re-entrant cubic lattice, figure 8.11c shows porosity periodically distributed, in a manner that coincides with the spacing of the nodes of high connectivity found in the lattice. This suggests that highly populated areas within the designed structure (i.e. areas where multiple struts meet) can represent difficult sections to melt, particularly for small size specimens. Although it is not clear up to what point the orientation in addition to highly populated areas influences the fraction of porosity, their irregular pores shapes and its formation in “colonies”, (see figure 8.11) may be an indicative of lack of fusion and not to pre-existing pores within the feedstock. It is therefore suggested that; given the fact that some porosity may exist, a high fraction of pores (irregular in shape) is likely to appear in areas where the melting is compromised i.e. at nodes of high connectivity and or trusses built perpendicularly to the built direction. On the other hand, if the member is built close to the built direction, the porosity fraction seems to diminish. In regard to the pore size, figure 8.12 reports the number of pores with size found for the three geometries. It can be seen that the number of pores found in the diamond lattice is significantly lower than the other two lattices where a higher pore volume fraction (up to one order of magnitude) was reported. However a significant difference can be distinguished between the two cubic geometries, while the diamond concentrates its distribution at bigger pore sizes, the re-entrant one contains a much smaller void population. This supports as well the fact that electron beam struggles to melt areas perpendicular to the built direction with no support

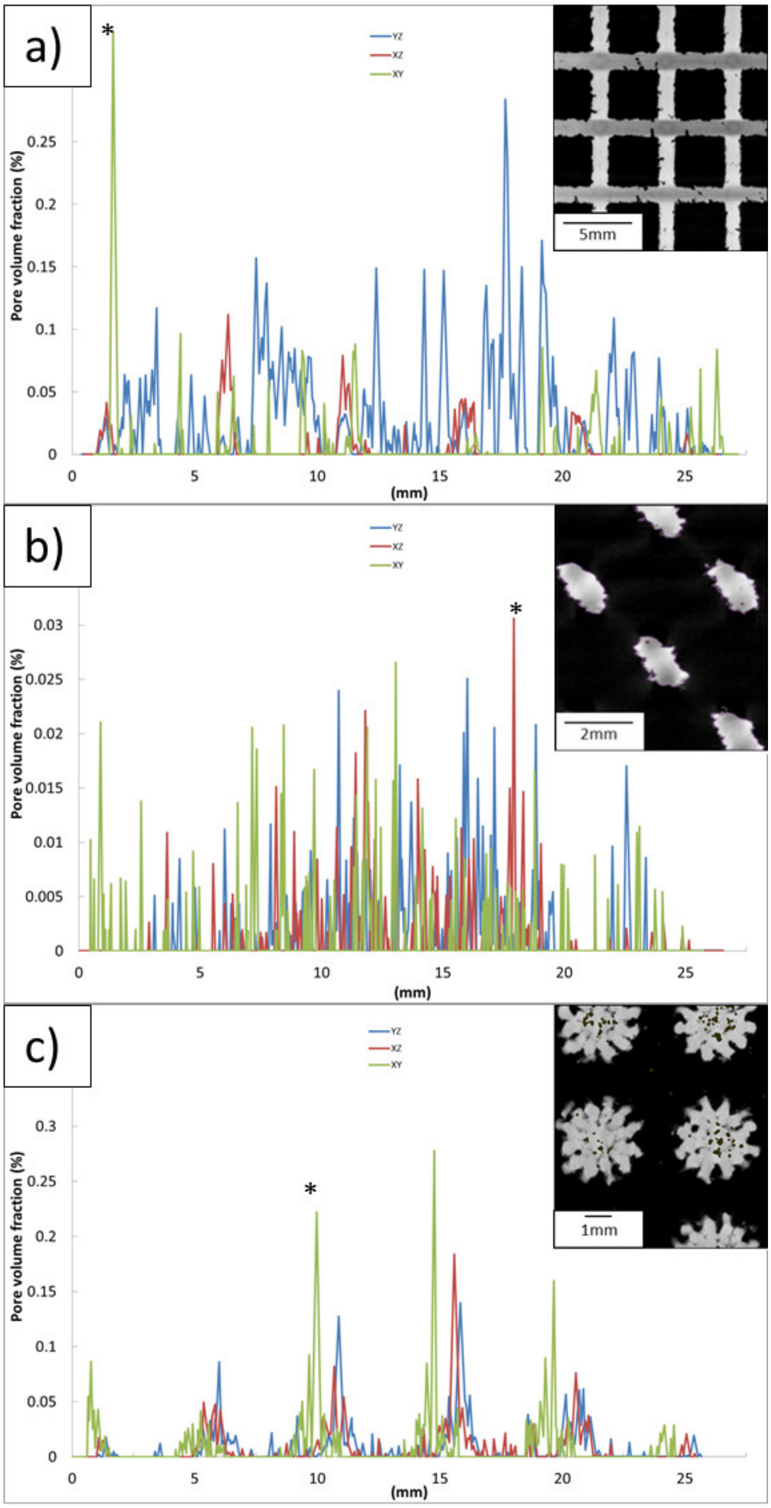

Figure 8.11: Pore volume fraction found in the three orthogonal planes of (a) cubic, (b) diamond lattices and (b) re-entrant cube lattice. Virtual slice images showing pore populated regions in the highlighted peaks are inserted for each plot; the diamond at 17.9 mm in the y direction, the cubic at 1.66 mm in the z direction and the re-entrant cube at 9.98 mm in the z direction.

structures or, highly populated at a very small scale. The characterisation of porosity on these structures however, has only been qualitatively assessed and their influence in

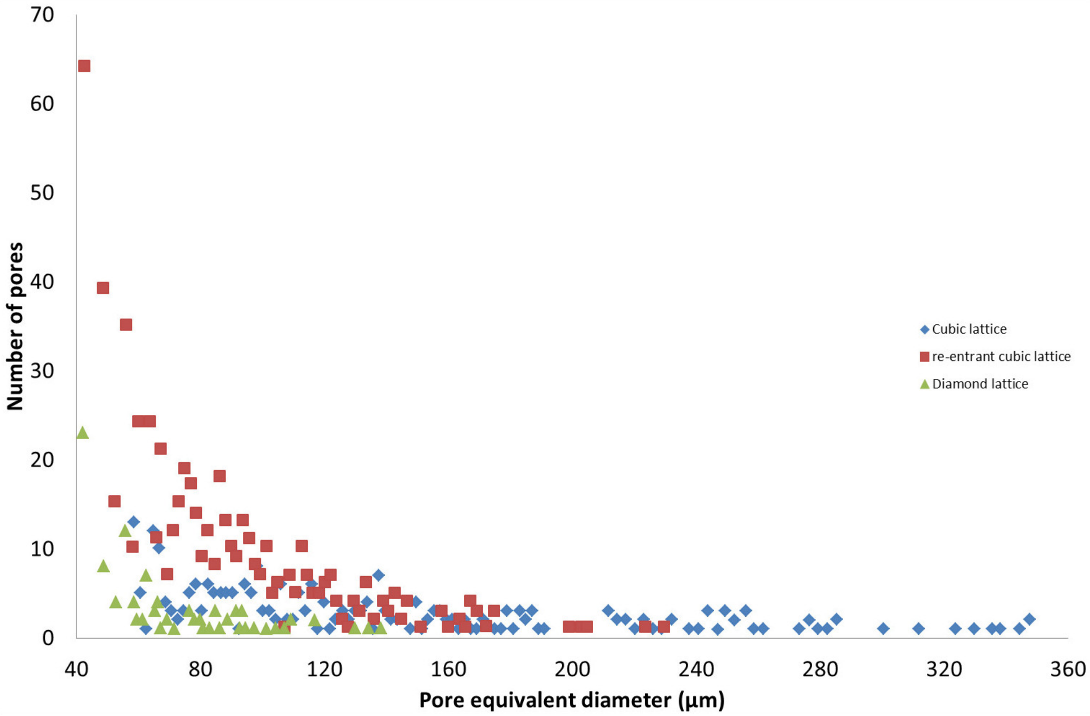

Figure 8.12: Number of pores found for the three lattices; Cubic, re-entrant and diamond.

compression resistance need to be further quantified. In chapter 6 it was commented that a minimum effect seems to exist on axially loaded elements underwent to regular plastic yielding. However, in geometries that bending moments may increase, the diamond and re-entrant structure, there may be a need for further characterisation. Despite the lack of observed defect influence, the possible generation of voids within the lattice is highlighted under the build conditions of orientation and hatching/contouring strategies employed here.

8.4 Strength comparison towards volume optimisation

Despite the heterogeneities found in cellular solids associated to the manufacturing route, pores, roughness etc., these materials manufactured additively perform and collapse according the mechanism that requires less stress. Their different compressive strengths can be tailored to specific degrees of cellular porosity so that their convenient application. In figure 8.13 the experimental failure strength for foams, cubic and diamond lattices is plotted. It can be seen that cubic lattices show a higher strength for a given density. This is suggested to be because of the parallel truss elements aligned with the load direction act efficiently upon loading. On the other side, diamond lattices display a lower response. Constructed with trusses equally orientated in respect to the build direction, these lattices tend to contain the lowest faction of internal porosity as discussed in section 8.3. Therefore their lower mechanical resistance is owned to their truss orientation and not to the fraction of defects that the manufacturing process may introduce. Metallic foams however show the lowest compressive performance. This is due to the intrinsic topology of foams that may contain smaller trusses within the solid, inducing a much earlier failure for a given relative density.

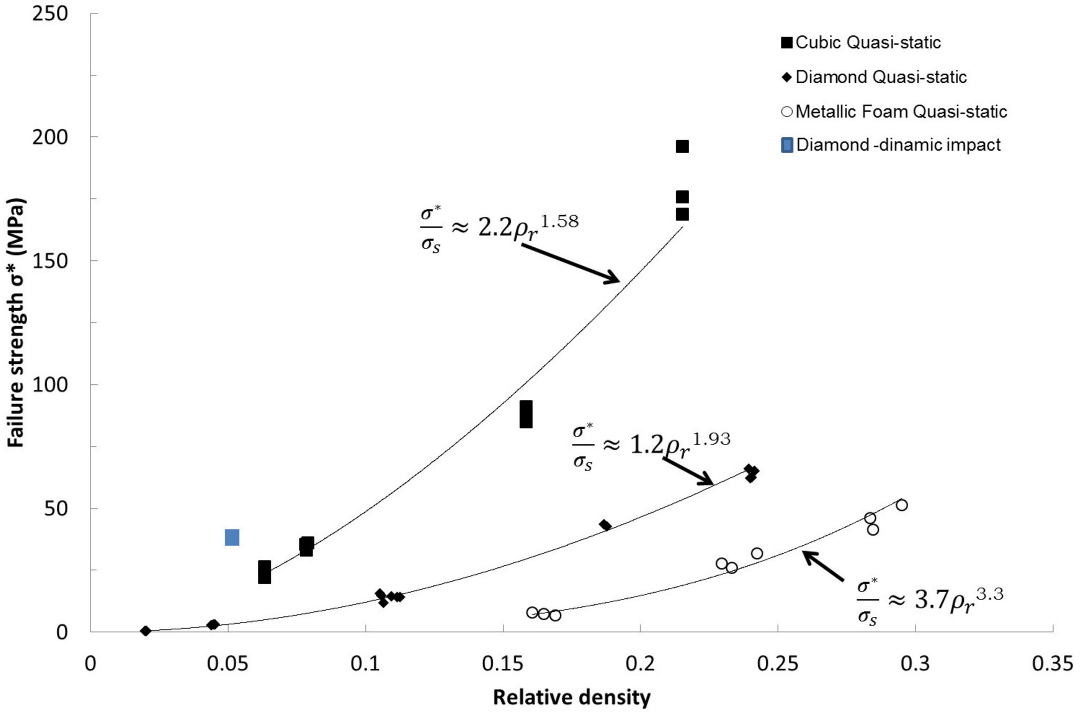

Figure 8.13: Compressive response of cubic, diamond lattices and metallic foams at quasi-static strain rate. A response of diamond under dynamic conditions is also included.

8.5 Applications for spatial spread of loading

The ability of micro-truss materials to spread the load spatially from concentrated impacts was investigated using cylinders (10 cm diameter and 10 cm height) populated with diamond lattices impacted with striker bars of 25 mm in diameter. Impacted at speeds of 25.1 m/s, the cylinders were mounted co-axially between a backplate and the striker bar one at time to record the stresses through the gauges of a HB arrangement, as explained earlier in chapter 4. Although two relative densities were attempted 0.02 and 0.06, only stress-time record of one, the $\rho = 0.06$, was possible due to a faulty record of the strain gauges when the impact took place. Still frames of the impacted specimens are shown in figures 8.14 and 8.15. The samples were orientated in such way that in the undeformed state it is possible to see through them. In the case of 0.02 relative density, the striker bar perforated the entire specimen whereas the specimen with $\rho = 0.06$ arrested the impact around 15 mm from the front face of the specimen. From the impacts, it can be seen that the thicker truss specimen shows a deformed middle area within the structure (beyond where the bar had reached) highlighted by shadows in the images. Therefore, this displacement of internal nodes can be seen as coupled movement with the broken trusses in contact with the striker bar. On the other hand, the specimen with lower density, i.e.

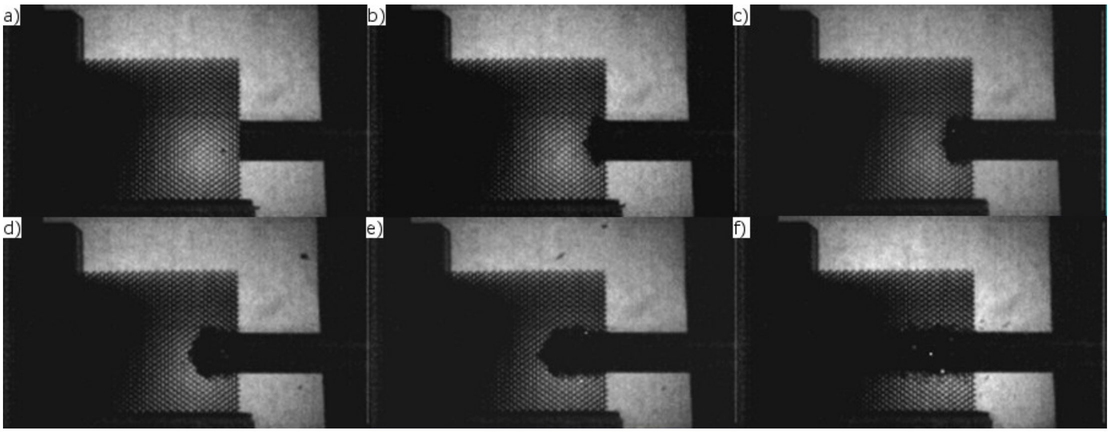

Figure 8.14: High speed stills during the impact of diamond lattice cylinder of $\rho = 0.02$, the time recorded was (a)0, (b) 315, (c) 577, (d) 892, (e) 1260 and (f) $2625\mu s$.

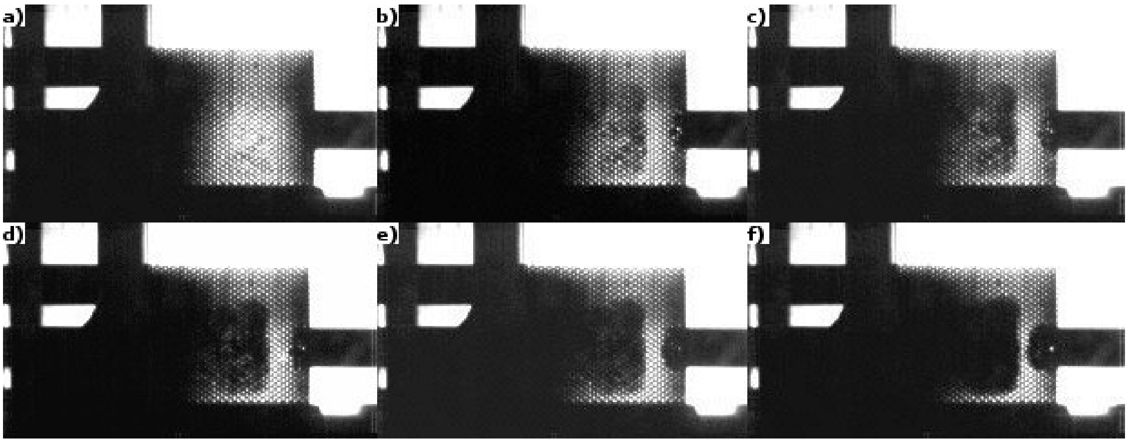

Figure 8.15: High speed stills during the impact of diamond lattice cylinder of $\rho = 0.06$, the time recorded was (a)0, (b) 110, (c)263, (d)315, (e)368 and (f)$638\mu s$.

thinner trusses, yielded and fractured only along the path of the striker bar.

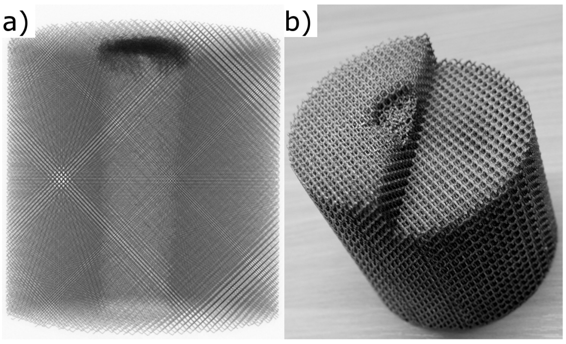

Figure 8.16: (a) CT scan of the $\rho = 0.02$ diamond sample after a HB impact where the fractured trusses are appreciated. (b) The $\rho = 0.06$ diamond cylinder sectioned showing the deformed zone at around 15mm inside.

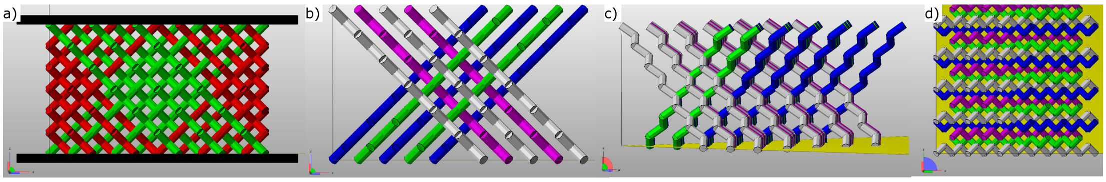

Figure 8.17: Illustration of trusses in a diamond lattice. (a) the family of trusses as wires going from top to bottom plates and unconnected wires are highlighted, (b) Four families of wires can be distinguished in the quaternary direction, (c) Plane parallel to the Z direction and (d) the top view.

This node displacement can be seen as a transmitted deformation through the trusses in contact with the striker bar. The diamond lattice, besides its carbon atomic-truss configuration, can be seen as an arrangement of connecting wires from one side to the specimen to the other. In a sandwich panel for example (figure 8.17a), these wires going from plane to plane are highlighted in green, whereas redundant or unconnected trusses are in red. It can therefore be expected that transient loading forces can be transmitted beyond the impact plane.

The loading differences applied to the diamond topology can be seen when comparing the quasi-static and dynamic response, fig. 8.13. While the bending moment takes place as the lattice is deformed quasi-statically, every truss element is prone to yield and fail. However, under dynamic conditions, material, structure and strain rate effects may take place increasing the failure resistance as the reported HB stress shown in figure 8.13.

Post-mortem CT scans were carried out in the specimen of $\rho = 0.02$ where the other sample was sectioned photographed, see figures 8.16. It can be seen that the structure at lower density could not withstand the impact deformation from the similar incoming energy. On the other hand, the higher density structure was able to stop the striking bar. Despite the results shown here, further material characterisation is required to investigate the degree of the truss elements deformation at different points of the structure in such impacts.

8.6 Chapter summary

The present chapter attempted to address common issues related to the design and AM process of lattices. Part of the analysis was the dedicated to the as-designed and experimental relative density and their influence on properties of lattices. Although volume fraction inaccuracies may be found in lattices, so their mechanical performance, their properties were evaluated according models based on Timoshenko and Euller-Bernoulli theory. It was found that, Timoshenko theory predicts a better match than Euler-Bernoulli for diamond-like lattices with relatively higher volume fraction. However, Euler-Bernoulli gives a better prediction for lower values of relative density.

Part of the volume fraction discrepancies in the form of internal pores found within these materials, was characterised by CT tomography. It was seen that lattices with a high number of trusses, so that their connectivity, the pore volume fraction increases. This may be of concern as a lack of material is usually related to a premature failure. However, it has been seen that their influence on the structural performance is complex to establish. For example, chapter 5 and 6 reports an efficiency of 5% for stochastic structures and an efficiency of 97% for cubic lattices respectively. Additionally, trusses orientated perpendicularly to the build direction, have been found to contain a relative high pore fraction too.

9

Conclusions

In this thesis it has been studied the mechanical properties of porous materials produced by Electron Beam Melting. Such materials, in the form of interconnected micro-truss elements, are intended to be used in lightweight and structural components. Some cases are in the use of sandwich panels for impact loading reduction and, materials with specific porous or volume fraction tailoring a compressive loading. Also, due to the use of AM routes, the creation of biomedical implants is allowed matching strict requirements of porous architecture to allow tissue ingrowth, specific mechanical properties and biocompatible processed materials. Overall, a characterisation of the material properties and microstructure in different conditions was carried out, i.e. as-built condition and after heat treatments. Finally, the deposition strategy in the geometry to melt was carried out in order to analyse the manufacturing-properties relationship. All these areas of study and their concluding remarks are outlined as follow.

- The electron beam penetration on solid pre-existing plates, agrees with numerical modelling for beam current and beam speed however, deviations in numerical values suggest that the single point numerical model employed here, is insufficient to totally predict the real beam penetration.
- A linear relationship between the melt pool depth and speed/current for beam parameters found in the ARCAM themes could be found. This can be seen as a characteristic melting feature from the manufacturers to obtain constant depths with changes in beam current or speed.
- The α lath thickness from the lamellar $\alpha+\beta$ microstructure was found to be directly proportional to the yield strength and elongation of the bulk material properties. Comparative measurements with other titanium alloys were additionally plotted.
- The build orientation influences the mechanical properties despite the use of identical beam parameters or raw material chemistry. This suggests that an extra variable related to thermal mass and the heat distribution remains uncharacterised.
- Metal foams could successfully be produced by 3D templates obtained by X-ray tomography to further be altered in density without a significant variation in the location and arrangement of cellular pores.
- Young's modulus in "As-built" foams reported low structural stiffness compared to ideal models, such values accentuated with reduction of feature size.
- A variation in the strength of the metal making up the foam was found to be, at least in part, due to the effect of the surface roughness. These findings suggested a

dependence of strength on size of manufactured parts, which seems to dramatically be reduces below 1 mm of feature size.

- While the mechanical properties in cubic lattices were minimally affected by heat treatments below the β-transus temperature, heat treatments above the β-transus temperature plus furnace cooling on as-built materials had a significant effect dropping the yield strength down to 10%.

- X-ray Computed Tomography revealed internal porosity that was distributed in proximity to the as-manufactured strut cross section perimeter. Such porosity presumably was re-arranged from the randomly porosity found in the powder feedstock.

- Analytical models based on solely compressive strut deformation rather than shearing or buckling, show a good agreement with experimental observations for the compressive failure strength of cubic lattices. However, shearing stresses are suggested to be taking place at the fractured surface as the micro-truss increased in size showing a transition in the failure mode.

- The cross section of micro-trusses with less than 600μm in diameter was compromised due to the beam power employed in this study. The minimum single pass with of 300μm plus a contouring melting strategy and the range of powder particles, gave oversized cross sections with a roughness of the order of the smallest particle size of the powder range, (45–100μm).

- Due to the resolution inaccuracies, comparisons between experimental results and mathematical predictions find better agreement if they are in terms of density rather than dimension of structural elements.

- A combination of the conditions used for fabrication; the melting sequence of hatching and contouring, beam power and raw material, produced characteristic internal porosity patterns for each topology.

- A high fraction of pores, irregular in shape, tend to appear in areas where the melting is compromised i.e. at nodes of high connectivity or trusses built perpendicularly to the built direction.

- The fraction of porosity on structural members built parallel to the deposition direction appears to be much lower, of an order of magnitude, than in any other orientation.

10

Future work

10.1 EBM characterisation

Although electron beam melting has been investigated in the last decades, it is a field of active development by machine manufacturers and new generations of equipment arrive continuously attempting to correlate hardware capabilities to theoretical principles. Characterising the beam efficiency is one area of particular current focus as there are apparent changes with critical EBM beam parameters, e.g. *focus offset*. Despite the accepted agreement between the prediction of microstructure through the developed solidification gradients [4], the control of the melt pool to predict the isotherms around the absorbed heat is still under debate. The size and shape, if fully predicted, could be useful to anticipate thermal cycling effects through repetitive re-melting of layers, obtaining maximum performance avoiding element vaporising temperatures.

10.2 Heat balance

The reported bulk properties in different orientations is evidence of the lack of understanding related to the heat input during the process. This can be outlined after the thermal histories developed out of the heat source. Current suggestions aim to look for a qualitative designed heat balance in qualitatively approach [59], that is based on the parts to melt and the assigned themes i.e. *melt, net, wafers* in every layer. However, these type of approaches are aimed to obtain completed builds with minimum partial and (no fatal) interruptions such as *arc trips* or *smokes* coming from "cold" areas of powder leading to build failure caused by electrostatic overcharging. Despite following this advise, and thermal cameras being implemented in some other ARCAM models, the distribution of the heat during the melting material and through all the themes remains poorly understood.

10.3 Deposition strategies

Most of the applications for cellular materials involve conditions needing good resolution at small scale. For the EBM technology, it is well known that the minimum achieved feature size is determined by the developed melt pool and the heat source. Although not analytically determined in this investigation, the size and shape of the melt pool and its consequences were reported after observing the weldtrack and its width (chapter 4), suggesting possible adjustments composed by overlaps and offsets for further thinner features to be explored.

10.4 Grain growth in narrow sections

Replication of parent materials properties needs more exploration if the microstructure is changed in a similar fashion as reported in chapter 6. This is as after the effects of high temperature heat treatments can not be predicted in terms of the bulk properties only, and that the compressive strength of lattices with small elements was dramatically decreased. The recrystallization and grain growth seen in $\alpha + \beta$ alloys previously cooled at high rates from the β phase can be related to features that need prior characterisation such as the dislocation densities that may or may not influence the driving force of recrystallisation [166], see equation 10.1 where ΔE is the recrystallised state, ρ is the dislocation density, G and b the shear modulus and the Burgers vector of the dislocations.

$$\Delta E = \rho G b^2 \tag{10.1}$$

On the other hand, the temperature and solute content are among the factors affecting the grain growth allowing, to some extent, boundary mobility, in which the rate of grain growth diminishes with specimen thickness [167], especially if the grains become bigger as in the case of the samples heat treated at 1200°C2h/FC, see image 7.6.

10.5 Defect location and loading direction

Although internal porosity and surface roughness was found to be significant, the effect of axial stresses reported in chapter 6 seemed to be negligible. While a similar fraction of defects was found in samples loaded by bending, the resistance shown a dramatic low efficiency (chapter 5). Therefore is suggested that defect location in combination to loading direction may affect the strength of these materials.

It is known that upon plastic deformation, the micromechanism of ductile fracture in porous metals is caused by microvoid coalescence appearing in areas subjected to tensile stresses [168]. It is also known that these mechanisms are nucleated at regions of localised strain such as discontinuities, see schematic figure 10.1 [169] leading to crack propagation and failure. Hence, it is the distribution of these microvoids and nucleation sites will affect the maximum load in bending-type structures within the structural elements that may lead to premature failure.

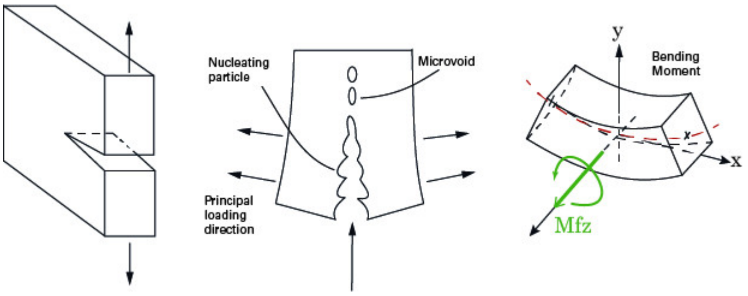

Figure 10.1: Fracture tearing loading mode showing the fracture direction developed upon bending forces within strut elements.

As most of the microporosity inserted in EBM components is derived from the raw material and melting strategies as *contouring/hatching* offsets [65], the influence of the porosity remnants within the lattice members on the path leading to failure is unknown.

References

[1] S. L. Semiatin and T. R. Bieler. The effect of alpha platelet thickness on plastic flow during hot working of Ti-6Al-4V with a transformed microstructure. *Acta Materialia*, 49:3565–3573, 2001.

[2] Y. T. Lee and G. Welsch. Youngs modulus and damping capacity of Ti-6Al-4V alloy as a function of heat-treatment and oxygen concentration. *Materials Science and Engineering: A1*, A128:77–89, 1990.

[3] D. Coney and M. Lasker. *Aerospace structural metals Handbook*. 1969.

[4] P. A. Kobryn and S. L. Semiatin. The laser additive manufacturing of Ti-6Al-4V. *JOM*, 53(9):40–42, 2001.

[5] T. Ahmed and H.J. Rack. Phase transformations during cooling in α+β titanium alloys. *Materials Science and Engineering: A*, 243(1-2):206–211, 1998.

[6] L. E. Murr, S. M. Gaytan, D. A. Ramirez, E. Martinez, J. Hernandez, K. N. Amato, P.W. Shindo, F.R. Medina, and R.B. Wicker. Metal Fabrication by Additive Manufacturing Using Laser and Electron Beam Melting Technologies. *Journal of Materials Science & Technology*, 28(1):1–14, 2012.

[7] P. Hanzl, M. Zetek, T. Bakša, and T. Kroupa. The Influence of Processing Parameters on the Mechanical Properties of SLM Parts. *Procedia Engineering*, 100: 1405–1413, 2015.

[8] H. Gong, K. Rafi, H. Gu, G. D. Janaki Ram, T. Starr, and B. Stucker. Influence of defects on mechanical properties of Ti-6Al-4V components produced by selective laser melting and electron beam melting. *Materials and Design*, 86:545–554, 2015.

[9] H. K. Rafi, N. V. Karthik, H. Gong, T. L. Starr, and B. E. Stucker. Microstructures and mechanical properties of Ti6Al4V parts fabricated by selective laser melting and electron beam melting. *Journal of Materials Engineering and Performance*, 22(12): 3872–3883, 2013.

[10] B. E. Carroll, T. A. Palmer, and A. M. Beese. Anisotropic tensile behavior of Ti–6Al–4V components fabricated with directed energy deposition additive manufacturing. *Acta Materialia*, 87:309–320, 2015.

[11] E. Sallica-Leva, A.L. Jardini, and J.B. Fogagnolo. Microstructure and mechanical behavior of porous Ti-6Al-4V parts obtained by selective laser melting. *Journal of the Mechanical Behavior of Biomedical Materials*, 26:98–108, 2013.

[12] P. Heinl, C. Körner, and R. F. Singer. Selective Electron Beam Melting of Cellular Titanium: Mechanical Properties. *Advanced Engineering Materials*, 10(9):882–888, 2008.

[13] M. F. Ashby. The properties of foams and lattices. *Philosophical transactions. Series A, Mathematical, physical, and engineering sciences*, 364(1838):15–30, jan 2006.

[14] M. F. Ashby, A. Evans, N. A. Fleck, L. J. Gibson, J. W. Hutchinson, and H. N. G. Wadley. *Metal foams. A design guide.* Butterworth-Heinemann, 2000.

[15] V. S. Deshpande and N. A. Fleck. High strain rate compressive behaviour of aluminium alloy foams. *International Journal of Impact Engineering*, 24(3):277–298, 2000.

[16] L. Yang, O. Harrysson, H. West, and D. Cormier. Compressive properties of Ti–6Al–4V auxetic mesh structures made by electron beam melting. *Acta Materialia*, 60(8):3370–3379, may 2012.

[17] S. M. Ahmadi, G. Campoli, S. Amin Yavari, B. Sajadi, R. Wauthle, J. Schrooten, H. Weinans, and A. Zadpoor. Mechanical behavior of regular open-cell porous biomaterials made of diamond lattice unit cells. *Journal of the Mechanical Behavior of Biomedical Materials*, 34:106–115, 2014.

[18] A. Amendola, E. Hernández-Nava, R. Goodall, I. Todd, R.E. Skelton, and F. Fraternali. On the additive manufacturing, post-tensioning and testing of bi-material tensegrity structures. *Composite Structures*, 131:66–71, 2015.

[19] A. Inayat, J. Schwerdtfeger, H. Freund, C. Körner, R.F. Singer, and W. Schwieger. Periodic open-cell foams: Pressure drop measurements and modeling of an ideal tetrakaidecahedra packing. *Chemical Engineering Science*, 66:2758–2763, 2011.

[20] J. Parthasarathy, B. Starly, S. Raman, and A. Christensen. Mechanical evaluation of porous titanium (Ti6Al4V) structures with electron beam melting (EBM). *Journal of the mechanical behavior of biomedical materials*, 3(3):249–59, apr 2010.

[21] X.Y. Cheng, S.J. Li, L.E. Murr, Z.B. Zhang, Y.L. Hao, R. Yang, F. Medina, and R.B. Wicker. Compression deformation behavior of Ti – 6Al – 4V alloy with cellular structures fabricated by electron beam melting. 2012.

[22] L. E. Murr, K. N. Amato, S. J. Li, Y. X. Tian, X. Y. Cheng, S. M. Gaytan, E. Martinez, P. W. Shindo, F. Medina, and R. B. Wicker. Microstructure and mechanical properties of open-cellular biomaterials prototypes for total knee replacement implants fabricated by electron beam melting. *Journal of the mechanical behavior of biomedical materials*, 4(7):1396–1411, oct 2011.

[23] R. Wauthle, B. Vrancken, B. Beynaerts, K. Jorissen, J. Schrooten, J. P. Kruth, and J. Van Humbeeck. Effects of build orientation and heat treatment on the microstructure and mechanical properties of selective laser melted Ti6Al4V lattice structures. *Additive Manufacturing*, 5:77–84, 2015.

[24] S. J. Li, Q. S. Xu, Z. Wang, W. T. Hou, Y. L. Hao, R. Yang, and L. E. Murr. Influence of cell shape on mechanical properties of Ti-6Al-4V meshes fabricated by electron beam melting method. *Acta Biomaterialia*, 10(10):4537–4547, 2014.

[25] J. Tiley, T. Searles, E. Lee, S. Kar, R. Banerjee, J.C. Russ, and H.L. Fraser. Quantification of microstructural features in α/β titanium alloys. *Materials Science and Engineering: A*, 372(1-2):191–198, may 2004.

[26] S. S. Al-Bermani, M. L. Blackmore, W. Zhang, and I. Todd. The Origin of Microstructural Diversity, Texture, and Mechanical Properties in Electron Beam Melted Ti-6Al-4V. *Metallurgical and Materials Transactions A*, 41(13):3422–3434, aug 2010.

[27] W. Xu, M. Brandt, S. Sun, J. Elambasseril, Q. Liu, K. Latham, K. Xia, and M. Qian. Additive manufacturing of strong and ductile Ti–6Al–4V by selective laser melting via in situ martensite decomposition. *Acta Materialia*, 85:74–84, 2015.

[28] T. Vilaro, C. Colin, and J. D. Bartout. As-fabricated and heat-treated microstructures of the Ti-6Al-4V alloy processed by selective laser melting. *Metallurgical and Materials Transactions A: Physical Metallurgy and Materials Science*, 42:3190–3199, 2011.

[29] R. Z. Valiev and I. V. Alexandrov. Development of severe plastic deformation techniques for the fabrication of bulk nanostructured materials. *Annales de Chimie: Science des Materiaux*, 27(3):3–14, 2002.

[30] S. Nagn and R. Banerjee. Laser deposition and deformation behavior of Ti-Nb-Zr-Ta alloys for orthopedic implan. *Journal of the Mechanical Behavior of Biomedical Materials*, 16:21–28, 2012.

[31] L. E. Murr, S. A. Quinones, S. M. Gaytan, M. I. Lopez, A. Rodela, E. Y. Martinez, D. H. Hernandez, E. Martinez, F. Medina, and R. B. Wicker. Microstructure and mechanical behavior of Ti-6Al-4V produced by rapid-layer manufacturing, for biomedical applications. *Journal of the Mechanical Behavior of Biomedical Materials*, 2(1):20–32, 2009.

[32] B. Baufeld, O. Van Der Biest, and S. Dillien. Texture and crystal orientation in Ti-6Al-4V builds fabricated by shaped metal deposition. *Metallurgical and Materials Transactions A: Physical Metallurgy and Materials Science*, 41(August):1917–1927, 2010.

[33] E. Brandl, F. Palm, V. Michailov, B. Viehweger, and C. Leyens. Mechanical properties of additive manufactured titanium (Ti-6Al-4V) blocks deposited by a solid-state laser and wire. *Materials and Design*, 32(10):4665–4675, 2011.

[34] B. Vandenbroucke and J.P. Kruth. Selective laser melting of biocompatible metals for rapid manufacturing of medical parts. *Rapid Prototyping Journal*, 13(4):196–203, 2007.

[35] A. Mortensen, Y. Conde, A. Rossoll, and C. San Marchi. Scaling of conductivity and Young's modulus in replicated microcellular materials. *Journal of Materials Science*, 48(23):8140–8146, aug 2013.

[36] B. Dutta and F. H. Froes. Additive Manufacturing of Titanium Alloys. *Advanced Materials & Procesees*, (February):18–23, 2014.

[37] G. Welch, R. Boyer, and E. W. Collings, editors. *Material Properties handbook: Titanium Alloys.* ASM International, Materials Park, OH, USA, 2nd edition, 1998.

[38] I. Gibson, D.W. Rosen, and B. Stucker. *Rapid Manufacturing Technologies. Rapid Prototyping to Direct Digital Manufacturing.* Springer, 2010.

[39] O. Ivanova, C. Williams, and T. Campbell. Additive manufacturing (AM) and nanotechnology: promises and challenges. *Rapid Prototyping Journal*, 19(5):353–364, 2013.

[40] A. Gebhardt. *Understanding additive manufacturing.* Hanser Gardner Publications, 2012.

[41] S. Das. Physical Aspects of Process Control in Selective Laser Sintering of Metals. *Advanced Engineering Materials*, 5(10):701–711, 2003.

[42] H. Milkert. GE Uses Breakthrough New Electron Gun For 3D Printing – 10X's More Powerful Than Laser Sintering, 2014. URL `http://3dprint.com/12262/ge-ebm-3d-printing/`.

[43] L. E. Murr, S. M. Gaytan, F. Medina, H. Lopez, E. Martinez, B. I. Machado, D. H. Hernandez, L. Martinez, M. I. Lopez, R. B. Wicker, and J. Bracke. Next-generation biomedical implants using additive manufacturing of complex, cellular and functional mesh arrays. *Philosophical transactions. Series A, Mathematical, physical, and engineering sciences*, 368(1917):1999–2032, apr 2010.

[44] A. Liszewski. The World's First 3D-Printed Titanium Rib Cage Is a Medical Marvel. 2015. URL http://gizmodo.com/the-worlds-first-3d-printed-titanium-rib-cage-is-a-medi-1730034483, 2015.

[45] G. Lütjering and J.C. Williams. *Titanium. Engineering materials and processes.* Springer, 2nd edition, 2007.

[46] W. D. Callister. *Materials Science and Engineering.* John Wiley & Sons., 7th edition, 2007.

[47] I. P. Jones and W. B Hutchinson. Stress-state dependence of slip in Titanium-6Al-4V and other H.C.P. metals. *Acta Metallurgica*, 29(6):951–968, 1981.

[48] I. Polmear. *Ligth Alloys.* Elsevier, fourth edi edition, 1981.

[49] G. Stevenson, S. Rehmana, E. Draper, E. Hernández-Nava, J Hunt, and W. Haycock. Combining 3D human in vitro methods for a 3Rs evaluation of novel titanium surfaces in orthopaedic applications. *Biotechnology & Bioengineering.*, 9999, 2016.

[50] H. Kuhn and D. Medlin, editors. *ASM Handbook. Volume 8: Mechanical Testing and Evaluation.* ASM International, 10th edition.

[51] S. Banerjee and P. Mukhopadhyay. *Phase trasformations. Examples from titanium and zirconium alloys.* Pergamon Materials series, 2007.

[52] C. Leyens and M. Peters. *Titanium and titanium alloys.* WILEY-VCH GmbH & Co., 2003.

[53] A. E. Markaki and A. W. Justin. A magneto-active scaffold for stimulation of bone growth. *Materials Science and Technology*, 30(13):in press, 2014.

[54] M. L. Weaver and H. Garmestani. Microstructures and mechanical properties of commercial titanium foils processed via the melt overflow process. *Materials Science and Engineering: A*, 247:229–238, 1998.

[55] M. R. Bache and W. J. Evans. Impact of texture on mechanical properties in an advanced titanium alloy. *Materials Science and Engineering A*, 319-321:409–414, 2001.

[56] A. N. Kalinyuk, N. P. Trigub, V. N. Zamkov, O. M. Ivasishin, P. E. Markovsky, R. V. Teliovich, and S. L. Semiatin. Microstructure, texture, and mehanical properties of electron-beam melted Ti-6Al-4V. *Materials Science and Engineering A*, 346:178–188, 2003.

[57] A. Zarkades and F. R. Larson. The science, technology and application of Titanium. page 933, Oxford UK., 1970. Pergamon Press.

[58] B. Verlinden, J. Driver, I. Samajdar, and R. Doherty. *Thermo-mechanical processing of metallic materials*. 2007.

[59] ARCAM. EBM Operator level 2 training, 2011.

[60] D. A. Ramirez, L. E. Murr, S. J. Li, Y. X. Tian, E. Martinez, J. L. Martinez, B. I. Machado, S. M. Gaytan, F. Medina, and R. B. Wicker. Open-cellular copper structures fabricated by additive manufacturing using electron beam melting. *Materials Science and Engineering: A*, 528(16-17):5379–5386, jun 2011.

[61] L. E. Murr, E Martinez, S. M. Gaytan, D. A. Ramirez, B. I. Machado, P. W. Shindo, J. L. Martinez, F. Medina, J. Wooten, D. Ciscel, U. Ackelid, and R. B. Wicker. Microstructural architecture, microstructures and mechanical performance for a Nickel-base supper alloy fabricated by electron beam melting. *Metallurgical and Materials Transactions A*, 42A(11):3491–3508, 2011.

[62] L. E. Murr, S. M. Gaytan, A. Ceylan, E. Martinez, J. L. Martinez, D. H. Hernandez, B. I. Machado, D. A. Ramirez, F. Medina, and S. Collins. Characterization of titanium aluminide alloy components fabricated by additive manufacturing using electron beam melting. *Acta Materialia*, 58(5):1887–1894, mar 2010.

[63] C. Körner, E. Attar, and P. Heinl. Mesoscopic simulation of selective beam melting processes. *Journal of Materials Processing Technology*, 211(6):978–987, 2011.

[64] M. Gebler, A. J. M. Schoot Uiterkamp, and C. Visser. A global sustainability perspective on 3D printing technologies. *Energy Policy*, 74:158–167, 2014.

[65] S. Tammas-Williams, H. Zhao, F. Leonard, F. Derguti, I. Todd, and P.B. Pragnell. XCT analysis of the influence of melt strategies of defect population in titanium components manufactured by selective electron beam melting. *Materials characterisation.*, 102:47–61, 2015.

[66] R. M. German. *Powder metallurgy and particulate materials processing.* Metal powder industry, 2005.

[67] www.metalysis.com.

[68] Metalysis titanium powder used to 3D print automotive parts, 2013. URL `www.metalysis.com`.

[69] S. M. Gaytan, L. E. Murr, F. Medina, E. Martinez, M. I. Lopez, and R. B. Wicker. Advanced metal powder based manufacturing of complex components by electron beam melting. *Materials Technology: Advanced Performance Materials*, 24(3):180–190, sep 2009.

[70] O. Cansizoglu, O. Harrysson, D. Cormier, H. West, and T. Mahale. Properties of Ti–6Al–4V non-stochastic lattice structures fabricated via electron beam melting. *Materials Science and Engineering: A*, 492(1-2):468–474, sep 2008.

[71] C.J. Smith, F. Derguti, E. Hernandez-Nava, S. Tammas-Williams, S. Gulizia, D. Fraser, and I. Todd. Dimensional accuracy of Electron Beam Melting (EBM) Additive Manufacture with regard to weight optimized truss structures. *Journal of Materials Processing Technology (Under Review).*

[72] Y. Arata and M. Tomie. Advanced welding technology. In *2nd Int. Conf. of Japan Weld. Soc.*, page 45, 1975.

[73] D. T. Swift-Hook and A. E. F. Gick. Penetration welding with lasers. *Welding Journal*, 52:492–499, 1973.

[74] S. Bontha, N.W. Klingbeil, P.A. Kobryn, and H.L. Fraser. Thermal process maps for predicting solidification microstructure in laser fabrication of thin-wall structures. *Journal of Materials Processing Technology*, 178:135–142, 2006.

[75] D. Couëdel, P. Rogeon, P. Lemasson, M. Carin, J. C. Parpillon, and R. Berthet. 2D-heat transfer modelling within limited regions using moving sources: Application to electron beam welding. *International Journal of Heat and Mass Transfer*, 46:4553–4559, 2003.

[76] J. W. Elmer, W. H. Giedt, and T. W. Eagar. The Transition from Shallow to Deep Penetration during Electron Beam Welding. *Welding Journal*, (May):1167–1176, 1990.

[77] S. S. Al-Bermani. *An investigation into microstructure and microstructural control of additive layer manufactured Ti-6Al-4V by electron beam melting.* Ph.d thesis, The University of Sheffield, 2011.

[78] J. Karlsson, A. Snis, H. Engqvist, and J. Lausmaa. Characterization and comparison of materials produced by Electron Beam Melting (EBM) of two different Ti-6Al-4V powder fractions. *Journal of Materials Processing Technology*, 213(12):2109–2118, 2013.

[79] ARCAM. Review of present Ti-6Al-4V material properties. EBM user group meeting. Technical report, Skaftö. Sweden, 2012.

[80] N. Hrabe and T. Quinn. Effects of processing on microstructure and mechanical properties of a titanium alloy (Ti-6Al-4V) fabricated using electron beam melting (EBM), Part 2: Energy input, orientation, and location. *Materials Science and Engineering A*, 573:271–277, 2013.

[81] P. Edwards, A. O'Conner, and M. Ramulu. Electron Beam Additive Manufacturing of Titanium Components: Properties and Performance. *Journal of Manufacturing Science and Engineering*, 135(6):061016, 2013.

[82] N. Hrabe and T. Quinn. Effects of processing on microstructure and mechanical properties of a titanium alloy (Ti-6Al-4V) fabricated using electron beam melting (EBM), part 1: Distance from build plate and part size. *Materials Science and Engineering A*, 573:264–270, 2013.

[83] M. Koike, K. Martinez, L. Guo, G. Chahine, R. Kovacevic, and T. Okabe. Evaluation of titanium alloy fabricated using electron beam melting system for dental applications. *Journal of Materials Processing Technology*, 211(8):1400–1408, 2011.

[84] G. Chahine, M. Koike, T. Okabe, P. Smith, and R. Kovacevic. The design and production of Ti-6Al-4V ELI customized dental implants. *Jom*, 60(11):50–55, 2008.

[85] L. E. Murr, E. V. Esquivel, S. a. Quinones, S. M. Gaytan, M. I. Lopez, E. Y. Martinez, F. Medina, D. H. Hernandez, E. Martinez, J. L. Martinez, S. W. Stafford, D. K. Brown, T. Hoppe, W. Meyers, U. Lindhe, and R. B. Wicker. Microstructures and mechanical properties of electron beam-rapid manufactured Ti-6Al-4V biomedical prototypes compared to wrought Ti-6Al-4V. *Materials Characterization*, 60(2): 96–105, 2009.

[86] A. Foroozmehr, M. Badrossamay, E. Foroozmehr, and S. Golabi. Finite Element Simulation of Selective Laser Melting process considering Optical Penetration Depth of laser in powder bed. *Materials and Design*, 89:255–263, 2016.

[87] E. Marin, S. Fusi, M. Pressacco, L. Paussa, and L. Fedrizzi. Characterization of cellular solids in Ti6Al4V for orthopaedic implant applications: Trabecular titanium. *Journal of the mechanical behavior of biomedical materials*, 3(5):373–81, jul 2010.

[88] T. W. Clyne, I. O. Golosnoy, J. C. Tan, and A. E. Markaki. Porous materials for thermal management under extreme conditions. *Philosophical transactions. Series A, Mathematical, physical, and engineering sciences*, 364(1838):125–146, 2006.

[89] R. Goodall, L. Weber, and A. Mortensen. The electrical conductivity of microcellular metals The electrical conductivity of microcellular metals. *Journal of applied physics*, 044912, 2006.

[90] M.A. Navacerrada, P. Fernández, C. Díaz, and A. Pedrero. Thermal and acoustic properties of aluminium foams manufactured by the infiltration process. *Applied Acoustics*, 74(4):496–501, apr 2013.

[91] L. J. Gibson and M. F. Ashby. *Cellular Solids Structure and Properties*. Cambridge, 1997.

[92] J. Parthasarathy, B. Starly, and S. Raman. A design for the additive manufacture of functionally graded porous structures with tailored mechanical properties for biomedical applications. *Journal of Manufacturing Processes*, 13:160–170, 2011.

[93] P. Heinl, A. Rottmair, C. Körner, and R.F. Singer. Cellular titanium by selective electron beam melting. *Advanced Engineering Materials*, 9(5):360–364, 2007.

[94] M. Jamshidinia, L. Wang, W. Tong, and R. Kovacevic. The bio-compatible dental implant designed by using non-stochastic porosity produced by Electron Beam Melting (EBM). *Journal of Materials Processing Technology*, 214(8):1728–1739, 2014.

[95] V. S. Deshpande, M. F. Ashby, and N. A. Fleck. Foam topology: bending versus stretching dominated architectures. *Acta Materialia*, 49(6):1035–1040, apr 2001.

[96] J. Case, A.H. Chilver, and C.T.F. Ross. *Strength of materials and structures : with an introduction to finite element methods*. London : Edward Arnold, 1993, 3rd ed. edition, 1993.

[97] E. Hernández-Nava, C.J. Smith, F. Derguti, S. Tammas-Williams, F. Léonard, P.J. Withers, I. Todd, and R. Goodall. The effect of density and feature size on mechanical properties of isostructural metallic foams produced by additive manufacturing. *Acta Materialia*, 85:387–395, feb 2015.

[98] C. R. Calladine and R. W. English. Strain-rate and inertia effects in the collapse of two types of energy-absorbing structure. *International Journal of Mechanical Sciences*, 26(11-12):689–701, 1984.

[99] H. N. G. Wadley. Multifunctional periodic cellular metals. *Philosophical transactions. Series A, Mathematical, physical, and engineering sciences*, 364(1838):31–68, jan 2006.

[100] H. N. G. Wadley. Cellular Metals Manufacturing. *Advanced Engineering Materials*, 4(10):726–733, oct 2002.

[101] R. E. Shallman and R. J. Bishop. Mechanical behaviour of materials. In *Modern Physical metallurgy & Materials Engineering*, chapter Mechanical, pages 197–258. Butterworth-Heinemann, 6th ed. edition, 1999.

[102] ASM International. Handbook Committee. *ASM Handbook. Volume 2. Properties and Selection : Nonferrous Alloys and Special-Purpose Materials*. 10th edition, 1990.

[103] S. L. Semiatin, V. Seetharaman, and I. Weiss. Flow behavior and globularization kinetics during hot working of Ti–6Al–4V with a colony alpha microstructure. *Materials Science and Engineering: A*, 263(2):257–271, 1999.

[104] Z. Ozdemir, E. Hernandez-Nava, A. Tyas, J. A. Warren, S. D. Fay, R. Goodall, I. Todd, and H. Askes. Energy absorption in micro-truss materials in dynamics : Part I-Experiments. *International Journal of Impact Engineering-Preprint*.

[105] Z. Xue and J. W. Hutchinson. Preliminary assessment of sandwich plates subject to blast loads. *Int. J. Mech. Sci.*, 45:687–705, 2003.

[106] A. E. Markaki and T. W. Clyne. Mechanics of thin ultra-light stainless steel sandwich sheet material: Part I. Stiffness. *Acta Materialia*, 51(5):1341–1350, 2003.

[107] J. W. Hutchinson and Z. Xue. Metal sandwich plates optimized for pressure impulses. *Int. J. Mech. Sci.*, 47:545–569, 2005.

[108] N. A. Fleck and V. S. Deshpande. The resistance of clamped sandwich beams to shock loading. *J. Appl. Mech.*, 71:386–401, 2004.

[109] X. Qiu, V. S. Deshpande, and N. A. Fleck. Dynamic response of a clamped circular sandwich plate subject to shock loading. *J. Appl. Mech.*, 71:637–645, 2004.

[110] Z. Xue and J.W. Hutchinson. A comparative study of impulse-resistant metal sandwich plates. *International Journal of Impact Engineering*, 30:1283–1305, 2004.

[111] S. R. Reid and C. Peng. Dynamic uniaxial crushing of wood. *International Journal of Impact Engineering*, 19(5-6):531–570, 1997.

[112] M. Guden, E. Celik, E. Akar, and S. Cetiner. Compression testing of a sintered Ti6Al4V powder compact for biomedical applications. *Materials Characterization*, 54(4-5):399–408, 2005.

[113] M. G. da Silva and K. T. Ramesh. The rate-dependent deformation and localization of fully dense and porous Ti-6Al-4V. *Materials Science and Engineering: A*, 232 (1-2):11–22, 1997.

[114] O. Harrysson, O. Cansizoglu, D. J. Marcellin-Little, D. R. Cormier, and H. A. West. Direct metal fabrication of titanium implants with tailored materials and mechanical properties using electron beam melting technology. *Materials Science and Engineering: C*, 28(3):366–373, 2008.

[115] D. A. Hollander, M. von Walter, T. Wirtz, R. Sellei, B. Schmidt-Rohlfing, O. Paar, and H. J. Erli. Structural, mechanical and in vitro characterization of individually structured Ti–6Al–4V produced by direct laser forming. *Biomaterials*, 27(7):955–963, 2006.

[116] L. E. Murr, S. M. Gaytan, F. Medina, E. Martinez, J. L. Martinez, D. H. Hernandez, B. I. Machado, D. A. Ramirez, and R. B. Wicker. Characterization of Ti–6Al–4V open cellular foams fabricated by additive manufacturing using electron beam melting. *Materials Science and Engineering: A*, 527(7-8):1861–1868, mar 2010.

[117] J. Parthasarathy, B. Starly, S. Raman, and A. Christensen. Mechanical evaluation of porous titanium (Ti6Al4V) structures with electron beam melting (EBM). *Journal of the mechanical behavior of biomedical materials*, 3(3):249–59, apr 2010.

[118] B. Gorny, T. Niendorf, J. Lackmann, M. Thoene, T. Troester, and H. J. Maier. In situ characterization of the deformation and failure behavior of non-stochastic porous structures processed by selective laser melting. *Materials Science and Engineering A*, 528(27):7962–7967, 2011.

[119] K. Hazlehurst, C. J. Wang, and M. Stanford. Evaluation of the stiffness characteristics of square pore CoCrMo cellular structures manufactured using laser melting technology for potential orthopaedic applications. *Materials and Design*, 51:949–955, 2013.

[120] L. Yang, D. Cormier, H. West, O. Harrysson, and K. Knowlson. Non-stochastic Ti-6Al-4V foam structures with negative Poisson's ratio. *Materials Science and Engineering A*, 558:579–585, 2012.

[121] P. Heinl, L. Müller, C. Körner, R. F. Singer, and F. A. Müller. Cellular Ti–6Al–4V structures with interconnected macro porosity for bone implants fabricated by selective electron beam melting. *Acta Biomaterialia*, 4(5):1536–1544, 2008.

[122] Z. Ozdemir, A. Tyas, R. Goodall, and H. Askes. Energy absorption in micro-truss materials in statics and dynamics : Part II-Nonlinear FE simulations. *Submitted to the Journal of the Mechanics and Physics of Solids.*, 2013.

[123] D. Rosenthal. The theory of moving sources of heat and its application to metal treatments. *Transactions ASME*, 11(43):849–866, 1946.

[124] T. W. Eagar and T. S. Tsai. Temperature fields produced by traveling distributed heat sources. *Welding journal*, 62(12):346–355, 1983.

[125] J. W. Elmer. *The influence of cooling rate on the microstructure of stainless steel alloys.* Scd thesis, Massachusetts Institute Of Technology, Cambridge, Mass., 1988.

[126] Y. Wang, P. Fu, Y. Guan, Z. Lu, and Y. Wei. Research on modeling of heat source for electron beam welding fusion-solidification zone. *Chinese Journal of Aeronautics*, 26(1):217–223, 2013.

[127] S. Kou. *Welding metallurgy.* John Wiley & Sons., New York, 1987.

[128] D. A. Porter and K. E. Easterling. *Phase trasformations in metals and alloys.* Chapman & Hall, 1981.

[129] W.G. Burgers. On the process of transition of the cubic-body-centered modification into the hexagonal-close-packed modification of zirconium. *Physica*, 1(7-12):561–586, 1934.

[130] L. Wang and S. Felicelli. Influence of Process Parameters on the Phase Transformation and Consequent Hardness Induced by the LENS$^{\mathrm{TM}}$ Process. In *TMS Annual Meeting & Exhibition*, Orlando, Fl, USA, 2007.

[131] S. Dushman. Chapter 10. In *Scientific foundations of vacuum technique*, chapter Chapter 10. John Wiley & Sons., 2nd edition, 1962.

[132] G. Lütjering, J. Albrecht, and O. M. Invasishin. Microstructure/Property Relationships of Titanium Titanium Alloys. In *TMS*, page 65, Warrendale, USA, 1994.

[133] S. L. Semiatin, V. Seetharaman, A. K. Ghosh, E. B. Shell, M. P. Simon, and P. N. Fagin. Cavitation during hot tension testing of Ti–6Al–4V. *Materials Science and Engineering: A*, 256(1-2):92–110, nov 1998.

[134] R. Banerjee, S. Nag, S. Samuel, and H.L. Fraser. Laser-deposited Ti-Nb-Zr-Ta orthopedic alloys. *Journal of biomedical materials research. Part A*, 78A:298–305, 2006.

[135] Y.T. Lee and G. Welsch. Young's modulus and damping of Ti-6Al-4V alloy as a function of heat treatment and oxygen concentration. *Materials Science and Engineering: A*, 128:77–89, 1990.

[136] R. Goodall and A. Mortensen. Porous metals. In David Laughlin and Kazuhiro Hono, editors, *Physical Metallurgy*, volume 7, chapter 26, pages 2399–2595. Elsevier, 5th edition, 2014.

[137] D. Tsarouchas and A.E. Markaki. Extraction of fibre network architecture by X-ray tomography and prediction of elastic properties using an affine analytical model. *Acta Materialia*, 59(18):6989–7002, 2011.

[138] J. K. Smugeresky and N. R. Moody. Properties of high strength, blended elemental powder metallurgy titanium alloys. In F.H. Froes and D. Eylon, editors, *Titanium net near shape*, pages 131–141. The metallurgical society, 1984.

[139] N. Tuncer, G. Arslan, E. Maire, and L. Salvo. Influence of cell aspect ratio on architecture and compressive strength of titanium foams. *Materials Science and Engineering: A*, 528(24):7368–7374, sep 2011.

[140] J. F. Despois, R. Mueller, and A. Mortensen. Uniaxial deformation of microcellular metals. *Acta Materialia*, 54:4129–4142, 2006.

[141] E. Brandl, A. Schoberth, and C. Leyens. Morphology, microstructure, and hardness of titanium (Ti-6Al-4V) blocks deposited by wire-feed additive layer manufacturing (ALM). *Materials Science and Engineering: A*, 532:295–307, jan 2012.

[142] R. Ding and Z.X. Guo. Microstructural evolution of a Ti–6Al–4V alloy during β-phase processing: experimental and simulative investigations. *Materials Science and Engineering: A*, 365(1-2):172–179, jan 2004.

[143] P. Moongkhamklang, D.M. Elzey, and H.N.G. Wadley. Titanium matrix composite lattice structures. *Composites Part A: Applied Science and Manufacturing*, 39(2): 176–187, feb 2008.

[144] W. van Grunsven, E. Hernandez-Nava, G. Reilly, and R. Goodall. Fabrication and Mechanical Characterisation of Titanium Lattices with Graded Porosity. *Metals*, 4 (3):401–409, aug 2014.

[145] Y. Me-Bar and D. Shechtman. On the adiabatic flow of Ti-6Al-4V ballistic targets. *Mater. Sci. Eng.*, 58:181–188, 1983.

[146] S. P. Timothy and I. M. Hutchings. Initiation and growth of micro fractures along adiabatic shear band in Ti-6Al-4V. *Mater. Sci. Tech.*, 1:526–530, 1985.

[147] Y. Bai, C. Cheng, and S. Yu. On the evolution of thermo-plastic shear band. *Acta mech. Sin.*, 2:1–7, 1986.

[148] W. Lee and C. Lin. Plastic deformation and fracture behaviour of Ti–6Al–4V alloy loaded with high strain rate under various temperatures. *Materials Science and Engineering: A*, 241(1-2):48–59, jan 1998.

[149] Q. Xue, M.A. Meyers, and V.F. Nesterenko. Self-organization of shear bands in titanium and Ti–6Al–4V alloy. 50:575–596, 2002.

[150] A. J. Wagoner-Johnson, C. W. Bull, K. S. Kumar, and C. L. Briant. The influence of microstructure and strain rate on the compressive deformation behavior of Ti-6Al-4V. *Metallurgical and Materials Transactions A*, 34(2):295–306, 2003.

[151] M.A. Meyers, G. Subhash, B.K. Kad, and L. Prasad. Evolution of microstructure and shear-band formation in alpha-hcp titanium. *Mechanics of Materials*, 17:175–193, 1994.

[152] Y. B. Xu, Y. L. Bai, Q. Xue, and L. T. Shen. Formation, microstructure and development of the localized shear deformation in low-carbon steels. *Acta Materialia*, 44(5):1917–1926, 1996.

[153] K. H. Hartmann, H. D. Kunze, and L. W. Meyer. Metallurgical effects on impact loaded materials. In M.A. MeyerS and L.E. Murr, editors, *Shock waves and high strain ratye phenomena in metals, concepts and application.*, pages 325–337, New York, 1981. Plenum Press.

[154] L.W. Meyer, E. Staskewitsch, and A. Burblies. Adiabatic shear failure under biaxial dynamic compression/shear loading. *Mechanics of materials*, 17:203–214, 1994.

[155] J. H. Beatty, L. W. Meyer, M. A. Meyers, and S Nemat-Nasser. Formation of controlled ASB in AISI 4340 high strength steel. Shock-wave and high strain rate phenomena in materials. *National Technical Information Service*, pages 645–656, 1992.

[156] K. Minnaar and M. Zhou. An analysis of the dynamic shear failure resistance of structural metals. *Journal of Mechanics Physics and Solids*, 40(10):2155–2170, 1998.

[157] Y. Xu and M.A. Meyers. Microstructural Evolution of Localized Shear Bands Induced during Explosion in Ti-6Al-4V Alloy. *J. Mater Sci. Tech.,*, 19(5):385–387, 2003.

[158] N. Li, Y. D. Wang, R. Lin Peng, X. Sun, P. K. Liaw, G. L. Wu, L. Wang, and H. N. Cai. Localized amorphism after high-strain-rate deformation in TWIP steel. *Acta Materialia*, 59(16):6369–6377, 2011.

[159] S. Mercier and A. Molinari. Steady-State shear band propagation under dynamic conditions. *Journal of the Mechanics and Physics of Solids*, 46(8):1463–1495, 1998.

[160] T. Buckmann, M. Thiel, R. Kadic, T. Schittny, M. Wegener, and R. Bueckmann. An elasto-mechanical unfeelability cloak made of pentamode metamaterials. *Nature Communications*, Vol.5., 2014.

[161] D. T. Queheillalt, V. S. Deshpande, and H. N. G. Wadley. Truss waviness effects in cellular lattice structures. *Journal of mechanics of materials and structures*, 2 (October):1657–1675, 2007.

[162] I. Quintana Alonso and N. A. Fleck. Damage tolerance of an elastic-brittle diamond-celled honeycomb. *Scripta Materialia*, 56(8):693–696, 2007.

[163] E. Hernández-Nava, C.J. Smith, F. Derguti, S. Tammas-Williams, F. Léonard, P.J. Withers, I. Todd, and R. Goodall. The effect of defects on the mechanical response of Ti-6Al-4V cubic lattice structures fabricated by electron beam melting. *Acta materialia. Accepted*, 2016. doi: 10.1016/j.actamat.2016.02.029.

[164] A. Bauereiß, T. Scharowsky, and C. Körner. Defect generation and propagation mechanism during additive manufacturing by selective beam melting. *Journal of Materials Processing Technology*, 214(11):2497–2504, 2014.

[165] R. Lakes. Foam Structures with a Negative Poisson's Ratio. *Science*, 235(4792): 1038–1040, 1987.

[166] R. D. Doherty. Primary Recrystallization. In R. W. Cahn, editor, *Encyclopedia of Materials: Science and Technology.*, pages 7847–7850. Elsevier, 2005.

[167] F. J. Humphreys and M. Hatherly. *Recrystallization and related annealing phenomena.* Elsevier Ltd, Oxford UK., second edition, 2004.

[168] N. A. Fleck and R. A. Smith. Effect of density on tensile strength, fracture toughness, and fatigue crack propagation behaviour of sintered steel., 1981.

[169] K. Mills. *Metals Handbook: Fractography*, volume 12. ASM International, 9th edition.